EVALUATION OF PLASMA-SPRAYED ALUMINA AS THERMAL CONTROL COATINGS FOR MICRO-SATELLITES LI RENMING 2006

NANYANG TECHNOLOGICAL UNIVERSITY

EVALUATION OF PLASMA-SPRAYED ALUMINA AS THERMAL CONTROL COATINGS FOR MICRO-SATELLITES

LI RENMING

SCHOOL OF MECHANICAL AND AEROSPACE ENGINEERING

2006

Evaluation of Plasma-Sprayed Alumina as Thermal Control Coatings for Micro-Satellites

Li Renming

School of Mechanical and Aerospace Engineering

A thesis submitted to the Nanyang Technological University
in fulfillment of the requirement for the degree of
Doctor of Philosophy

2006

ACKNOWLEDGMENT

I would like to express my sincere gratitude to my supervisor Assistant Professor Sunil Chandrakant Joshi, and my co-supervisor Associate Professor Ng Heong Wah, for their invaluable guidance, encouragement, and patient assistance throughout this research work. Thanks should also be given to them for their help in my life in Singapore.

I also would like to thank research fellow Dr. Appuswamy Devasenapathi and research students Mr. Wang Peng and Mr. Kang Chang Wei, for their help, advice, and cooperation while performing experiments. Thanks are extended to Mr. U Win Tun, for his guidance in using an FE software. I am also grateful to Dr. Liu Lie, Dr. Su Fei and Dr. Jiang Dazhi, for their precious assistance, suggestions and discussions. They also brought me a lot of fun and cherishable memories in Nanyang Technological University.

In addition, I wish to thank all the technicians from the Strength of Materials Lab, Ceramics Lab, Materials Lab and Metrology Lab, for their unfailing technical support, without which the project would not progress smoothly.

Last but not least, I would like to thank my family members—my parents, parents-in-law, my wife Yang Dongli and my little sister, for a great deal of their encouragement and whole-hearted support.

Contents

List of Figures

List of Tables

SUMMARY

Hundreds of artificial satellites have been launched for the purposes of scientific, military, and commercial missions. Among them, micro-satellites are fast becoming important scientific and commercial realities because they provide shorter development times, smaller budgets and can achieve many of the functions of their larger counterparts. The thermal control subsystem becomes more important for micro-satellites, in view of reduction in packaging space and thermal mass. As a result, passive thermal control methods are adopted if possible, by use of films, coatings, multi layer insulations (MLI), sun shields, geometry, radiating fins and heat pipes. However, conventional thermal control materials (TCMs) used in satellites tend to deteriorate in the severe space environment (e.g., vacuum ultraviolet radiation, atomic oxygen attack, plasma radiation and space debris), often leading to unanticipated mission problems. New and better TCMs are thus constantly sought to reduce difficulties in satellite thermal design.

In this thesis, the suitability of plasma sprayed alumina coating as TCM for a satellite was examined. Such alumina coating has proved to be a good thermal barrier coating material for hot section components in aircraft engines. Panels of aluminum alloys such as 2024-$T3$, 6061-$T6$ and 7075, which are commonly used for satellite applications, form a very compatible substrate for plasma sprayed alumina coating. Various physical, thermal, processing parameters and simulated in-service behavior for plasma sprayed alumina coating were studied analytically and/ or experimentally. The results reveal that the plasma sprayed alumina coating has good potential as a substitute for conventional TCMs for micro-satellite components, including solar arrays.

During these investigations, surface roughness of plasma sprayed alumina coating was found very important because the roughness affects the radiation heat exchange between the surface and its surrounding. Roughness parameters such as root-mean-square roughness cannot properly evaluate such effects on radiation properties of opaque surfaces. Some models have been developed previously by other researchers to predict the surface roughness effects, such as Davies' model, Tang and Buckius' statistical geometric optics model. However they are valid only in their own specific situations.

As such, in this thesis, two geometrical energy absorption models were developed and applied, with the help of 2D surface profile measurements obtained using Talyscan 150 instrument and a few user-written C programs. One of the models was developed at micro level for a localized area of a large rough surface. It was to predict local effective normal solar absorptance and local effective hemispherical infrared (IR) emittance. The other, the macro-level model, was established by integration of all micro-level models for a large rough surface under consideration. These values of effective normal solar absorptance and effective hemispherical IR emittance for the rough surface derived by the macro-level model, if used in the heat transfer analysis of an equivalent, smooth and optically flat surface, lead to the prediction of the same rate of heat exchange and temperature as that of the rough surface.

Both of the above models were validated by means of simulations and experiments for plasma sprayed alumina coating surfaces. Even though they were not tested for other materials, the model formulations are generic enough to be employed for the surfaces either of similar opaque materials or coated with such opaque materials where the substrates have little influence on the radiation properties. Thus they can be used to incorporate the rough surface effects for other type of thermal control coatings, provided that the baseline values of normal solar absorptance and hemispherical IR emittance are available.

ACRONYMS

AO	Atomic Oxygen
ASTM	American Society for Testing and Materials (100 Barr Harbor Drive, West Conshohocken, Pennsylvania, USA)
AutoCAD	A commercial CAD software from Autodesk® (Autodesk Inc., 111 Mclnnis Parkway, San Rafael, CA 94903, USA)
CAD	Computer Aided Design
CPSP	Critical Process Spray Parameter
CTE	Coefficient of Thermal Expansion
CVD	Chemical Vapor Deposition
ESA	European Space Agency
ESH	Equivalent Sun Hours
FE	Finite Element
FEA	Finite Element Analysis
FEM	Finite Element Method
IR	Infrared
LDEF	Long Duration Exposure Facility
LEO	Low Earth Orbit
LHS	Left Hand Side
LUSAS	A commercial FEA software from LUSAS (forge House, 66 High Street, Kingston upon Thames, Surrey, KT1 1HN, United Kingdom)
LV	Local Valley
MATHEMATICA	A commercial scientific software from Wolfram Research Inc. (100 Trade Center Drive, Champaign, IL 61820-7237, USA)
MATLAB	A commercial scientific software from The MathWorks, Inc. (3 Apple Hill Drive, Natick, MA 01760-2098, USA)
MHT	Microhardness Tester
MLI	Multi Layer Insulation
MMOD	Micrometeoroid/ Orbital Debris
NASA	National Aeronautics and Space Administration
PVD	Physical Vapor Deposition

RHS	Right Hand Side
SEM	Scanning Electron Microscope
SINDA/G	A commercial thermal analyzer (Systems Integrated Numerical Differential Analyzer/ Gaski) from Network Analysis, Inc. (4151 W. Lindbergh Way, Chandler, AZ 85226)
SLV	Semi Local Valley
TCM	Thermal Control Material
TML	Total Mass Loss
UV	Ultraviolet
VUV	Vacuum Ultraviolet

NOMENCLATURE

c_p	Heat capacity, $J/kg\ ^\circ C$
h	Satellite orbit height, km
i	Hitting number
t	Orbit time, min
$t_j,\ j = 1 - 11$	Dividing timeline, min
t_p	Time period, min
w	Width, μm
A	Area, μm^2
B	Area, μm^2
E	Young's modulus, GPa
F	View factor (configuration factor)
H_{V3N}	Microhardness under 3 N loading, MPa
I	Heat flux intensity, W/m^2
I_a	Albedo flux intensity, W/m^2
I_I	IR flux intensity, W/m^2
I_s	Solar flux intensity, W/m^2
I_r	Real heat flux intensity, W/m^2
I_{S1}	Heat flux intensity for surface $S1$, W/m^2
I_{S2}	Heat flux intensity for surface $S2$, W/m^2
R	Radius of the earth, km
$S1$	Surface 1 of aluminum panel
$S2$	Surface 2 of aluminum panel
T	Temperature, $^\circ C$ or K
T_0	Environment temperature, $^\circ C$ or K
T_{eq}	Equilibrium temperature, $^\circ C$ or K
$T_{\max}$	Maximum stabilized temperature, $^\circ C$ or K
$T_{\min}$	Minimum stabilized temperature, $^\circ C$ or K
V	Volume, m^3
R_a	Roughness parameter, arithmetic mean of the absolute departures of the roughness
R_z	Roughness parameter, numerical average height difference between the five highes
Cr_2O_3	Chrome oxide
$NiCoCrAlY$	Composition of Ni, Co, Cr, Al and Y
$NiCr$	Composition of Ni and Cr
$NiCrAlY$	Composition of Ni, Cr, Al and Y
Nb_2O_5	Niobium pentoxide

SiO_2	Silicon oxide
TiO_2	Niobium pentoxide
WO_3	Tungsten oxide
ZrO_2	Zirconium oxide

α_n	Total normal solar absorptance
α_{ne}	Effective absorptance
α_{nel}	Local effective absorptance
Δt	Time interval, min
ϵ_h	Total hemispherical emittance
ϵ_{he}	Effective emittance
ϵ_{hel}	Local effective emittance
$\sigma_{\max}$	Maximum stress, MPa
ρ	Density, kg/m^3

LIST OF PUBLICATIONS

During the research period, two journal papers and three conference papers relevant to the thesis topic were published, which are listed below:

(1) R M Li, S C Joshi and H W Ng, "Radiation Properties Modeling for Plasma-Sprayed-Alumina-Coated Rough Surfaces for Spacecrafts," in *Materials Science and Engineering B 132 (2006), pp. 209-214*

(2) R M Li, S C Joshi and H W Ng, "Characterization of Plasma Sprayed Alumina as Thermal Control Coating for Micro-Satellite Applications," in *Journal of Materials: Design and Applications (Proceedings of the Institution of Mechanical Engineers Vol. 219 Part L)*, 21 January 2005, pp. 111-119

(3) R M Li, S C Joshi and H W Ng, "Radiation Properties Modeling for Plasma-Sprayed-Alumina-Coated Rough Surfaces for Spacecrafts," presented in The 3rd International Conference on Materials for Advanced Technologies, Singapore, 2005

(4) R M Li, S C Joshi and H W Ng, "FE Simulation of In-Service Thermal Behavior of Plasma Sprayed Alumina Coated Satellite Substrates," *Proceedings of the Fourth Australasian Congress on Applied Mechanics*, Institution of Engineers (Australia), Melbourne, Australia. 16-18 February 2005

(5) R M Li, S C Joshi and H W Ng, "Air-Plasma Sprayed Alumina Coating as Thermal Control Material for Satellite Panels," presented in The 2nd International Conference on Materials for Advanced Technologies, Singapore, 2003

Chapter 1

INTRODUCTION

1.1 Background

Micro-satellite (10-100 kg category) technologies are the current trend in satellite development because they provide cost effective solutions to a wide range of missions. When satellites get smaller in size, thermal control becomes more important, in view of reduction in packaging space and thermal mass. Passive thermal control methods are commonly used for small satellites, because active methods require electric power, more hardware and space for installation. For the passive thermal control method, reflective and radiative films, coatings and multi-layer insulations are mostly selected and applied on the surfaces of different components. However, most of them deteriorate in the harmful outer space environment, many times leading to unanticipated mission problems. New and better TCMs are constantly sought to reduce difficulties in satellite thermal design and to assure the desired missions completed.

Plasma sprayed alumina coating has proved as a good thermal barrier coating material for hot section components in aircraft engines. Some plasma sprayed alumina coating properties are similar to that of TCMs such as $Z93$, $YB71$, $S13G\text{-}LO$ and $A276$. However, plasma sprayed alumina coating is never used as TCM in space applications. In this thesis, the suitability of such alumina coating as TCM for a micro-satellite was examined.

During this investigation, the surface roughness of plasma sprayed alumina coating is found important, because the roughness affects the radiative heat exchange between the surface and its surrounding. Roughness parameters such as root-mean-square roughness cannot properly evaluate surface roughness effects on radiation properties of opaque surfaces. Some models have been developed earlier to predict the effects, such as Davies' model, Tang and Buckius's statistical geometric optics model. However they are valid only in their own specific situations. In this thesis, two geometrical energy absorption models (each consists of two sub-models: (i) micro-level sub-model, and (ii) macro-level sub-model) were developed and applied to investigate the roughness effects with the help of 2D surface profile of plasma-sprayed-alumina-coated substrate scanned at micron level. This model predicts effective normal solar absorptance (α_{ne}) and effective hemispherical infrared emittance (ϵ_{he}) of a rough surface. These values, if used in the heat transfer analysis of an equivalent, smooth and optically flat surface, lead to the prediction of the same rate of heat exchange and temperature as that of for the rough surface. The model is validated using a few typical cases of plasma-sprayed-alumina-coated rough surfaces. Even though they were not tested for other materials, the model formulations are generic enough to be employed for the surfaces either of similar opaque materials or coated with such opaque materials where the substrates have little influence on the radiation properties. Thus they can be used to incorporate the rough surface effects for other types of thermal control coatings, provided the baseline values of normal solar absorptance (α_n) and hemispherical infrared emittance (ϵ_h)that are available for an optically flat surface produced using the same material.

1.2 Objectives

One objective of this project is to study the performance of plasma sprayed alumina coating as TCM for satellites in low earth orbit (LEO) environment, analytically and

experimentally, in order to enhance the thermal stability and to improve thermal control characteristics. The other objective is to develop models that can predict α_{ne} and ϵ_{he} respectively for a rough surface, such as plasma-sprayed-alumina-coated aluminum plate. The effective values of α and ϵ are useful for heat transfer analysis of an equivalent, smooth and optically flat surface. These values will lead to the prediction of the same rate of heat exchange and temperature as that of for the rough surface. This will eventually minimize the need for testing every coated surface.

1.3 Scope

To achieve the above mentioned objectives, relevant literature, existing numerical and experimental techniques are explored. Literature review is carried out for collection of useful known properties of plasma sprayed alumina coating, satellite thermal control and other related information. Finite element method (FEM) and user-written C programs are used to perform temperature and stress analyses for understanding thermomechanical behavior of plasma-sprayed-alumina-coated panels in LEO thermal environment. Experiments, such as plasma spray, microhardness measurements, surface profiles scanning, absorptance and emittance measurements and vacuum outgassing tests, were carried out to examine the various properties of plasma sprayed alumina coating. The α_{ne} model and ϵ_{he} model were developed at micro-level and macro-level with the help of surface profile scanning and user-written C programs.

1.4 Outline of the Thesis

Chapter 2 presents the literature review, providing the background of the topic and the literature evidence for plasma sprayed alumina coating as TCM, which includes micro-satellite applications, satellite thermal control technologies, degradation of TCMs in outer

space environment, selection criteria for TCMs, plasma spray technique and properties of plasma sprayed alumina coating. Chapter 3 summarizes the suitability of plasma sprayed alumina coating as TCM for spacecraft applications. Chapter 4 describes experimental studies on production and properties examinations of plasma sprayed alumina coating, to prove the coating suitability as TCM. Chapter 5 contains FEA studies for in-service behavior of plasma-sprayed-alumina-coated panels, to predict the on-flight performance of the coated panel in terms of the minimum/ maximum stabilized temperature and stress of the coated panel. Chapter 6 involves developments and validations for both micro-level model and macro-level model. The two models together predict the effective absorptance and emittance of a rough opaque surface if baseline values of normal solar absorptance and hemispherical IR emittance are available. Chapter 7 highlights the conclusions drawn and the recommended future work. Finally, the copy of test certificate is provided in the Appendix.

Chapter 2

LITERATURE REVIEW

2.1 Micro-Satellites

Hundreds of artificial satellites have been launched for the purposes of scientific, military, and commercial missions [3,26,28,41,58,84,100]. The theoretical foundation for artificial earth-orbiting satellites dates back over three hundred years, to Isaac Newton's theory of gravitation. In the early 20th century Robert Goddard in America and Konstantin Tsiolkovsky in Russia demonstrated the technological foundations for the use of rockets to carry satellites into orbit. Theory became reality on the evening of October 4, 1957, when the Soviets launched Sputnik-1 into orbit [47].

In terms of wet mass (the mass including fuel), satellites are classified into three groups: Large satellite ($> 1000\ kg$), medium sized satellite ($500 - 1000\ kg$) and small satellite ($< 500\ kg$). However, group of small satellite includes mini satellite ($100 - 500\ kg$), Micro satellite ($10 - 100\ kg$), nano satellite ($1 - 10\ kg$), Pico satellite ($0.1 - 1\ kg$), and femto satellite ($< 100\ g$) [12]. Micro-satellites are fast becoming important scientific and commercial realities. They provide cost-effective solutions to traditional missions. Smaller satellites provide shorter development times, smaller budgets and can achieve many of the functions of their larger counterparts [28]. It is reported that 243 micro-satellites have been launched between year 1983 and year 1999 [12].

There are a variety of orbit types for satellites that are common to near-Earth space operations: LEO, middle earth orbit, geosynchronous orbit, Sun-synchronous orbit and Molniya-type orbit [26, 41, 58, 84]. LEO has altitudes between 300 km and 1000 km and have the shortest periods, of the order of 90 min [41]. Some of these orbits are circular while others may be somewhat elliptical. The inclination of these orbits, which is the angle between the plane of the equator and the plane of the orbit, can also vary from 0° to greater than 90° . LEOs are very often given high inclinations so that the satellite can pass over the entire surface of the Earth from pole to pole as it orbits. This coverage is important for weather and surveillance missions. The big advantage of LEO satellites is that they are smaller and cheaper to build and launch. Because of their lower heights, they can be accessed very easily, even from mobile or cellular type handsets [105]. Micro-satellites are generally launched into LEO [12, 41].

In LEO, the spacecraft is below the radiation belts but does have to contend with several atmospheric effects, especially those related to reactions with atomic oxygen and atmospheric drag. A special case of the LEO is the polar orbit (∼90° inclination), which places the satellite in the high-radiation environment of the auroral zones around the north and south poles [116].

Generally micro-satellites remain in LEO, have shorter orbit durations and need to perform frequent maneuvers. Thus, the solar arrays are exposed to frequently changing radiation environment and experience thermal shocks, which may affect the solar cells efficiency and disturb the stability of the whole satellite [47].

2.2 Satellite Thermal Control

Thermal control is a subsystem of satellite. Its purpose is to maintain all the elements of a spacecraft within their temperature limits for all mission phases. Satellites perform

better and last longer when their components remain within certain temperature limits, usually near the level at which they are assembled [5, 9, 14, 19, 34, 56, 68]. For example, general operating temperature range for solar array is -100 to $+85$ $^{\circ}C$ [58].

In order to provide a design that meets the temperature requirements of a spacecraft, heat inputs from the sun, the earth, and electrical and electronic components on board the spacecraft must be accounted for. In most cases, the heat inputs are highly variable with time. The thermal control subsystem accounts for about 2-5% of the total spacecraft cost and about the same percentage of the dry weight.

The external surfaces of a spacecraft radiatively couple the spacecraft to space. Because these surfaces are also exposed to external sources of energy including sunlight, albedo and Earth-emitted IR radiation, their radiative properties must be selected to achieve an energy balance at the desired temperature between spacecraft internal dissipation, external sources of heat, and reradiation to space. The steady state of radiation heat transfer for a body without heat source in space can be described by Stefan-Boltzmann's Law:

$$\alpha(I_S A_S + I_I A_I + I_A A_A) = \epsilon\sigma(A_S + A_I + A_A)(T_{eq}^4 - T_0^4) \tag{2.1}$$

Where

α-Solar absorptance of the surface facing solar radiation normally,

ϵ-Emittance of the surface facing its environment,

$\sigma = 5.6697E-8\ W/m^2 \cdot K^4$, Stefan-Boltzmann constant,

I- Flux intensity of radiation (W/m^2. Subscripts' meaning: S-Solar, I-IR, A-Albedo),

A - Area of absorbing or emitting radiation energy (m^2),

T_0 - Environmental temperature (K),

T_{eq} - Equilibrium temperature of the body (K).

Requirements for a thermal control subsystem usually exist at several levels. Top-level system requirements define allowable temperature margins, overall testing re-

quirements, and environmental conditions such as the flux levels for direct solar, Earth-reflected solar (albedo), and earth-emitted energy. Subsystem weight allocations and cost goals are requirements derived by the spacecraft project management. Finally, component temperature limits are defined based on supplier data. Typically allowed temperature ranges for spacecraft components are given in Table 2.1 [12]. Silicon solar cells usually operate over a wide range. However, the efficiency of the solar cells decreases with an increase in temperature [71, 79, 98, 99, 130]. But the decrease is relatively small. For silicon solar cells, the efficiency is 13.5% and 10% at 112 $^{\circ}C$ and 150 $^{\circ}C$ respectively. The change of efficiency is only

$$\frac{0.135 - 0.100}{150 - 112} \times 100\% \approx 0.1\% \ (/^{\circ}C) \tag{2.2}$$

For GaAs cells, the efficiency changes from 19% to 16% when temperature increases from 112 $^{\circ}C$ to 150 $^{\circ}C$ [99]. However, uniformity of solar panel temperature is more important. If solar cells from the same string experience different temperature, the whole string might malfunction or fail. Another issue is reliability of the coating so that the power output remains the same for the entire life of satellite. Further more, deflections due to non-uniform temperature distributions may cause cracks in solar cells.

When a satellite becomes smaller, its thermal control becomes more important, in view of reduction in packaging space and thermal mass. Spacecraft thermal control subsystems are classified into passive methods and active methods. The involved components and devices, such as heat pipes, coatings, insulators, etc., are used extensively

Table 2.1: Typical temperature ranges for selected spacecraft components

Components	Typical temperature range ($^{\circ}C$)
Electronics	0 to 40
Batteries	5 to 20
Solar arrays	-100 to +100
Propellant, Hydrazine	7 to 35
Structures	-45 to +65
IR detectors	-200 to -80

in thermal control subsystems. Some further information of the components and devices are provided in the following sections.

2.2.1 Active Thermal Control

Active thermal control methods, by means of electrical heaters, heat pipes with related systems and so on, need power supply from power subsystem of satellite [25, 41, 58, 125]. They are typically applied to regions that require fine temperature control, i.e., propellant and electronics that are sensitive to temperature. Generally they are avoided for micro-satellites to keep the power consumption to minimum and to save mass and space for installations.

2.2.2 Passive Thermal Control

Passive thermal control involves configuring the spacecraft's balance of absorptance and emittance such that it maintains a natural radiative thermal balance at the desired temperature [9, 58, 84]. It is applied whenever possible to avoid expending power and to save mass and installing space. The traditional materials for passive thermal control are discussed in the following section.

2.2.3 Passive Thermal Control Materials

Surface films, coatings or paints with special radiation properties provide the desired thermal performance of the surface. The involved technologies include physical vapor deposition (PVD), chemical vapor deposition (CVD) [53, 60], anodization [52, 69], (reactive/ pulsed/ unbalanced) magnetron sputtering [22] and painting [109]. The passive thermal control is based on the Stefan-Boltzmann's Law, whose full formulation is

$$\alpha I A_{in} = \sigma \epsilon F A_{out} \left(T^4 - T_0^4\right) \tag{2.3}$$

Surfaces can either naturally, or after-treatment be made to, absorb and emit radiant heat at specific rates corresponding to the spectrum of radiation. The terms α and ϵ in Equation 2.3 are a function of spectrum, as primary surface properties. They determine an object's temperature in environment with only radiation heat transfer. Thus, in spacecraft thermal designs, materials with various values of α and ϵ are used to meet temperature control requirements. Solar reflectors, such as second-surface mirrors and white paints, or silver- or aluminum-backed Teflon® are applied to minimize absorbed solar energy, yet emit energy almost like an ideal black body. To minimize both the absorbed solar energy and IR emission, polished metal such as aluminum foil or gold plating is used. On the interior of the vehicle, if it is desired to exchange energy with the compartment and/ or other equipment, black paint is commonly used. Thus, the existing state of the art uses a rather wide variety of wavelength-dependent coatings/ films/ paints. The problems of in-space stability, outgassing [11, 57, 86], and mechanical adhesion to the substrate are challenges that have to be resolved for most coatings.

Two or more coatings are sometimes combined in a checkerboard or striped pattern to obtain the desired characteristics. There are four basic types of thermal control surfaces: solar reflector, solar absorber, flat reflector, and flat absorber, as shown in Figure 2.1 [38]. The solar reflector reflects incident solar energy while absorbing and emitting IR energy, characterized by a very low $\frac{\alpha}{\epsilon}$ ratio [60]. Solar absorbers absorb solar energy while emitting only a small percentage of the IR energy [20]. Polished metal surfaces approximate solar absorbers. Flat reflectors reflect energy throughout the spectral range, i.e., they reflect in both the solar and IR radiation regions, while flat absorbers, such as black paint, absorb throughout the spectral range. Table 2.2 lists the most common thermal control finishes used on today's satellites, and their properties [12]. It should be noted that the values given here are for 'normal' temperature ranges. Substantial changes may occur at cryogenic or very high temperatures [33, 115].

Several newly-developed TCMs are reviewed as follows: a systematic search for a suitable composition and thickness of $Ti_xAl_yN_z$ alloy coatings prepared by reactive, unbalanced magnetron sputtering from targets consisting of differently sized titanium and aluminum sectors was reported [22]. Neglecting internal heat contributions, the lowest calculated equilibrium temperature in orbit around the Earth, 32.5 $°C$, was obtained for a 505-nm-thick $Ti_{0.14}Al_{0.47}N_{0.40}$ film. This film was obtained by sputtering from target (50% titanium and 50% aluminum) for 30 min at 120 W, with a nitrogen gas flow of 1.8 ml/min. However, the space environmental effects on this coating are not yet studied.

Several WO_3 and SiO_2 multilayer coatings were accomplished with Eratron Model EB-8 electron beam evaporator [52]. The coatings, whose thickness ranges from 50 nm to 366 nm, were predicted by computer program and were subsequently manufactured with electron beam evaporation and characterized with both optical and thermal techniques. Solar absorptance values were observed optically in the range of 0.048-0.093 and calorimetrically in the range of 0.069-0.100.

$Z93P$, a common thermal control paint used for heat rejection on spacecraft, and

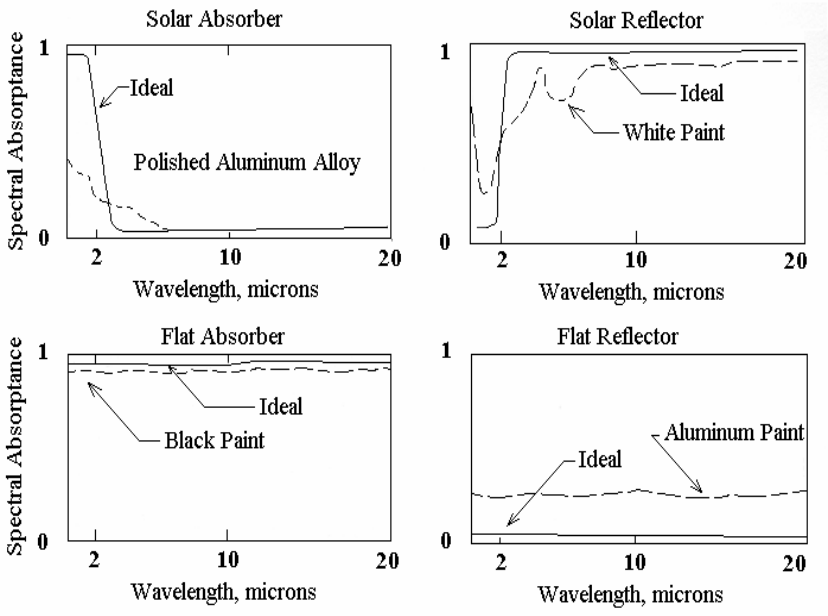

Figure 2.1: Ideal representation of four basic passive control surfaces [38]

black anodized aluminum are chosen to design the thermal control surface for optimum heat rejection at the highest expected temperature. Their low temperature performance has been studied [52].

Anodization of aluminum and its alloys is a well-known electrochemical process with wide spread applications [21, 122]. Anodization of aluminum alloy 2024 (aluminum alloy 2024) in sulfuric acid bath has been studied to develop white anodic oxide coating. The obtained 10.5 ± 0.5 μm-thick oxide coating provides a ratio of solar absorptance to infrared emittance, as low as 0.2 (which determines the equilibrium temperature of

Table 2.2: Properties of common surface finishes [12]

Surface Finish	α (Beginning-of-Life)	ϵ
Optical Solar Reflectors		
8 *mil* Quartz mirrors	0.05 to 0.08	0.80
2 *mil* Silvered Teflon ®	0.05 to 0.09	0.66
5 *mil* Silvered Teflon ®	0.05 to 0.09	0.78
2 *mil* Aluminized Teflon ®	0.10 to 0.16	0.66
5 *mil* Aluminized Teflon ®	0.10 to 0.16	0.78
White Paints		
*S*13*G-LO*	0.20 to 0.25	0.85
*Z*93	0.17 to 0.20	0.92
ZOT	0.18 to 0.20	0.91
Chemglaze *A*276	0.22 to 0.28	0.88
Black Paints		
Chemglaze *Z*306	0.92 to 0.98	0.89
3M Black Velvet	$\sim$ 0.97	0.84
Aluminized Kapton		
1/2 *mil*	0.34	0.55
1 *mil*	0.38	0.67
2 *mil*	0.41	0.75
5 *mil*	0.46	0.86
Metallic		
Vapor deposited aluminum	0.08 to 0.17	0.04
Bare aluminum	0.09 to 0.17	0.03 to 0.10
Vapor deposited gold	0.19 to 0.30	0.03
Anodized aluminum	0.25 to 0.86	0.04 to 0.88
Mylar		
1/4 *mil* Aluminized Mylar, Mylar side	(Degrades in sunlight)	0.34
Beta cloth	0.32	0.86
Astro quartz	$\sim$ 0.22	0.80
MAXORB	0.9	0.10

solid objects in outer space environment. The lower the ratio, the lower the equilibrium temperature). The optical properties and hardness values measured under optimum experimental conditions support its use as a thermal control coating on external surface of spacecraft [69]. However, there is no report available about space environmental effects on the anodized coatings.

In year 2006, it was reported that 10-20 μm mullite ($2Al_2O_3 \cdot SiO_2$) was deposited to aluminum substrate by plasma spraying, to form TCM as well as thermal barrier coating for atmospheric reentry vehicles [104]. The preliminary space stability tests by the authors of the reference [104] showed only negligible variations both in mechanical and thermal optical properties of the mullite coating under the conditions selected. For the tests, two grain sizes were used and various spraying parameters were selected to make eight different samples for each grain size. Moreover, the arithmetic mean surface roughness R_a of the plasma-sprayed coatings was measured and the correlation coefficient between R_a and the thermal emittance ϵ was found to be 0.82.

Insulation blankets are used to prevent heat coming in or going out of the protected component. Generally they consist of many layers of light-weight material that conducts heat very poorly, such as aluminum-coated polyamide films (Kapton). Sensors and payloads can be wrapped in insulation blankets to thermally isolate them and reduce thermal control requirements.

A space radiator is a heat exchanger with a large surface area on the outer surface of a spacecraft that spreads out the waste heat to deep space [27]. For an active system, radiators consist of a lattice work of fluid loops (usually freon). For a passive system, there's connector with high heat conductivity between radiator and heat source. Radiator size depends on both heat loads and required temperature. The location for radiator depends on satellite orientation along orbit movement. Second surface mirrors are considered space radiators.

2.3 Degradation of Thermal Control Materials

The manufacturing and application of surface coatings have become largely automated and less prone to human imperfections. Despite careful and successful management on the ground, problems have persisted in space [109]. Among the outstanding ones are degradation of properties, erosion from atomic oxygen (AO) attacks, and delamination of bonded material [2, 10, 93, 116].

2.3.1 Degradation Cause and Its Effects

Thermal control finishes are affected in orbit by charged particles, ultraviolet radiation, high vacuum, and the contaminant films that deposit on almost all spacecraft surfaces. The general result of these processes is an increase in solar absorptance by certain percentage (up to 250%). This is normally undesirable from a thermal control standpoint because spacecraft radiators must be sized to account for the substantial increase in absorbed solar energy that occurs due to degradation over the mission. These radiators, which are oversized to handle the high solar loads at "end-of-life", cause the spacecraft to run much cooler in the early years of the mission, sometimes necessitating the use of heaters to avoid under-temperatures of electronic components. The degradation is, therefore, a problem not only because of the solar load, but also because of the change in load over the course of the mission. The stability of coating properties is therefore important in order to minimize heater-power requirements [41]. More desirable coatings are necessary to be worked out.

Different materials are affected in different ways by the space exposure. White paints, such as $S13G$, are affected most strongly by ultraviolet (UV) radiation and charged particles (protons and electrons), and can degrade from $\alpha = 0.20$ to $\alpha = 0.70$ in just a few years. Quartz mirrors, on the other hand, experience essentially no damage due to the UV and charged particles, leaving only contamination as a source of

increased absorptance. Aluminized or silvered Teflon® films show degradation due to both charged-particle damage and contaminant deposition. Contamination results when volatile condensable materials are outgassed from spacecraft components, primarily electronic boxes, and then deposit out on the thermal finishes. This outgassing is strongest early in the mission (the first few months to one year) and tapers off with time. Once the contaminants deposit on the thermal surfaces they are in turn darkened by the UV and charged-particle environment. The net result is a rather large increase in solar absorptance in the first few years of the mission, followed by a small steady increase until end-of-life.

2.3.2 Outgassing

Observed rate of contamination induced $\Delta\alpha$ is not completely understood, but is known to be strongly dependent upon such factors as the types of materials used in the spacecraft, the venting of outgassed materials across thermal surfaces as they leave the spacecraft, and the presence of sunlight, which enhances the deposition of contaminants onto surfaces. Because of these effects, many programs are switching to lower outgassing materials and redesigning vent paths to insure that these outgassed contaminants are directed out to space without impinging onto the thermally sensitive surfaces.

Outgassing characteristics of four types of surface finish were tested previously [25]: alodined aluminum, anodized aluminum, Kapton-coated aluminum and Kapton-coated alodined aluminum. The alodined aluminum plates were manufactured in accordance with NASA MIL-C-5541 Class 3 document, by ACP Metal Finishing Pte Ltd (Singapore) which is approved for aerospace coating operations. The alodined aluminum samples were polished to the required surface roughness of 600 grit and cleaned prior to the conversion coat was carried out. The anodized aluminum samples were also prepared by ACP Metal Finishing Pte Ltd (Singapore). The chemical anodizing process

was executed in line with NASA MIL-A-8625 Type I Class 1 document. After polished to 600-grit roughness, cleaned and dried, Chromic acid was used for the anodizing process. The Kapton film was adhered to the buffed aluminum plates using 3M 966 pressure-sensitive adhesive, following the recommended conditions given by 3M Company, to make Kapton-film-coated aluminum samples. The Kapton-film-coated alodined aluminum samples were achieved by applying Kapton film onto the alodined aluminum plates using 3M 966 pressure-sensitive adhesive. The outgassing results are shown in Tables 4.8, 4.9, 4.10, and 4.11 respectively for comparison with similar testing results. For each type of the sample, six specimens ($50\ mm \times 50\ mm \times 1.5\ mm$) were prepared and tested. All the four types of samples were examined at the same time for mass loss; they were weighed before and after vacuum baking.

As mentioned earlier, aluminized and silvered Teflon® films degrade due to both contamination and natural environmental effects. High absorptance surfaces, such as black paints, generally do not degrade. There may, however, be a slight (a few percentage points) reduction in absorptance over time due to UV bleaching.

The change in solar absorptance is calculated by analytical correlation of thermal math models to flight temperature increases on the satellite. Because of the much shorter orbit period and the effects of highly variable earth heating rates, it is much harder to separate out absorptance changes from other effects for LEO satellites. This may explain the shortage of data for LEO systems.

2.3.3 The Long Duration Exposure Facility

NASA's Long Duration Exposure Facility (LDEF) was designed to provide long-term data on the space environment and its effects on space systems and operations. There were 57 experiments containing over 10,000 specimens on the LDEF [41]. LDEF was gravity-gradient stabilized, with one side of the vehicle continuously pointing down toward earth

center, and another side always facing the velocity vector, within one degree. During the mission, the leading-edge materials, i.e., those facing into the velocity vector, were exposed to approximately 9E21 oxygen $atoms/cm^2$, a level at which erosion of over 0.254 mm would be expected for many polymers.

The LDEF observations on thermal control materials are particularly significant for AO effects on the leading edge for LEO, while the trailing-edge samples show the effects of UV radiation. The thermal control surfaces experiment provided on-orbit leading-edge data on thermal properties of 25 materials during the first 18 months of the mission [125]. The inorganic binder paints, such as $Z93$ (zinc oxide in a potassium silicate binder) and $YB71$ (zinc orthotitanate in a potassium silicate binder), were shown to be stable in the LEO environment. Some TCMs degraded more, others less, than predicted from ground tests. The thermal-control properties (α and ϵ) of organic binder paints, commonly used for their ease of application, were observed to degrade by as much as a factor of 3 on the trailing edge, but show much smaller changes on the leading edge. Data from paints flown on the M0003 experiment on LDEF are shown in Table 2.3 [82]. The data from the trailing edge at or near 180 ° clearly shows the degradation of the polyurethane paint $A276$ by solar UV, while the degraded binder on the leading edge near 0 ° has been removed by the AO erosion to maintain properties close to the initial values. It should be noted that the degradation caused by space environment is not uniform. This non-uniform degradation leads to non-uniform temperature distributions, which can cause malfunction of components, such as solar cells.

Table 2.3: Solar absorptance of thermal control paints on LDEF M0003

Paint	Initial α	Leading Edge α	Trailing Edge α	Max. Change (%)
$YB71$	0.130	0.182	0.182	40
$A276$	0.282	0.228	0.552	96
$S13GLO$	0.147	0.232	0.458	212
$D111$	0.971	0.933	0.968	-0.04

2.4 Selection of Thermal Control Materials

There are many testing standards that can be used for the selection of TCMs, such as ASTM, NASA and ESA standards [2, 5, 6, 9, 10, 14]. Some NASA preferred reliability practices for spacecraft thermal control coatings design and application are listed below [5]:

(1) The α and ϵ of particular thermal control coatings are determined and verified by testing. When possible, test measurements are made with the test sample subject to actual flight conditions such as vacuum, temperature, etc.

(2) Effects of surface roughness and coating thickness are primary considerations in the applications of coatings.

(3) Flight data is researched and laboratory testing is performed to determine thermal coating's susceptibility to space radiation and the amount of degradation that can be expected during the lifetime of a mission.

(4) A detailed analysis of the contamination of the spacecraft is performed in order to determine the amount and type of contaminates expected to develop on surfaces of the spacecraft.

(5) Electrical properties are primary considerations used in the selection of thermal control coatings.

2.5 Plasma Spray Technique

Plasma is a gaseous collection of electrons, ions and neutral molecules. The plasma used for ceramic processing is generally operated in air [95]. Plasma spraying of ceramic coatings has become well established as a commercial process over the past 38 years

[64, 72, 90, 101, 113, 117, 120, 129]. Basically plasma spraying consists of the injection of powders into a direct current plasma jet of temperature up to $15,000\ K$ and velocity up to 1 km/s [43], where they are melted and accelerated, and directing the stream of molten particles onto a substrate where they form a coating as they spread and solidify very quickly.

The common air plasma spraying equipment consists of the power sources, control and monitor unit, plasma torch, cooling system, gas supply, powder feed unit, spraying chamber, exhaust equipment, motion devices for the control of the plasma torch, the sprayed part and the appropriate connecting cables and hoses.

2.5.1 Applications of Plasma Sprayed Ceramic Coatings

Plasma spraying has received considerable attention as a process for obtaining protective coatings. Plasma sprayed coatings are widely used in corrosion [24, 35, 54, 83, 88, 126, 127] and wear protection [17, 23, 36, 43, 97], or thermal and electrical insulation [66], etc.. Any variation in spraying variables affects the structure and properties of the received coatings, even in the case of identical materials and equipment. But these variables can be controlled to get the best coatings [30, 32, 36, 80, 89–91, 94, 97]. Table 2.4 summarizes the ceramic coatings that have been developed and widely used in various branches of industry.

2.5.2 Plasma Gases

At present, primary plasma forming gases such as Ar, He, H_2, N_2 and to a lesser extent air and water (for use in torches with water stabilization), are brought into the plasma state [31, 51, 92, 103]. Ionization of Ar starts at $9,000\ K$ and completes at $22,000\ K$ [77]. Enthalpy of one-atom gas is considerably lower than those of two-atom gases. Moreover, the gases have been preferred because of their easier transfer to plasma state, they provide

Table 2.4: The main application features of ceramic coatings

Coatings	Engineering Environment	Engineering Reference Application
Al_2O_3, Al_2O_3-TiO_2, Cr_2O_3	Wear	Mechanical parts in textile industry, petrochemical and paper making equipments
TiO_2-ZrO_2-Nb_2O_5	Infrared radiation	Electric heating
ZrO_2 bioglass	Biological compatibility	Bioceramic coatings for artificial bones, joints and tooth roots
ZrO_2, Al_2O_3, ZrO_2-metal	Low thermal diffusivity, good thermal shock resistance	Thermal barrier coatings for diesel engine and jet engine hot section components
$NiCr$, $NiAl$, $NiCrAlY$	High strength, good adhesion to substrate	Bonding coating between the ceramic coating and substrate [46, 62, 63, 102, 114]

a stable electric arc, and they require a lower working voltage. In addition, temperature of their plasmas is the highest. From the viewpoint of their effects on the sprayed material, argon and especially helium assure high inertness of environment. Because Ar and He do not dissociate, their beam are very bright, short and constricted. Such a beam allows local deposit of the spraying layer, facilitating considerably higher spraying efficiency. Typical flow rate is 40-50 Nl/min, in some installation up to 80 Nl/min.

2.5.3 Preparation of Surfaces prior to Spraying

Preparation prior to plasma spraying is important for ensuring strong bonding of the sprayed coating with the substrate material, since the bond is mostly of mechanical character [18, 44–46, 49, 67, 81, 87]. The surface must be sufficiently rough in order to adhere the sprayed particles in its unevenness. Optimum conditions for forming a strong bond can be ensured by removing moisture, grease and oxide films and by providing suitable roughness [77]. As predicted by most authors the adhesion strength increases with roughness at least for the well-molten particles. Coatings with big particles which were partially molten exhibit lower values of adhesion strength. However the decrease in adhesion strength for the highest roughness has no clear explanation except maybe that the

partially molten particles flatten the substrate peaks. In all cases the rupture was purely adhesive [81]. The abrasive cleaning of surfaces is a widespread indispensable method of surface preparation prior to plasma spraying. The most common way to remove grease is to use chemical solvents. Washing the parts or using the vapors of chemical solvents like trichloroethylene, perchlorethylene, acetone etc. can remove mineral oils. Generally, grit-blasting, which is the standard technique of surface roughening, is used to roughen surfaces.

2.5.4 Interlayers for Improving Adherence

By spraying special ceramic materials on clean and pretreated metallic substrates, a suitable underlayer for the next plasma sprayed coating can be obtained. Such interlayers are characterized by good adherence to the substrate and then these surfaces subsequently provide suitable conditions for good adherence of the next plasma sprayed coating. Moreover, interlayers compensate for the very different thermal expansion coefficients of the substrate and the material of the working layer by lowering the level of shear stresses formed on the boundary of substrate and the layer. The interlayers may also serve other specific purposes, e.g., protecting the substrate from corrosion, gas formation, the effects of high temperature, etc.. Generally $NiCrAlY$/ $NiCoCrAlY$ is selected as bond coating, as the CTE of which is about the average value of the CTE of ceramics and metals [45, 46, 62, 96, 102, 111, 114].

2.5.5 Working Parameters and Quality Control

There are a number of interrelated parameters (up to 200) that determine the characteristics of the resulting plasma sprayed coatings. These include: gas type, pressure and flow rate [37], power, spray distance, physical features of the feedstock powder, such as particle size and size distribution, particle shape and the level of chemical

uniformity of the constituents in a mixed oxide [50]. Size and shape of particles are particularly significant because the former is important for meltability considerations, while the shape of the particles will determine the flowability of the powder into the flame [40, 42, 55, 59, 77, 95, 108, 119, 129]. Critical process spray parameter (CPSP, defined as the gun power divided by the primary gas flow rate) is responsible for the microstructure and properties of plasma sprayed coatings [70]. Many of the properties of plasma sprayed coatings depend upon their microstructure, whilst the microstructure itself depends upon the mechanism of coating formation so microstructure is the common factor linking properties to processing details [42, 48, 73, 75, 78, 80, 106–108, 112].

Typical variable spraying parameters are listed as follows:

(1) Spraying power: typically up to 60 kW (in some installations, more than 100 kW) [95]. Adhesion strength of pure alumina coatings increases with an increase in power level [97]. When the power level is increased, the melting fraction and velocity of the particles will increase. Therefore there will be better splashing and mechanical interlocking of molten particles on the surface of the substrate, which enhances the mechanical properties of the coating (i.e., microhardness, young's modulus, fraction toughness, etc.). Usually vol.% of pores is decreased with an increase in power level [97].

(2) Spraying angle: typically, 90 °.

(3) Spraying distance: typically, 60 to 130 mm. 100 mm is selected normally.

(4) Powder size: The large size particles need large spraying power to melt them. The unmelted and partially melted particles may decrease adhesion strength and other mechanical performances of the coating [97]. Three grades of alumina powder with mean sizes of 25, 40 and 76 μm were sprayed under different injection velocities

and the microstructure was studied [32]. The results of microstructure and microhardness of the coatings reveal that, with spraying power of 31.5 kW (35 V, 900 A, spray torch model: SG-100) and particle injection velocity of 25 m/s, 25 μm is the best powder size.

(5) Powder feed rate: High feed rate leads to a coating with unmelted and partially melted particles, which decrease the mechanical performance of the coating [97].

The most important parameter that could govern the coating microstructure and the coating characteristics is the extent of particle melting [43,128]. The microstructure characterization can be made with a scanning electron microscope (SEM), X-ray diffraction, transmission electron microscope, mercury intrusion porosimetry or other techniques. The full coating microstructure description would contain the following information:

(1) Chemical composition in macro and micro scale,

(2) Grain morphology and its orientation (texture),

(3) Defects, such as voids or second phases or more rarely micro-defects such as stack faults or dislocations, content and their distribution, and

(4) The distribution of the above features in different depths of the coating.

2.6 Plasma Sprayed Alumina and Its Properties

Ceramic coatings, such as alumina coating and zirconia coating, are used in corrosion and wear protection, or thermal and electrical insulation, etc. [63,80,94,123]. It is mentioned that solar absorptance of alumina does not change after 1000 equivalent sun hours (ESH) UV radiation [41, 84]. Plasma sprayed alumina leads to a porous coating on a surface (when its porosity ratio is approximately 88%, the density is 510 kg/m^3, the thermal

conductivity is 0.605 $W/m \cdot K$, compressive strength is 6.41 MPa, and the highest working temperature is 2,090 K) [77]. Absorptance and emittance of alumina from literature are listed in Table 2.5. There are no data for absorptance or emittance available in literature for plasma sprayed alumina coating on Nickel powder coated aluminum substrates. However, it is known that the absorptance or emittance are influenced by the substrate material, as well as the coating thickness (See Figure 2.2, which shows that with the thickness increasing from 0.025 mm to 0.25 mm, the normal absorptance decreases 60% accordingly.) Although it was mentioned that the nonmetallic or dielectric materials were known to be less sensitive to surface conditions [115], dielectrics generally show a slight increase in emittance with roughness [110]. Some general properties of plasma sprayed alumina coating from literature are listed below in Table 2.6.

Table 2.5: Available literature data on absorptance and emittance of alumina

Absorptance	Emittance	Remarks
0.13	0.23	On buffed aluminum, without any change after 2560 ESH UV irradiation [15, 41]
0.12	0.24	On fused silica [41]
-	0.4-0.6	On silver-deposited stainless steel [115]
-	$\sim$ 0.76	At 273-400 K, on molybdenum substrate [115]
-	$\sim$ 0.84	At 366-400 K, on stainless steel substrate, flame-sprayed [115]
0.163	-	At 298 K, sapphire (0.1 m thick), aluminum and mill-finish aluminum alloy 6061-T6 substrate, vapor-deposited [115]
0.149	-	Above specimen except UV irradiated in vacuum at 533 K for 250 ESH and thermal cycled 10 times between 294 and 533 K [115]
0.2-0.5	-	Sapphire(0.025-0.25 mm thick), substrate unknown, flame-sprayed [115]
-	0.65-0.45	At 810-1370 K, on Inconel [110]

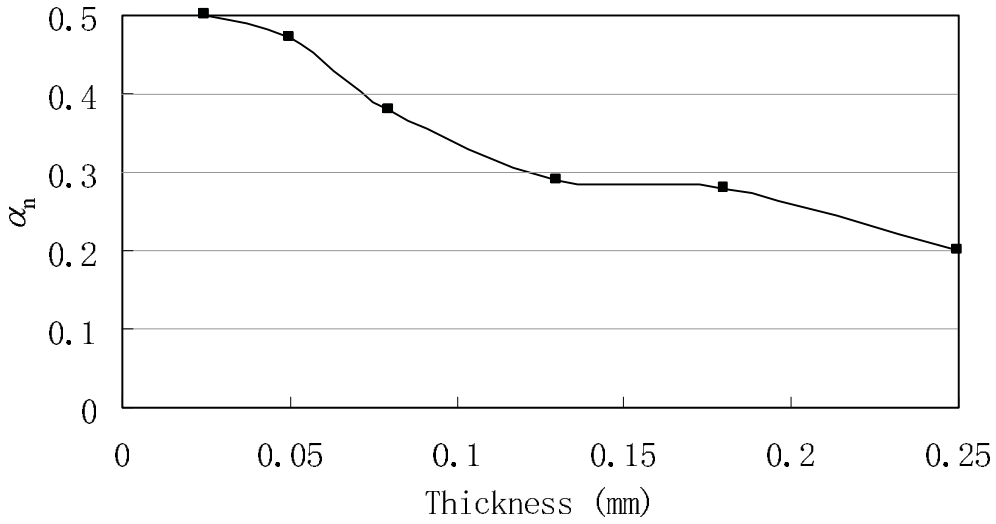

Figure 2.2: Normal absorptance vs thickness (Flame-sprayed sapphire on unknown substrate)

Table 2.6: General properties of plasma sprayed alumina coating

Property	Value	Remarks	Ref.
Young's modulus, GPa	70-80	$\sim$ 1/5 of bulk value ($\sim$370)	[61, 80, 90, 95]
	39	presumably tensile test on free-standing plate)	[117]
	20-40	99.6% alumina, -40+10 μm size powder, by 4-point bending	
Microhardness (H_{V3N}), MPa	600-1080		[16, 32, 39, 95]
Porosity	Usually 5-10 vol.%		[39]
	Up to 20 vol.%		[80, 123]
Fracture strength, MPa	138		[95]
CTE, $m/m/K$	7E-6@300-1300 K		[95]
Thermal conductivity, $W/m \cdot K$	1-4, typically		[95]
Density, kg/m^3	3400		[95, 118]
Tensile bond strength, MPa	52	R_a=2.6, alumina grit-blasting stainless steel substrate, 30 kW spraying	[49]
	32	R_a=0.6, HCl acid etched stainless steel substrate, 30 kW spraying	[49]
	33	R_z=18, spheres blasting mild steel substrate	[95]
	58	R_z=92, sand blasting mild steel substrate	[95]

Chapter 3

SUITABILITY OF PLASMA SPRAYED ALUMINA AS THERMAL CONTROL MATERIAL

Due to the dynamic conditions materials face in the harmful outer space, all new materials must be space-flight qualified prior to implementation on spacecraft. Testing new materials in simulated space environment prior to an actual space flight testing opportunity is the first step toward acceptance and transition to new materials. Information gained from the experiments could reduce screening and qualification costs for potential future spacecraft materials. Then, when a new material surpasses the current state-of-the-art performance criteria, the new material will be examined in orbital space flight tests. However, the extreme cost and limited availability of space flight testing greatly impede this stage of the acceptance process. Even small modifications in current state-of-the-art materials, such as changing a raw material supplier or imposing a material processing change, will require satellite manufacturers to initiate a requalification program to ensure that the new version of the same material performs at least as well as the previous one. The promising new materials should offer weight, performance, and cost-saving benefits-characteristics that are critical to the adoption of new materials to space systems.

As such, the plasma sprayed alumina coating should follow the same qualification procedure. Suitability of plasma sprayed alumina coating as TCM was established by three means: literature, numerical simulations and some experiments in simulated environment.

3.1 Literary Evidence

In order to determine suitability of plasma sprayed alumina coating as TCM, its physical and thermal properties were firstly examined. It was found suitable as TCM in comparison to the other traditional TCMs due to the following attributes:

3.1.1 Physical Properties

Plasma sprayed alumina coating is whitish in color similar to $Z93, YB71$, and $S13G$-LO, which are commonly used in existing satellites. The density of alumina coating is $\sim 3400\ kg/m^3$ [35, 113, 118, 119], about two times of the density of $Z93$, which might be a drawback for alumina coating, if the coating thickness is not properly controlled.

The durability of plasma sprayed alumina coating is much better than the conventional paints and some coatings, in terms of impact resistance and adherence. The alumina coating has a Young's modulus of $\sim 80\ GPa$, approximately 1/5 of the bulk alumina ($\sim 400\ GPa$) [90]. It has approximately the same elastic modulus as aluminum ($\sim 70\ GPa$).

The coefficient of thermal expansion (CTE) of alumina is 7E-6 $m/m/^{\circ}C$ as compared to 24E-6 $m/m/^{\circ}C$ of aluminum, which is about 3.5 times higher than that of alumina. The differential expansion coefficient is not as severe as compared to aircraft engine applications. A bond coat layer, such as $NiCrAlY/\ NiCoCrAlY$ and aluminum powder, whose CTE is about the average of the CTE of ceramics and metals, is normally sprayed on the substrate to provide good adherence between the substrate and the

ceramic coating. The bond coat compensates for differential CTE of the substrate and ceramic coating thus lowering the level of shear stresses at the boundary of substrate and the ceramic coating [46].

3.1.2 Thermal Properties

The α_n for alumina is in the range from 0.12 to 0.50 [15,41,115], compared to $Z93$ paint, which varies between 0.19 and 0.37 [41,110,115]. The ϵ_h for alumina ranges between 0.23 to 0.84 [15,41,110,115], while for $Z93$, it is $\sim$ 0.87 [41,110,115]. Thus, the values of both, α_n and ϵ_h parameters indicate that alumina is a kind of suitable TCM. Most importantly, the absorptance and emittance of alumina do not change after a long exposure to solar flux. Two records [41, 84] show that 2300-ESH UV irradiation had no effect on the absorptance or emittance of alumina.

Effects of AO on plasma sprayed alumina coating are not very clear at this stage. One evidence showed that mullite ($2Al_2O_3 \cdot SiO_2$) coating did not show any degradation in absorptance α or emittance ϵ after 6h exposure to cold plasma as effective AO flux [104]. However, it was found that AO leads to severe erosion of TCMs like $S13G$-LO followed by a large increase in its α_n [58]. Experimental results show that the total increase of α_n is 47%, 67% and 100% for $Z93$, YB-17 and $S13G$-LO respectively [41]. Such significant increase in α_n limits their applications, and moreover, such changes in α_n are often unpredictable.

Thermal conductivity of plasma sprayed alumina coating is in the range 1 to 4 $W/m \cdot K$ [95], which is much higher than that of similar TCM $Z93$ (0.2 $W/m \cdot K$ [109]). Although thermal conductivity of plasma sprayed alumina coating is relatively higher, the simulation results reported in section 4 reveal that the thermal stress in a panel with plasma sprayed alumina coating is well within the acceptable range.

3.1.3 Outgassing and Weight Loss

Alumina ceramics are exclusively used today for vacuum applications [124]. In general, a ceramic component of vacuum facility should be baked at 450 $^{\circ}C$ for several hours in the final system to complete outgassing. The resulting outgassing rate at room temperature is of the order 10^{-11} W/m^2 or better [124]. There is no organic element in plasma sprayed alumina coating, thus contamination caused by such coating is not a problem for a micro-satellite in comparison with the conventional TCMs.

3.2 Verifying Experiments

The experiments were limited to the available facilities. Thus the complete testings prior to flight cannot be achieved. The tested coating properties include: panel warping measurements before and after plasma coating process, microhardness of the coating, outgassing measurements in high temperature vacuum, total normal solar absorptance and total hemispherical emittance measurements, coating surface profile scanning. Prior to the coating properties measurements, the plasma spraying technique was studied and the optimized spraying parameters were applied for spraying alumina coating. The warping, mainly due to thermal stress induced by the high temperature of plasma spray process, is quantified by

$$\frac{\text{Maximum out} - \text{of} - \text{plane deflection}}{\text{Length of the plate}} \times 100\% \tag{3.1}$$

Pretreatment such as grit blasting and bond coat spraying also caused warping, which was up to 1%. After single-sided plasma spraying, the warping was about 1.5%. After double-sided plasma spraying, warping reduced to about 0.39%. The performance of the panel will not be affected from the point of view of tolerance. Such small warping is a non-issue for traditional coating applications. In order to reduce the warping induced

by the spraying process, double-sided coating should be used wherever necessary and possible.

The other coating properties, namely, microhardness, outgassing in high temperature vacuum, total normal solar absorptance and total hemispherical emittance measurements, were measured and found to be suitable as TCM.

3.3 Supportive Simulations

To understand the in-service behavior of the plasma-sprayed-alumina-coated panels, transient heat transfer and stress analyzes were carried out to predict $T_{\min}$ and $T_{\max}$, the corresponding thermal stresses and deflections of the panels when subjected to space thermal environment experienced by a satellite in LEO, by a general-purpose FE analysis package LUSAS with the help of user-written C program. The results showed that $T_{\max}$ of the plasma-sprayed-alumina-coated aluminum panel in LEO thermal environment are safe for satellite operation. $T_{\min}$, however, vary with each other due to different coating thickness. The corresponding thermal stresses do not vary significantly.

Deflection caused by thermal stress is not a problem. For example, the largest deflection in a 100 mm-long, 2 mm-thick aluminum square panel, with 0.1 mm-thick bond coating and 0.1 mm-thick alumina coating, were 0.086 mm (0.086%) in its longitudinal and transverse directions, and 0.007 mm (0.007%) in its thickness direction. Higher defections than these are reported in the literature for a micro-satellite mission. For example, the maximum out-of-plane deflection along the center line of the 2670mm-long solar array on a Korea Multi-Purpose Satellite was stated as 18.52mm (0.69%) with no further mission problems reported by such deflection. This array was made of a honeycomb with aluminum facesheets. The deflection reduced from 0.07% to 0.15% when the aluminum was replaced by composites. Both deflections were in the safe range [109].

3.4 Conclusion

It was observed in this study that plasma sprayed alumina coating has potential to be used as TCM for LEO satellites. The reasons are:

(1) Reduced or little outgassing because of no organic element used;

(2) More predictable behavior as $\frac{\alpha}{\epsilon}$ ratio is suitable as TCM and is less likely to degrade;

(3) This coating works as not only radiation TCM, but also as a thermal insulation layer; and

(4) It can withstand severe thermal shocks. The warpage induced during the manufacturing process is a minor issue. However, further studies are needed to make application of plasma sprayed alumina coating as TCM more attractive and acceptable (as presented in section 8.2). Furthermore, the thickness of both substrate and alumina coating can be optimized by numerical simulation, which will help in designing better desired thermal control for a satellite. The thermal stress developed within the coated panel in LEO thermal environment is found to be very small and well within the safe range.

Chapter 4

EXPERIMENTAL WORK

As mentioned in chapter 3, some experiments are required to prove the suitability of plasma sprayed alumina coating as TCM. The necessary experimental work includes plasma spraying of alumina coating on aluminum alloy plates, warping measurements of the plasma-sprayed-alumina-coated aluminum alloy panels, microhardness measurements of the coating on aluminum alloy substrate, surface profile scanning of alumina coating surfaces to study light absorption and reflection, solar normal absorptance and IR emittance measurements of alumina coating and vacuum outgassing tests of alumina coating. The purpose was to examine the coating's behavior under space-like conditions. All the samples needed for different experimental purposes were sprayed under the same conditions at the same time.

The facilities used and testing standards adopted are described in detail. The results and discussions are presented at the end of the section describing each experiment.

4.1 Plasma Spray and Warping Measurements

Plasma spraying of ceramic coatings has been well established as a commercial process over about 40 years. However, it is mostly used for spraying thermal barrier coatings. For space applications, particularly for thermal control of a micro-satellite, some new issues must be considered. The primary concerns are the warping (quantified by the ratio of the

maximum out-of-plane deflection to the length of the plate $\times 100\%$) of thin substrates due to the high temperature of the process and the effects of the surface roughness on the radiation properties, which is a dominant mode of heat transfer in space.

In order to study such warping systematically, three cases namely, initial warping (i.e., warping before spraying alumina coating onto the aluminum alloy plate), warping after single-sided plasma sprayed alumina coating and warping after double-sided plasma sprayed alumina coating, were studied experimentally and the effects were compared with each other.

4.1.1 Plasma Spray Facility

The plasma spray system (manufactured by Miller Thermal Inc.) consists of a power supply, a heat exchanger, a plasma spray gun, a control console and a rotor-feed powder hopper. The SG-100 spray gun has an interchangeable, water-cooled, self-aligning electrode for multi-mode plasma spray gun, which normally operates at 40 kW and has the ability to operate beyond this limit, i.e. up to 80 kW. The control console has critical orifices built into the gas circuits to control the gas flow of primary gas, secondary gas as well as powder carrier gas to achieve satisfactory accuracy and repeatability that can hardly be achieved by other commonly used methods, such as glass tube flowmeters and mass flow controls. The control console regulates electrical power, plasma gas flow, and cooling water and sequences these parameters to initiate the process. The rotor feed hopper is pressurized and electronically controlled to produce an accurate and consistent feed rate. It operates on a volumetric principle and feed rate to the plasma spray gun. The powder is fed into the powder hose and is carried to the plasma gun by the carrier gas. The delivery speed of powder to the plasma spray gun is governed by the speed of the powder wheel. A computerized feed rate control panel and closed-loop control of the

feed rate is integrated into the system to further improve the feeding accuracy. It has a digital display to indicate the exact speed of the powder wheel.

4.1.2 Warping Measurement Facility

The warping measurements were carried out using a bridge-type 3D multi-sensor measuring center (supplied by WEGU Messtechnik GmbH, Germany). It consists of 3 subsystems: (a) Measuring system: linear glass scales, having 0.1 μm resolution, with automatic temperature acquisition and compensation, (b) Laser probe system: providing high-speed single point measurement (0.1 s) and dynamic surface scanning (5000 $points/s$), and (c) Air supply system: pressurized air at 600-1000 kPa, filtered and free from oil and water.

4.1.3 Materials, Spray Parameters and Sprayed Samples

In order to prepare the necessary test samples, nickel powder, alumina powder, and aluminum alloy 6061-T6 substrate plates were required. These materials are commonly used for plasma spray. The alumina powder was to be used as the final coat. The nickel powder was to be applied over the grit blasted substrate as a bond coat to compensate for the CTE mismatch and to increase the adhesive ability between the alumina coating and the substrate. Aluminum alloy 6061-T6 is commonly used as the main metal substrate material for coatings and films in space applications due to its excellent joining characteristics and good adherence of applied coatings, and the common thickness used is 2 mm.

The sintered alumina powder (Praxair ALO-101, -325 mesh, which is smaller than 45 μm)and ATOMIZED nickel powder (Praxair NI-171, proprietary size) were both supplied by Praxair Surface Technologies Inc. The aluminum alloy substrates were cut

to a size 300 $mm \times 300$ mm and its thickness was 2 mm, which are general dimensions commonly suitable for a micro-satellite.

Grit blasting of both surfaces of the substrates were carried out to get a rough texture for better adhesion (reasons discussed in section 2.5.3). The roughened surface was then thoroughly cleaned with acetone before spraying to remove fine particles of sand.

After feeding the powder, the aluminum alloy substrate was mounted to the substrate holder at its center by a screw so that thermal expansion will not be restricted during the high-temperature spraying process. The spraying parameters were optimized, as presented in Table 4.1 [32]. For all necessary experiments, 15 sprayed samples were prepared, as listed in Table 4.2.

Table 4.1: Spraying parameters for bond coat and alumina coat

Spraying parameter	Nickel powder (bond coat)	Alumina powder (top coat)
Arc Current (A)	850	900
Plasma Gas (kPa), Argon	600	600
Carrier Gas (kPa), Argon	300	300
Spray Distance (mm)	120	120
Powder Feed Rate (rpm)	3	3
Traverse Speed (mm/s)	400	500
Pitch ($mm/step$)	5	5

Table 4.2: Plasma sprayed alumina samples prepared

Sample Label	Purpose	Dimension (mm)
S-PSA-01	Warping measurement	304.8 × 304.8
S-PSA-02	Microhardness tests	50 × 50
S-PSA-03, -04, -05, -06	Absorptance and emittance measurement and surface profile scanning	50 × 50
S-PSA-07, -08, -09, -10, -11, -12	Vacuum outgassing test	50 × 50
S-PSA-13,-14, -15	Additional coupons to supplement, if needed	50 × 50

4.1.4 Warping Measurements

The specimen preparation and warping measurements were carried out in the following sequence:

(1) Grit blast the plate, clean surfaces with acetone and mount the plate for spraying,

(2) Spray bond coat (nickel powder) on surface $S1$ of the substrate,

(3) Turn over the plate, mount it and spray (nickel powder) on the other surface, $S2$, of the substrate,

(4) Measure the warping on surface $S1$,

(5) Spray alumina powder on surface $S1$,

(6) Measure the warping on surface $S1$,

(7) Spray alumina powder on surface $S2$, and

(8) Measure the warping on surface $S1$.

The illustration for plasma spraying is presented in Figure 4.1. The curvature measurements were carried out by scanning the midline of the panel, as shown in Figure 4.2. The WEGU machine provides X and Z coordinates of a measurement. These coordinates were leveled and plotted for comparison.

4.1.5 Results and Discussions

The average bond-coat thickness was 125 μm and the average alumina coat thickness was 135 μm. They were measured by the SEM picture of the cross section of the sample, as presented in Figure 4.3. Figure 4.4 shows warping of one of the aluminum panels with alumina coating on one side and both sides. The warping developed mainly due to

thermal stress induced by the high temperature of the plasma spray process, i.e., about 15,000 K. Pretreatment such as grit blasting and bond coat spraying also caused warping, which was up to 1% of the plate length dimension. After single-sided alumina spraying, the warping was about 1.5%. With double-sided alumina coating, warping reduced to about 0.39%. The performance of the panel will not be affected from the point of view of tolerance. Such small warping is a non-issue for traditional coating applications. In order to reduce the warping induced by the spraying process, double-sided coating should be used wherever necessary and possible.

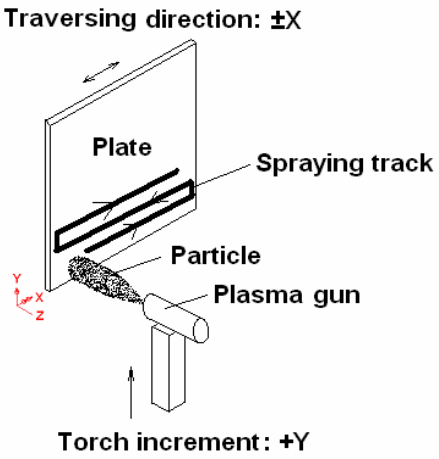

Figure 4.1: Illustration showing plasma spraying

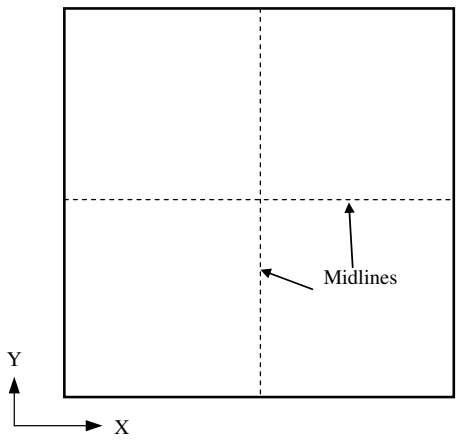

Figure 4.2: Illustration for curvature measurement

4.2 Microhardness and Young's Modulus Measurements

Microhardness and Young's modulus are general mechanical properties that are necessarily to be measured. Young's modulus is also needed for the numerical simulations. Microhardness testing is an indentation method for measuring the hardness of plasma

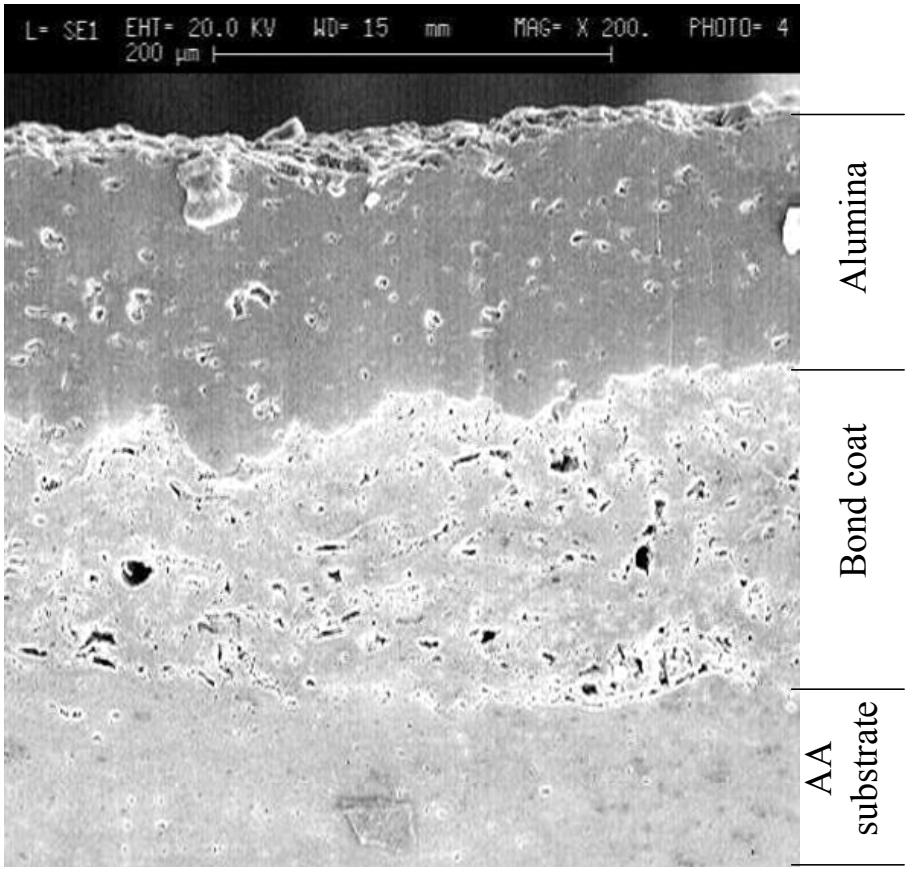

Figure 4.3: Thickness measurements for bond coat and alumina coat

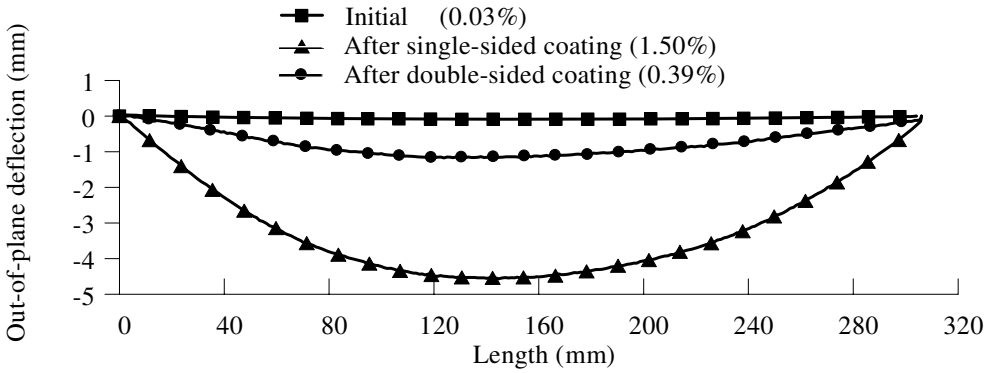

Figure 4.4: Warping of an aluminum panel with plasma sprayed alumina coating on one side and both sides

sprayed alumina coating on a microscopic scale. The indentation method was used to get the Young's modulus of the porous plasma sprayed coatings by many researchers; for example refer [65, 74, 90, 121]. Hardness of alumina coating is an important parameter because the coating must survive the intense launch vibrations and withstand as many impacts by MMOD as possible during the design service life.

4.2.1 Microhardness Tester

The microhardness tester (supplied by CSM Instruments SA, Switzerland) provides Vickers hardness and allows direct readings of microhardness and Young's modulus of almost any type of material: soft, hard, brittle or ductile. It covers a wide load range from 10 mN to 30 N. This load range permits measurements of coatings down to 1 or 2 μm without being influenced by the substrate materials [29].

This microhardness tester works on the principle in that an the indenter tip made of diamond, with a known geometry, is pressed on the coating material under a normal load that increased continuously up to a designated level. The load was then gradually decreased to 0. The entire loading and unloading processes were recorded continuously throughout this process, resulting in a load-displacement curve. Hardness and Young's modulus are automatically determined by software during this process, based on the attained stiffness of contact, contact depth and projected contact area.

4.2.2 Description of the Test

The specimen is a plasma-sprayed-alumina-coated aluminum panel of 50 $mm \times 50$ $mm \times$ 1.5 mm (chosen dimensions for easy assembly in microhardness tester). The average coating thickness is 135 μm, as mentioned in section 4.1.5 (page 36). The coating was carefully polished to grade 1 μm as required for accurate measurement and indentation was followed on the polished surface. The microhardness and Young's modulus were automatically calculated and provided by the software associated with the MHT.

4.2.3 Results and Discussions

The microhardness of alumina coating is $H_{V3N} = 692\ MPa$ (Vickers hardness, with 3 N loading), which is average of 8 tested values and standard deviation is 126. The coating is much harder than the thermal control paints. The Young's modulus of the coating is 81.4 GPa (approximately 1/5 of the bulk alumina, $\sim$400 GPa) which is an average of 9 tested results and the standard deviation is 14.4. It has approximately the same elastic modulus as aluminum, which is $\sim$ 70 GPa. The minimum 61 GPa and maximum 95 GPa tested values were used as lower and upper bound values for each case of stress analysis. The measured microhardness and Young's modulus were consistent with the literature values. The results also reveal that the spraying conditions can produce good coatings.

4.3 Surface Profile Scanning

The surface profiles of plasma sprayed alumina coating were scanned to obtain the surface characteristics. The scanned results are X and Z coordinates which are provided in a data file for one scan.

4.3.1 Talyscan 150 Facility

The dedicated surface topography system Talyscan 150 (supplied by Taylor Hobson, Great Britain) provides high-speed 3D scanning (97 $mm \times 97\ mm$) for surfaces. The user can choose non-contact laser scanning (10 mm range) and /or inductive gauge scanning (2.5 mm range). The instrument was supplied with Talymap 3D analysis software. The maximum scanning speed is 10 mm/s. The minimum interval in X, Y and Z direction is 0.5 μm, 1 μm and 0.1 μm respectively. The specimen was carefully mounted onto the specimen holder using plasticine, which cannot ensure that the sample is held on the

horizontal plane. However, the scanned results can be leveled using Talymap 3D analysis software.

4.3.2 Scanning Output

The output can be plotted to pseudo color image (2D, example shown in Figure 4.5) or meshed axonometric image (3D, example shown in Figure 4.6). Coordinates of scanned points can also be exported in ASCII format (example shown in Figure 4.7). Two samples (S-PSA-03 and S-PSA-04) were scanned with X-interval of 0.5 μm and Y-interval of 1 μm. From the scanned data, 2D profile can be extracted between any two points of the scanned surface.

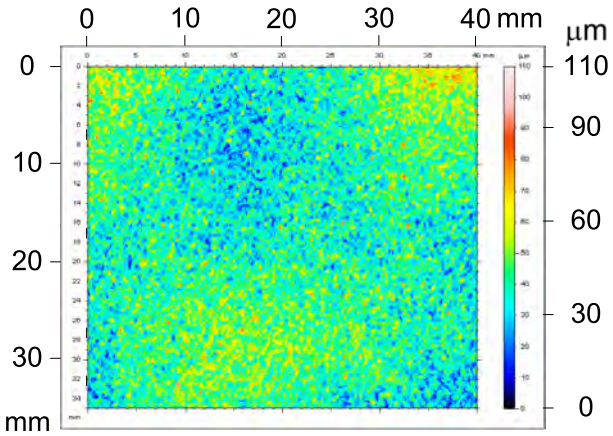

Figure 4.5: Pseudo-color image of plasma sprayed alumina coating surface

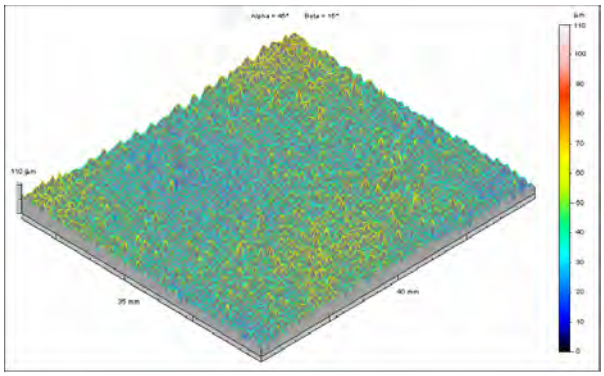

Figure 4.6: Meshed axonometric image of plasma sprayed alumina coating surface in Figure 4.14

4.4 Absorptance (α_n) and Emittance (ϵ_h) Measurements

Radiation property measurements were carried out for many purposes:

(1) Get the actual experimental values measured as per the spacecraft standards,

(2) Obtain the properties for numerical simulations, and

(3) Validate the surface radiation properties models.

Four samples were prepared, as listed in Table 4.3. The property measurements were carried out by Sheldahl (Sheldahl Inc., USA), because Nanyang Technological University does not have such special facilities and there was no ongoing major project for procuring such facilities. Furthermore, the measurements should be done according to special standards, such as ASTM-E-490 and ASTM-E-408, etc..

1001 lines, with a spacing 5.000 µm
8001 points by lines, with a spacing of 3.5004 µm
The values are in nm

3730.875556	2845.414424	2293.244842	2243.499835	3019.521950	3133.935467
4059.192605	3004.598448	2626.536392	2944.904439	3676.156048	3919.906585
4715.826703	3870.161577	3362.762501	3059.317956	3591.589536	3536.870027
6367.360950	4785.469714	3979.600593	3591.589536	3417.482010	3238.399983
5989.298893	4899.883231	4183.555124	3800.518567	3621.436540	3521.946525
5571.440831	5019.271248	4467.101666	4248.223634	3865.187076	3730.875556
5481.899817	4969.526241	4671.056197	4243.249133	4188.529625	4223.351130
5476.925317	5253.072783	4914.806733	4820.291219	5307.792292	5586.364333
5840.063871	5541.593826	5362.511800	5850.012872	5218.251278	5078.965257
6208.176926	6203.202425	7809.966165	7675.654645	7163.281068	6029.094899
6705.627000	6944.403036	7591.088132	8292.492737	8401.931753	7392.108102
6949.377536	6725.525003	7551.292126	8033.818698	8312.390740	8347.212245
6899.632529	6471.825465	6670.805495	7073.740055	7352.312096	7551.292126
8511.370769	8048.742200	6745.423006	6735.474004	6725.525003	6879.734526
7839.813169	8043.767700	8277.569234	7392.108102	6511.621471	6332.539444
6720.550502	6705.627000	6611.111486	6267.870935	5342.613797	5536.619326
6257.921933	6242.998431	6849.887521	7178.204570	5914.681382	5576.415332
5959.451889	7606.011634	9302.316387	8456.651261	8113.410710	7685.603646
6451.927462	8387.008251	8088.538206	7038.918550	7073.740055	6516.595972
7317.490591	7267.745584	6546.442976	6118.635912	5695.803349	5098.863260
6063.916404	5969.400890	5914.681382	5785.344363	5854.987373	5755.497358
5352.562798	5675.905346	5660.981844	5486.874318	5347.588297	5258.047284
7426.929608	7660.731142	6864.811024	5521.695823	5591.338834	6247.972932

Figure 4.7: Coordinate data sample

4.4.1 Test Facilities and Test Methods Used by Sheldahl

Total normal solar absorptance α_n was tested using Perkin Elmer Lambda 9 spectrophotometer, as shown in Figure 4.8 [13]. This instrument can record data from wavelength of 185 to 3200 nm, was computer controlled and has data processing capabilities. It uses a 6.0-in diameter integrating sphere. The incident beam impinges on the sample at 8 degrees from normal. Total normal solar absorptance α_n was computed based on 25 equal energy intervals centered on wavelengths from 314 nm to 2191 nm. The wavelengths were computed from tables of spectrum NASA SP-8005 [2] and ASTM-E-490-73a [7].

Total hemispherical emittance ϵ_h was tested by the AZ Technology TEMP 2000A Portable Emissometer, which provides a portable reflectometer/ emissometer [13] that performs total hemispheric reflectance measurements from less than 3 μm to greater than 35 μm wavelength. It is not limited in wavelength range due to filters, windows, or coatings in the optical path. Its measurement accuracy is $\pm 3\%$. The standard followed was ASTM-E-408, Method A [1].

Table 4.3: Specimens for absorptance and emittance measurements

Specimen ID	Surface Condition
SMP-PSA-03	As sprayed
SMP-PSA-04	800-grit ground
SMP-PSA-05	As sprayed
SMP-PSA-06	800-grit ground

Figure 4.8: Perkin Elmer Lambda 9 spectrophotometer (Courtesy of Sheldahl)

4.4.2 Results and Discussions

The test results obtained are presented in Table 4.4 and the original test report is shown in Appendix A. The difference between α_n values for as-sprayed and ground samples showed that the coating surface roughness plays an important role for α_n. However, the roughness did not affect ϵ_h too much. Both of the measured quantities were in the same range as found in the literature, i.e., α_n=0.12-0.50, ϵ_h=0.23-0.84, as shown in Table 2.5.

4.5 Vacuum Outgassing Tests

Plasma sprayed alumina coatings are not expected to outgas as severely as polymer-based TCMs do. However, vacuum outgassing test was conducted to confirm and arrive at a quantitative assessment.

4.5.1 Vacuum Tube Furnace Facility and Test Standards for Vacuum Outgassing

The only available facility for the outgassing characteristic test is the vacuum tube furnace CARBOLITE supplied by TriTech Scientific Pte Ltd, which provides maximum tube furnace operating temperature of 1600 $^{\circ}C$. The vacuum level provided is better than 10^{-2} Pa with a clean empty worktube.

There are two standards available for examining outgassing characteristics of a sample, (1) ECSS-Q-70-02A [8] (Space product assurance: thermal vacuum outgassing test for the screening of space materials, 26 May 2000) and (2) ASTM E595 [4] (Total mass

Table 4.4: Total normal solar absorptance (α_n) and total hemispherical emittance (ϵ_h) measurement results

Specimen	α_n	ϵ_h	Surface condition
S-PSA-03	0.318	0.801	As sprayed
S-PSA-04	0.250	0.795	800-grit Ground
S-PSA-05	0.301	0.810	As sprayed
S-PSA-06	0.243	0.795	800-grit Ground

loss and collected volatile condensable materials from outgassing in vacuum environment, 1993). ECSS-Q-70-02A specifies the test conditions of 24 h at temperature 125 $°C$ and vacuum $\leq 1E-3$ Pa. ASTM E595 recommends conditions of vacuum $\leq 7E-3$ Pa and 24 h test at the temperature 125 $°C$.

4.5.2 Samples and Tests

Only total mass loss (TML) is measured for all specimens. For comparison, another three kinds of coated substrates (i.e., anodized aluminum, Kapton-coated aluminum and Kapton-coated alodined aluminum) were used, which are shown in 4.9. Because the vacuum level could only reach 1E-2 Pa (but not too far from 7E-3 Pa), the temperature is adjusted to 300 $°C$ and time extended to 30 h, instead of 125 $°C$ and 24 h respectively as recommended. The new conditions were derived according to the ideal gas law:

$$\frac{PV}{T} = \text{Constant}$$

In which,

P- absolute pressure, Pa,

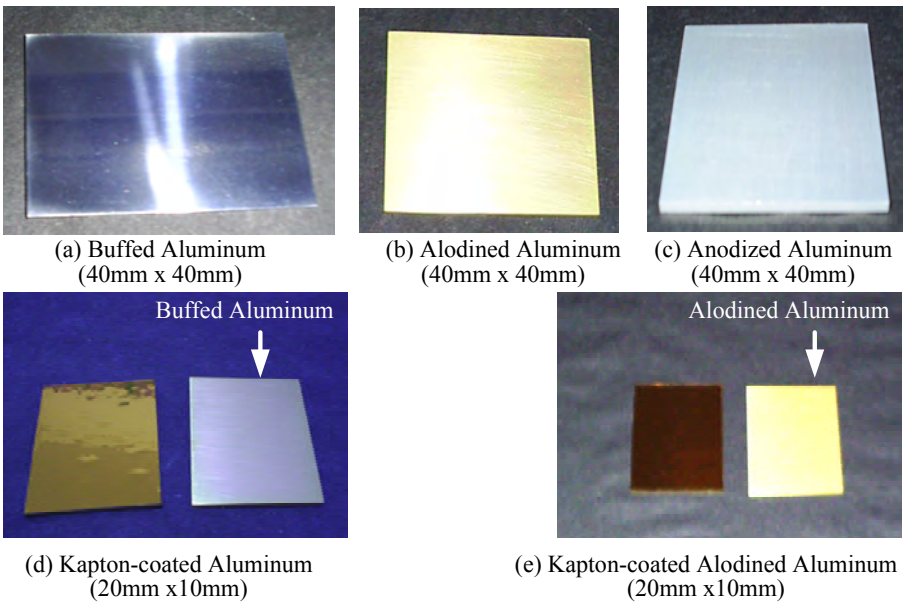

(a) Buffed Aluminum (40mm x 40mm)
(b) Alodined Aluminum (40mm x 40mm)
(c) Anodized Aluminum (40mm x 40mm)
(d) Kapton-coated Aluminum (20mm x10mm)
(e) Kapton-coated Alodined Aluminum (20mm x10mm)

Figure 4.9: The samples for outgassing test

V- volume, m^3,

T- absolute temperature, K.

Since the pressure P=1E-2 Pa was raised from P=7E-3 Pa, the temperature $T = 125\ ^{\circ}C$ was elevated to $T = 300\ ^{\circ}C$, a more critical testing condition. To ensure the experimental conditions meet the testing standard, duration was extended from 24 h to 30 h. Although the ideal gas law could not be simply employed to arrive at higher temperature to compensate for the higher vacuum, and the temperature to a large extent will determine the decomposition and deterioration of a substance, with pressure playing a relatively minor role, the experiment can be compensated by increasing the temperature and duration of testing time.

Six types of thermal control surface finish were compared using aluminum alloy 6061-T6 as substrate. Raw aluminum was also examined for the purpose of calculating TML for coatings/ films. The six types of surface finish were: plasma sprayed alumina coating surface, buffed aluminum surface, alodined aluminum surface, anodized aluminum surface, Kapton surface and Kapton-coated alodined surface. The samples of alodined aluminum, anodized aluminum, Kapton-coated aluminum and Kapton-coated alodined aluminum were tested by a co-student [25] and the specimen preparations were mentioned in section 2.3. For each type of sample, six specimens (50 $mm \times 50\ mm \times 1.5\ mm$) were prepared and tested. All the seven types of samples were examined at the same time for mass loss; they were weighed 5 times to get the average value for each sample, before and after vacuum baking. The buffed aluminum plates were manually polished to roughness level of 1 μm, according to the standard NASA MIL-C-87936 type I document.

4.5.3 Results and Discussions

The results were compared in view of percentage loss for coatings/ films. TML for raw aluminum and buffed aluminum panels are shown in Table 4.5 and Table 4.6 respectively. Results for plasma-sprayed-alumina-coated aluminum, alodined aluminum, anodized aluminum, Kapton-coated aluminum and Kapton-coated alodined aluminum are presented in Tables 4.7, 4.8, 4.9, 4.10 and 4.11 respectively. The meaning for every specimen ID is as follows (The capitals were used to name the specimen IDs):

Table 4.5: Vacuum baking test results for raw aluminum

Specimen ID	Wt. before Vacuum Baking (g)	Wt. after Vacuum Baking (g)	Percentage Wt. Loss (%)
SMP-VB-RAL1	9.56543	9.56500	0.005
SMP-VB-RAL2	9.59197	9.59159	0.004
SMP-VB-RAL3	9.55622	9.55594	0.003
SMP-VB-RAL4	9.47345	9.47283	0.007
SMP-VB-RAL5	9.73758	9.73721	0.004
SMP-VB-RAL6	9.55681	9.55637	0.005
Avg.	9.58024	9.57982	0.005

Table 4.6: Vacuum baking test results for buffed aluminum

Specimen ID	Wt. before Vacuum Baking (g)	Wt. after Vacuum Baking (g)	Percentage Wt. Loss (%)
SMP-VB-BAL1	6.10910	6.10872	0.006
SMP-VB-BAL2	5.91740	5.91707	0.006
SMP-VB-BAL3	5.56421	5.56400	0.004
SMP-VB-BAL4	6.19771	6.19745	0.004
SMP-VB-BAL5	6.26731	6.26709	0.004
SMP-VB-BAL6	6.15431	6.15413	0.003
Avg.	6.03501	6.03474	0.005

Table 4.7: Vacuum baking test results for plasma-sprayed-alumina-coated aluminum

Specimen ID	Wt. before Vacuum Baking (g)	Wt. after Vacuum Baking (g)	Percentage Wt. Loss (%)
SMP-VB-PSA1	13.58550	13.58194	0.02
SMP-VB-PSA2	13.62111	13.61709	0.03
SMP-VB-PSA3	13.42440	13.42027	0.03
SMP-VB-PSA4	13.32163	13.31828	0.02
SMP-VB-PSA5	14.14032	14.13448	0.04
SMP-VB-PSA6	12.92411	12.91960	0.03
Avg.	13.50285	13.49861	0.03

Table 4.8: Vacuum baking test results for Alodined aluminum

Specimen ID	Wt. before Vacuum Baking (g)	Wt. after Vacuum Baking (g)	Percentage Wt. Loss (%)
SMP-VB-AL1	6.27439	6.27271	0.02
SMP-VB-AL2	6.13013	6.12847	0.02
SMP-VB-AL3	6.28433	6.28269	0.02
SMP-VB-AL4	6.00015	5.99845	0.02
SMP-VB-AL5	6.18989	6.18824	0.02
SMP-VB-AL6	6.26113	6.26010	0.01
Avg.	6.19000	6.18844	0.02

Table 4.9: Vacuum baking test results for anodized aluminum

Specimen ID	Wt. before Vacuum Baking (g)	Wt. after Vacuum Baking (g)	Percentage Wt. Loss (%)
SMP-VB-AN1	6.22610	6.22460	0.02
SMP-VB-AN2	5.97263	5.97138	0.02
SMP-VB-AN3	6.12866	6.12792	0.01
SMP-VB-AN4	6.09853	6.09757	0.01
SMP-VB-AN5	6.22026	6.21892	0.02
SMP-VB-AN6	6.02231	6.02098	0.02
Avg.	6.11142	6.11023	0.02

Table 4.10: Vacuum baking test results for Kapton-coated aluminum

Specimen ID	Wt. before Vacuum Baking (g)	Wt. after Vacuum Baking (g)	Percentage Wt. Loss (%)
SMP-VB-K1	5.61603	5.57823	0.67
SMP-VB-K2	6.37623	6.33345	0.67
SMP-VB-K3	6.26080	6.22892	0.51
SMP-VB-K4	5.91637	5.88668	0.50
SMP-VB-K5	6.29942	6.26953	0.47
SMP-VB-K6	6.41203	6.38034	0.49
Avg.	6.14681	6.11286	0.55

Table 4.11: Vacuum baking test results for Kapton-coated alodined aluminum

Specimen ID	Wt. before Vacuum Baking (g)	Wt. after Vacuum Baking (g)	Percentage Wt. Loss (%)
SMP-VB-KAL1	6.64037	6.61942	0.31
SMP-VB-KAL2	6.27992	6.24595	0.54
SMP-VB-KAL3	6.45960	6.43537	0.37
SMP-VB-KAL4	6.09075	6.06533	0.41
SMP-VB-KAL5	6.44696	6.42493	0.34
SMP-VB-KAL6	6.43058	6.40933	0.33
Avg.	6.39136	6.36672	0.38

SMP-VB-RAL1: SaMPle-Vacuum Baking-Raw ALuminum No. 1

SMP-VB-BAL1: SaMPle-Vacuum Baking-Buffed ALuminum No. 1

SMP-VB-PSA1: SaMPle-Vacuum Baking-Plasma Sprayed Alumina No. 1

SMP-VB-AL1: SaMPle-Vacuum Baking-ALodined aluminum No. 1

SMP-VB-AN1: SaMPle-Vacuum Baking-ANodized aluminum No. 1

SMP-VB-K1: SaMPle-Vacuum Baking-Kapton-coated aluminum No. 1

SMP-VB-KAL1: SaMPle-Vacuum Baking-Kapton-coated ALodined aluminum No. 1

Comparison of average percentage loss for the five kinds of coated substrates is shown in Figure 4.10. The mass loss of plasma-sprayed-alumina-coated panel is negligible. Outgassing of plasma sprayed alumina coating in such a small amount (0.03%) will not contaminate any satellite components, because of its amount and inorganic nature.

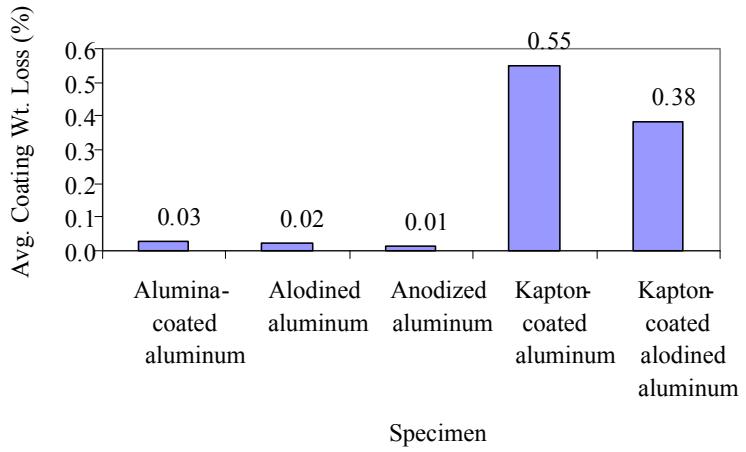

Figure 4.10: Comparison of average percentage loss for five kinds of coated substrates

Chapter 5

NUMERICAL SIMULATION

As further investigation, finite element method (FEM) was applied to study the in-service thermomechanical behavior of the plasma sprayed alumina coating, including temperature variation, stress distribution and effect of the thickness of both substrate and coating on the stabilized temperature and stress distribution in plasma-sprayed-alumina-coated aluminum substrates.

As mentioned in chapter 2 (page 5), solar panels must remain within their temperature tolerance so that they have less distortion and solar cells have better and uniform output. As such, other satellite surfaces should maintain temperature within the specified limits. This is only possible through the use of suitable and reliable TCM. In order to understand the thermal and structural behavior of plasma-sprayed-alumina-coated panels in LEO environment, coupled thermomechanical analyses were carried out. The purpose was to predict the maximum temperature ($T_{\max}$), minimum temperature ($T_{\min}$) and maximum Von Mises stress ($\sigma_{\max}$) in the coated panels and the distortions of the panels with and without alumina coating due to such thermal fluctuations.

A total of 12 cases were analyzed. A plasma-sprayed-alumina-coated aluminum alloy 6061-T6 panel ($300\ mm \times 300\ mm \times 2\ mm$) subjected to normal solar loads on one side and albedo, IR flux on both sides. These cases were divided into 3 groups. Group 1 (five cases) deals with cases of $\alpha_n = 0.13$ and $\epsilon_h = 0.23$ (literature values selected [41]).

Group 2 (five cases) includes cases of $\alpha_{ne} = 0.31$ and $\epsilon_{he} = 0.81$ (averages of SMP-PSA-03 and SMP-PSA-05). Group 3 (two cases) involves $\alpha_{ne} = 0.39$ and $\epsilon_{he} = 1.29$ (these values were derived using energy absorption model based on surface properties of SMP-PSA-03; see chapter 7 for the modeling details).

5.1 Analysis Procedure

Two special analysis schemes were designed using a general-purpose finite element software, LUSAS (version 13.4), and a few user-written C programs to simulate the effects of a variety of thermal loading experienced simultaneously by a plasma-sprayed-alumina-coated panel in outer space environment. One scheme is used for thermal analysis and the other for subsequent structural analysis.

LUSAS, although a good and comprehensive FE package, cannot combine different environmental temperature loading for two or more surfaces as a function of time in the form of loading curves. Therefore, C programs were written to calculate separately and apply the loadings for different surfaces of the panel as a function of time in order to perform the analysis using LUSAS. Batch programs were used to manage the order of executing programs. The user-written C programs were: (a) CP1: to update initial nodal temperature and thermal loading at every timestep and to save the simulation results of every timestep, (b) CP2: to select certain nodal temperature from output for checking the trends, (c) CP3: to update initial nodal displacements and loadings at every timestep and to save the simulation results of every timestep, and (d) CP4: to select certain nodal displacements and stress from output for checking the distortions of the panel and the corresponding stress.

The program execution details are shown in Figure 5.1 and Figure 5.2. The accuracy of the developed analysis schemes for both temperature and stress analysis

were separately validated using a commercial software SINDA/G, which is a specialized software for space related thermal analysis [76], and/ or by manual calculations.

5.2 Geometric Details and Boundary Conditions

The substrate size is 300 mm × 300 mm × 2 mm. The coating thickness varies from 0.1 mm, 0.2 mm and to 0.3 mm.

The orbit plane was assumed parallel to the sunrays, as shown in Figure 5.3. This

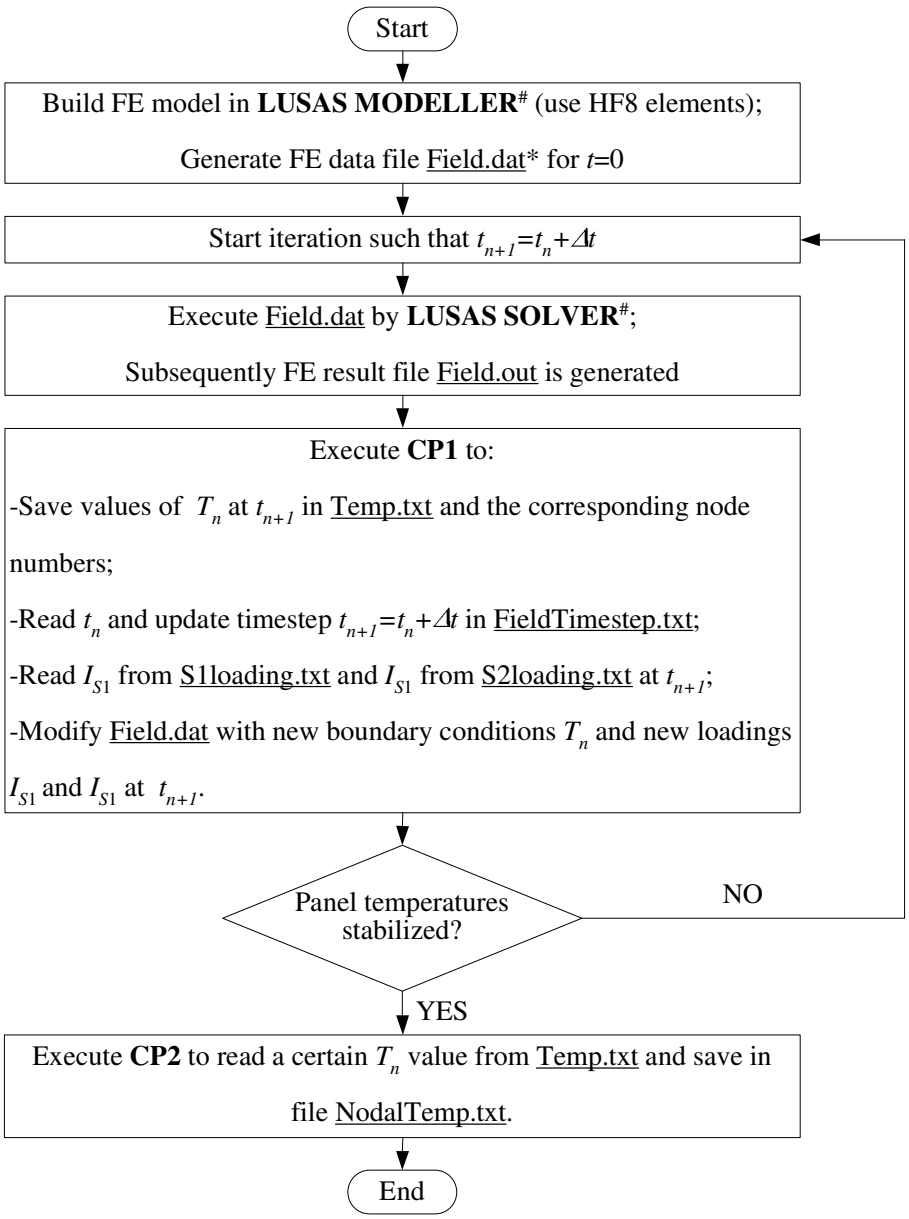

Figure 5.1: Procedure for field analysis (∗ Computer file; ♯ Executable program)

is the most severe case expected for a coated substrate in outer space. In order to generate maximum power, except for payload and downlink operations, solar panels are always kept normal to the sunrays. The loadings for the panel include solar flux (I_s, W/m^2),

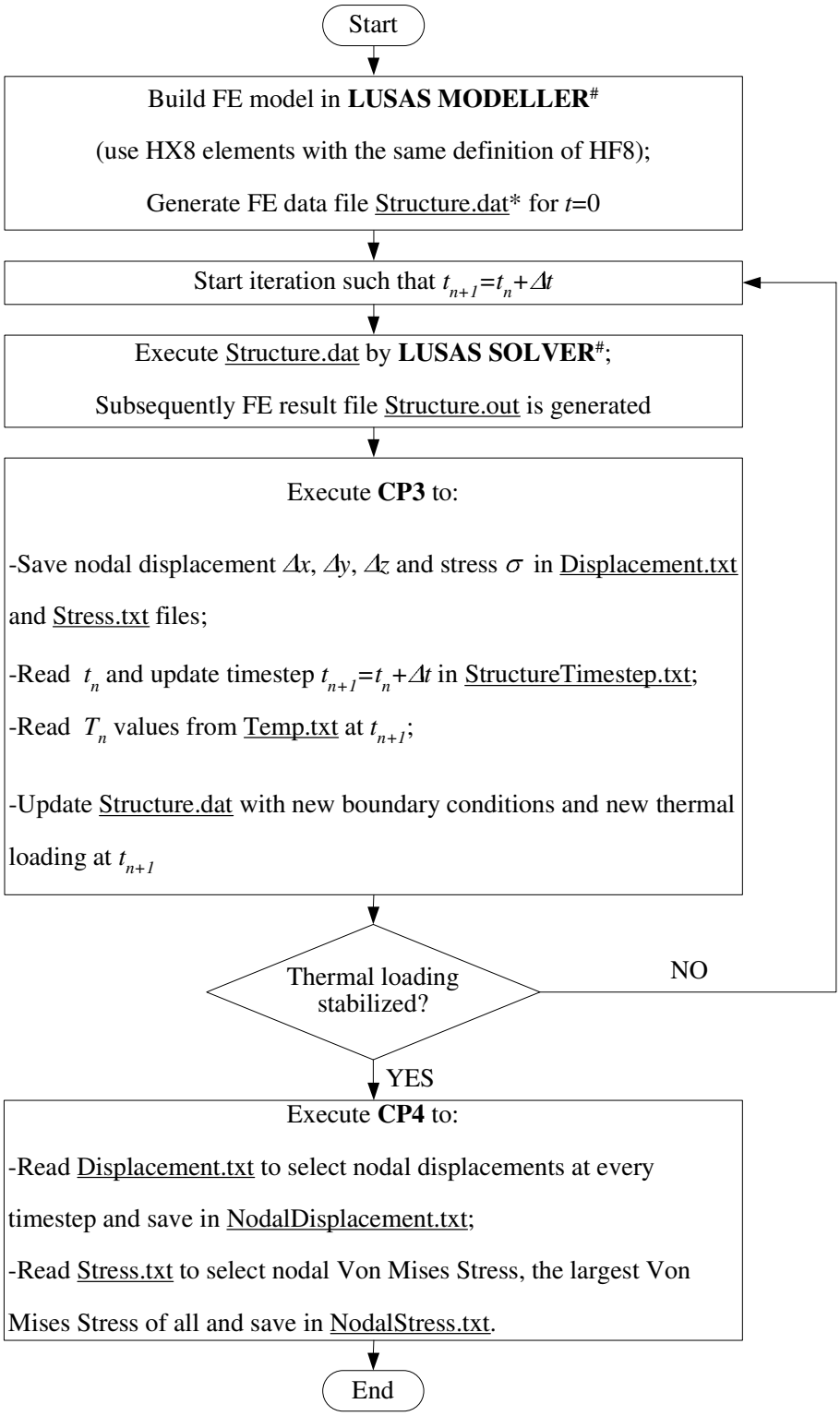

Figure 5.2: Procedure for structural analysis (∗Computer file; ♯ Executable program)

albedo from the earth (I_a, W/m^2) and IR radiation from the earth (I_I, W/m^2). The space is assumed to be a black body at 4 K [41, 109]. As mentioned in chapter 2, micro-satellite circles the earth in a LEO with an orbit period of approximately 90 to 100 min. In this study, it is assumed that the orbit height is $h = 685$ km and the orbit is circular. The estimated orbit period, t_p, is 98 min. The assumptions were based on the studies by other researchers [109].

In Figure 5.3, time t_1 to t_{11} are calculated as follows: assuming that the plasma-sprayed-alumina-coated panel starts its orbit at t_1:

$$t_2 = t_p \times \frac{\arccos\left(\frac{R}{R+h}\right)}{360^\circ} = 7 \; min$$

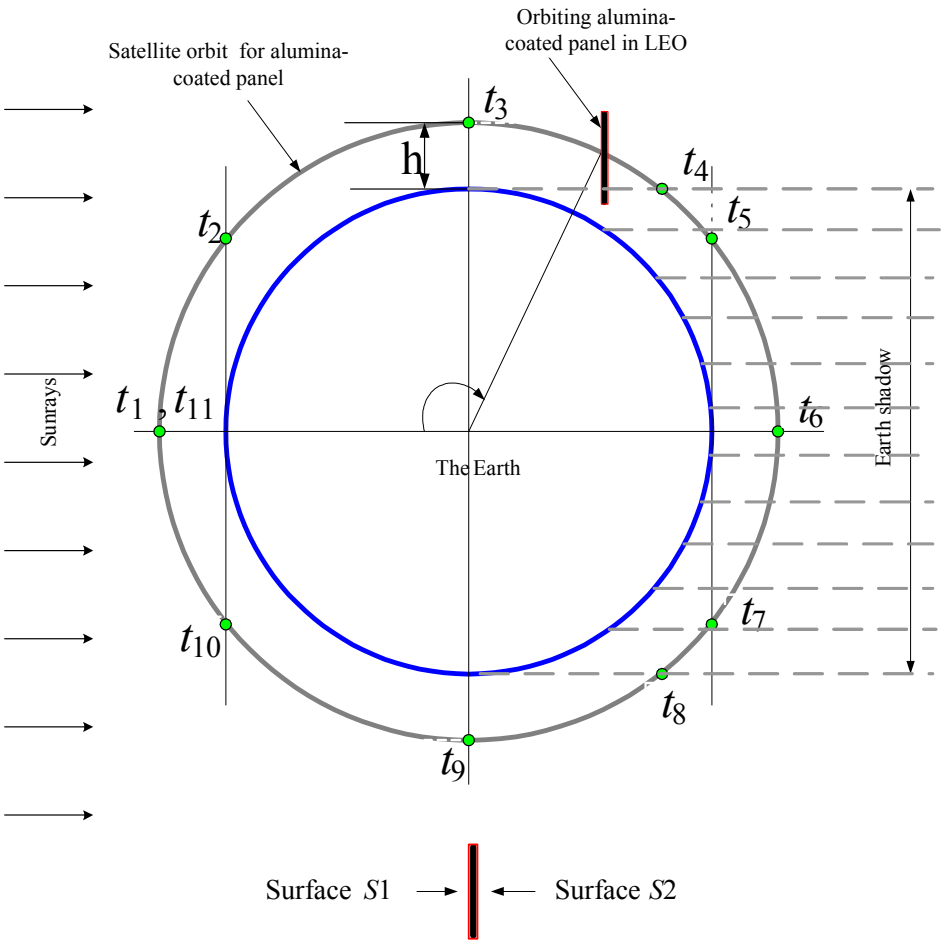

Symbols	t_1	t_2	t_3	t_4	t_5	t_6	t_7	t_8	t_9	t_{10}	t_{11}
Corresponding time (min)	0.0	7.0	24.5	31.5	42.0	49.0	56.0	66.5	73.5	91.0	98.0

Figure 5.3: Thermal loads as a function of orbit-positions for plasma-sprayed-alumina-coated panel in low earth orbit (Not to scale; $S1$/ $S2$ are the two surfaces of the panel; $S1$ is always sun facing)

In which, $R = 6375\ km$, radius of the earth; $h = 685\ km$, height of the orbit.

$$t_3 = t_p \times \frac{90^\circ}{360^\circ} = 24.5\ min$$

$$t_4 = t_p \times \frac{90^\circ + \arccos\left(\frac{R}{R+h}\right)}{360^\circ} = 31.5\ min$$

(dividing time-line between sunshine and earth shadow)

$$t_5 = t_p \times \frac{180^\circ - \arccos\left(\frac{R}{R+h}\right)}{360^\circ} = 42\ min$$

$$t_6 = t_p \times \frac{180^\circ}{360^\circ} = 49\ min$$

$$t_7 = t_p \times \frac{180^\circ + \arccos\left(\frac{R}{R+h}\right)}{360^\circ} = 56\ min$$

$$t_8 = t_p \times \frac{270^\circ - \arccos\left(\frac{R}{R+h}\right)}{360^\circ} = 66.5\ min$$

(dividing time-line between sunshine and earth shadow)

$$t_9 = t_p \times \frac{270^\circ}{360^\circ} = 73.5\ min$$

$$t_{10} = t_p - t_2 = 91\ min$$

$$t_{11} = 98\ min$$

According to the time calculation, I_s, I_a and I_I are calculated individually for $S1$ and $S2$ based on view factors for the panel. Then the total loadings for $S1$, I_{S1}, and the total loadings for $S2$, I_{S2}, are calculated and saved in separate files (S1loading.txt and S2loading.txt), as plotted in Figure 5.4. The calculations are briefly presented below (details in reference [58], pp 67-78):

$$I_{S1}(t) = F_{S1-s}(t) \times I_s + F_{S1-E}(t) \times (I_a + I_I)$$

Where F_{S1-s} is the view factor of surface $S1$ to the sun and F_{S1-E} is the view factor of surface $S1$ to the Earth.

$$I_{S2}(t) = F_{S2-E}(t) \times (I_a + I_I)$$

In which F_{S2-E} is the view factor of surface $S2$ to the Earth.

5.3 Finite Element Model

The FE models for temperature and stress analysis are both symmetrically meshed in a graded manner. The FE model for temperature analysis is simplified as a solid bar, as shown in Figure 5.5. It may be noted that even though 2D model was adequate for the temperature analysis, the stress analysis required a full 3D model to impose the appropriate boundary conditions for the solar panel substrate, such as the hinges between the panel and the satellite body.

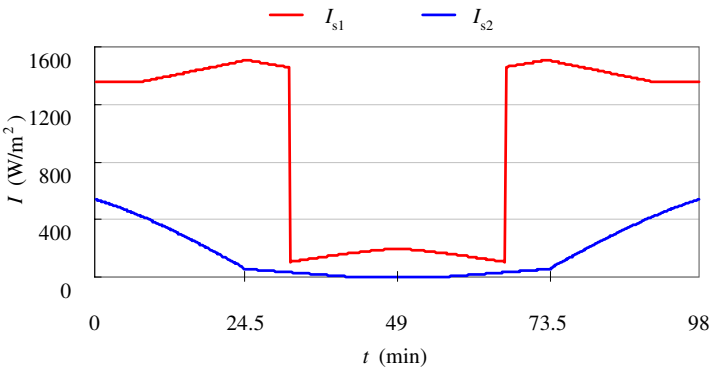

Figure 5.4: Thermal loadings on panel surfaces $S1$ and $S2$

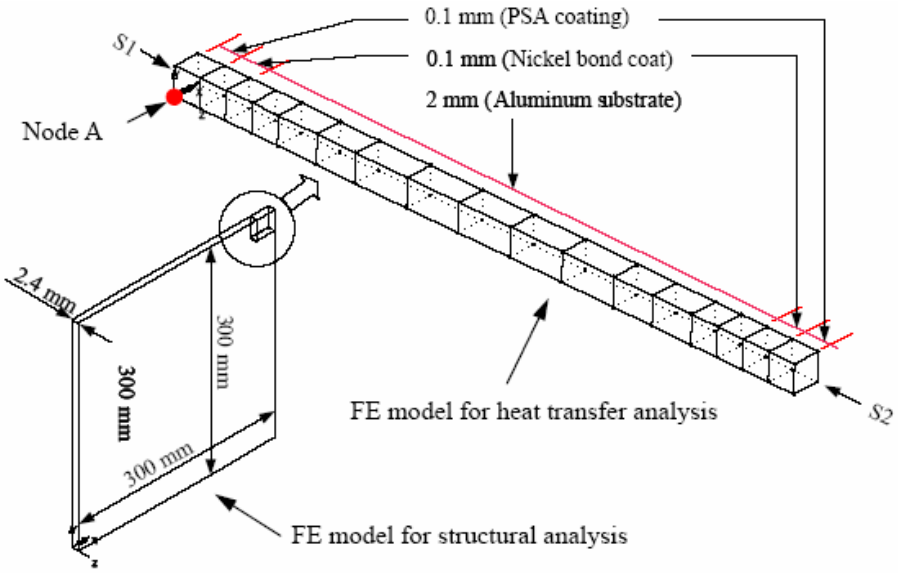

Figure 5.5: Finite element model used for heat transfer and stress analyses

5.4 Analysis

The thermal cycling process is analyzed as incremental transient heat transfer analysis. Two kinds of elements (HF8 and HX8, having the same geometry and mesh) are used to mesh the panel structure; HF8 (Hexahedral, field, 8 nodes) elements were used for heat transfer analysis and HX8 (Hexahedral, stress, 8 nodes) elements were used for stress and deformation analysis. The simulation procedures in the form of flow chart are shown in Figure 5.1 and Figure 5.2 respectively. The computation was controlled using user-written batch programs.

5.5 Validations

Validations are carried out to verify that LUSAS and the developed analysis schemes worked correctly. Validation of steady state thermal analysis is firstly performed to check the choice of correct LUSAS data cards by analytical calculations in section 5.5.1. Validation of transient thermal analysis is carried out using SINDA/G (details in section 5.5.2). and validation of stress analysis using analytical calculations in section 5.5.3.

5.5.1 Steady State Thermal Analysis

An example on a 300 $mm \times 300\ mm \times 1.5\ mm$ panel is used for the validation. The panel properties and other details are shown in Table 5.1. The I_{S1} is an average value of solar constant [7, 41, 58]. The I_{S2} is the sum of maximum albedo and IR from the earth [41,58]. The absorptance (α_n) and emittance (ϵ_h) are both set to 1.0 for simplicity in the validation. The other properties of the panel are defined as that of aluminum. The environment temperature for the panel is the deep outer space temperature, $T_0 = 4\ K$. The simulation results obtained using the developed LUSAS analysis scheme showed that the equilibrium temperature of the panel was 364.371 K ($\sim$ 364.4 K) for both surfaces

$S1$ and $S2$. In the middle (thickness-wise) it was 364.381 K ($\sim$ 364.4 K). The same case could be analytically solved. The equilibrium temperature is calculated as follows:

$$\alpha_n I_{S1} A_{S1} + \alpha_n I_{S2} A_{S2} = \sigma \epsilon_h \left(A_{S1} + A_{S2}\right) \left(T^4 - T_0^4\right) \tag{5.1}$$

Equation 5.1 was converted from equation 2.1. In equation 5.1, α_n=1, ϵ_h=1, $A_{in} = A_{out}$, thus

$$I_{S1} + I_{S2} = 2\sigma \left(T^4 - T_0^4\right) \tag{5.2}$$

So,

$$T = \sqrt[4]{\frac{I_{S1} + I_{S2}}{2\sigma} + T_0^4} \tag{5.3}$$

Substituting the values,

$$T = \sqrt[4]{\frac{1353 + 645.9}{2 \times 5.6697 \times 10^{-8}} + 4^4} = 364.376 \ K \tag{5.4}$$

Comparing the simulation result ($\sim$ 364.4 K) and analytical result ($\sim$ 364.4 K), it is found that the LUSAS scheme is correctly designed and the cards in the input file are correctly chosen. It should be noted that, the numbers accurate to 3 digits are used to check the numerical accuracy of LUSAS. However, for all practical purposes, the temperature values with one digit are adequate.

5.5.2 Transient Thermal Analysis

Validation of transient heat transfer analysis was carried out by comparing the results obtained using LUSAS and SINDA/G (a specially designed commercial software for studying thermal problem in space [76]). The same example as discussed in section 5.5.1 was

Table 5.1: Properties of a panel considered for validation

Panel Dimension (mm)	300 $mm \times$ 300 $mm \times$ 1.5 mm
Loading (W/m^2)	I_{S1} = 1353, I_{S2} =645.9
Surface Properties	α_n/ϵ_h = 1.0/ 1.0 for both $S1$ and $S2$ surface
Density (kg/m^3)	2700
Conductivity ($W/m \cdot K$)	121
Specific heat ($J/kg \cdot K$)	921

used. The same properties as shown in 5.1 were used. Only exception is that: (1) only loading I_{S1} was applied, (2) $\alpha_n/\ \epsilon_h$ for $S1$ was assumed 0.75/ 0.82, and (3) $\alpha_n/\ \epsilon_h$ for $S2$ was taken as 0.13/ 0.23. The comparison of the temperature history for one orbit period obtained using the two software is shown in Figure 5.6. The results are summarized in Table 5.2.

The results shown in Figure 5.6 and Table 5.2 confirm that both the loading calculations and the LUSAS simulation scheme are quite accurate. Small discrepancy observed might be due to numerical rounding-off of the numbers during analysis.

5.5.3 Stress Analysis

For validation of stress analysis, an example of bi-material bar was used. The FE model is shown in Figure 5.7. The support conditions, loadings and material properties are listed in Table 5.3.

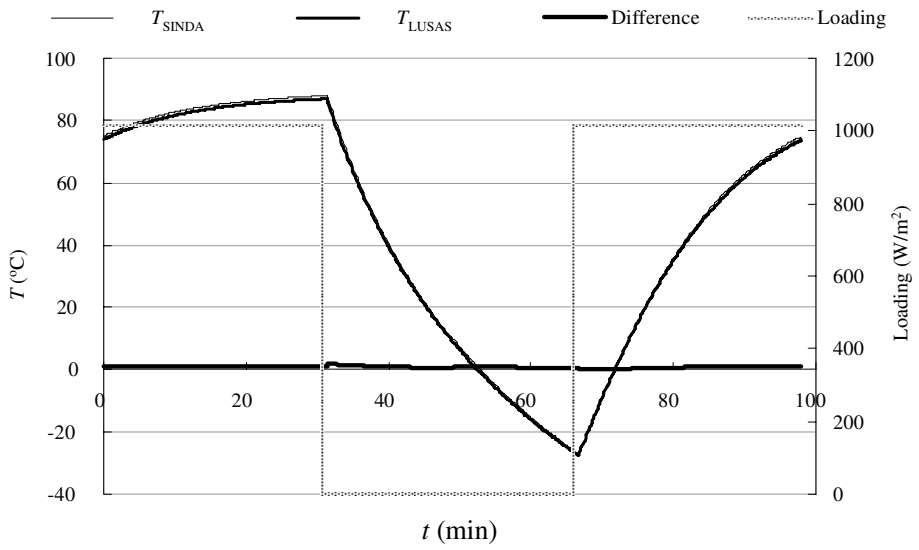

Figure 5.6: Comparison between temperatures obtained using LUSAS and SINDA/ G

Table 5.2: Minimum stabilized temperature ($T_{\min}$) and maximum stabilized temperature ($T_{\max}$) comparison (results of LUSAS and SINDA/G)

Temperature	LUSAS result	SINDA/G result	Difference (%)
$T_{\min},\ ^\circ C$	-27.101	-27.707	2.24
$T_{\max},\ ^\circ C$	87.986	87.046	1.07

Firstly case 1 was analyzed using LUSAS. Its stress contour is shown in Figure 5.8. This result can be validated by analytical calculation:

$$\sigma = E \times \delta = E \times \alpha \times \Delta T$$

Thus,

$$\sigma_{\text{Al}} = 73\text{E}9 \times 24\text{E} - 6 \times 100 = 175 \text{ MPa}$$

$$\sigma_{\text{Fe}} = 210\text{E}9 \times 12\text{E} - 6 \times 100 = 252 \text{ MPa}$$

The analytical results match very well with the peak stresses of 175 MPa and 252 MPa respectively for aluminum and steel obtained by FEA.

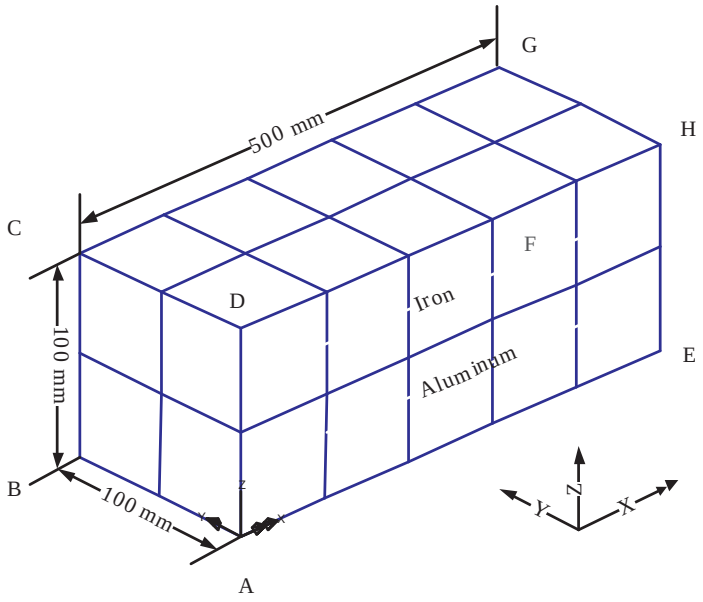

Figure 5.7: Finite element model of an example of bi-material bar

Table 5.3: Support conditions and properties used for stress analysis of bi-material bar example

Dimension $(mm \times mm \times mm)$	$500 \times 100 \times 100$
$E(Pa)$	$E_{Fe} = 210E9$, $E_{Al} = 73E9$
$\alpha_{\text{X}}, \alpha_{\text{Y}}, \alpha_{\text{Z}}, (m/m/\ ^{\circ}C)$	12E-6, 0, 0
Poisson's ratio	0
Support condition for case 1	Corner nodes A,B,C,D,E,F,G,H are fixed in X direction (i.e., $u = 0$)
Support condition for case 2	Corner nodes A,B,C,D,E,F,G,H are fixed in X direction ($u = 0$), except at E, F, G, H u=2.8029E-4m
Thermal loading	100 $^{\circ}C$ for all nodes

Secondly, for the model with support condition 2 (pre-deformation at certain points in X direction): Assume

$$\sigma_{\mathrm{Al}} = \sigma_{\mathrm{Fe}}$$

Thus,

$$E_{\mathrm{Al}}\delta'_{\mathrm{Al}} = E_{\mathrm{Fe}}\delta'_{\mathrm{Fe}} \ , \ \delta' = \delta_0 + \delta$$

Thus,

$$\frac{\delta_0 + \delta_{\mathrm{Al}}}{\delta_0 + \delta_{\mathrm{Fe}}} = \frac{E_{\mathrm{Fe}}}{E_{\mathrm{Al}}}$$

where,

$$\delta_0 = 2.8029\mathrm{E}-4 \ m$$

The corresponding stresses under 100 $^{\circ}C$ loading are calculated as follows:

$$\sigma_{\mathrm{Al}} = \frac{E_{\mathrm{Al}}\left(\delta - \delta_0\right)}{L} = \frac{73\mathrm{E}9 \times \left(24\mathrm{E}-6 \times 100 \times 0.5 - 2.8029\mathrm{E}-4\right)}{L} = 134 \ MPa$$

$$\sigma_{\mathrm{Fe}} = \frac{E_{\mathrm{Fe}}\left(\delta - \delta_0\right)}{L} = \frac{210\mathrm{E}9 \times \left(12\mathrm{E}-6 \times 100 \times 0.5 - 2.8029\mathrm{E}-4\right)}{L} = 134 \ MPa$$

The LUSAS stress contours showing peak stress of 134 MPa (presented in Figure 5.9) matches the analytical value very well. Thus a conclusion can be drawn that the LUSAS data cards and the simulation scheme are both correct.

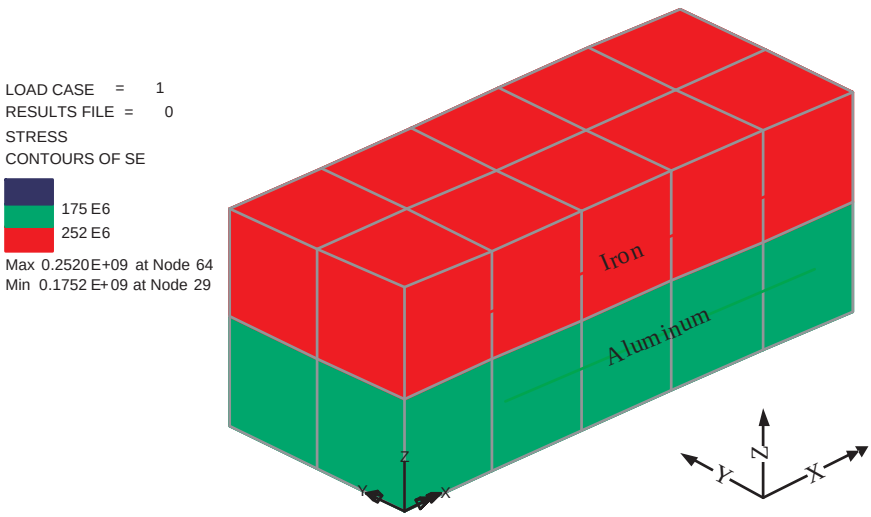

Figure 5.8: Results—validation of structural analysis (1)

5.6 Case Studies

As preliminary study, a total of 12 cases as described in Table 5.4 were analyzed. Simulations for Group 1 (5 cases) were carried out, using literature values of absorptance and emittance. Group 2 (5 cases) was simulated with average experimental values of absorptance and emittance. Group 3 was performed using predicted values after the energy absorption model was accomplished that provided effective values of absorptance and emittance. This was done only for the ease of reference and not for testing the developed models and the values of the derived radiation properties from the models. Thus, the content of this chapter are independent of the efficacy of the models which is examined in Chapter 6 later on.

The material properties used for the simulations are presented in Table 5.5. For

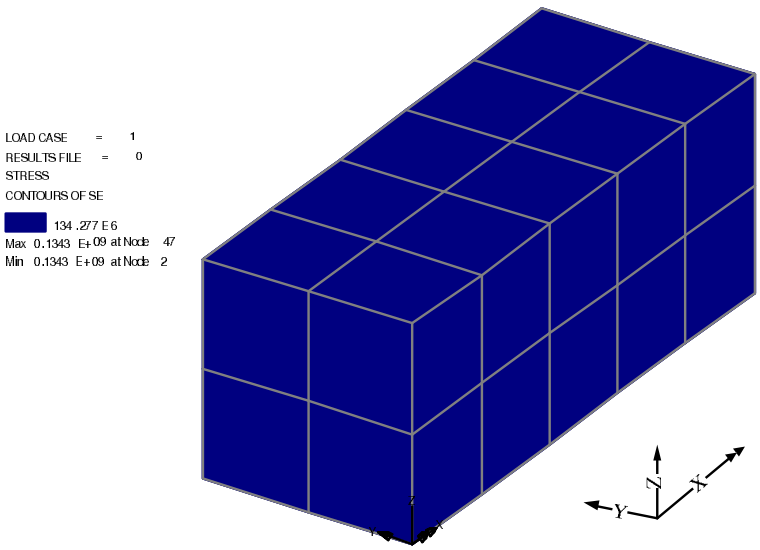

Figure 5.9: Results—validation of structural analysis (2)

Table 5.4: Simulated cases

Group No.	GP1	GP2	GP3	Substrate tk (mm)	Bondcoat tk (mm)	plasma sprayed alumina coating tk (mm)
Case No.	CA1	CA6	CA11	2	0.1	0.1
	CA2	CA7	-	2	0.1	0.2
	CA3	CA8	-	2	0.1	0.3
	CA4	CA9	-	3	0.1	0.1
	CA5	CA10	CA12	4	0.1	0.1

each of the 5 cases of Group 1, two separate stress analyses were performed using upper and lower bound values of Young's moduli that were obtained from literature.

The uncertainty in the input values for thermal loads comes from orbital conditions for a satellite. Satellite undergoes extreme hot and extreme cold conditions in an orbit. The change of loading conditions leads to the change in temperature for satellite components including panels. In the present analysis, thermal loadings for the extreme hot orbital conditions are considered. The substrate and coating thickness are selected in such a way that the mass of the spacecraft will not increase unnecessarily. When the considered plasma-sprayed-alumina-coated panel enters an eclipse portion of the orbit, it experiences the worst, coldest condition. Thus, viability of the plasma sprayed alumina coating is verified for both, the worst, hottest and the worst, coldest conditions. For any typical satellite application, a coating that can survive such extreme thermal loadings will not need further validation.

5.7 Results and Discussion

The simulation results $T_{\min}$, $T_{\max}$ and $\sigma_{\max}$, are presented in Table 5.6 (Group 1, note that $E = 61\ GPa$ and $E = 95\ GPa$ are the lower and upper bound values respectively for plasma sprayed alumina coating obtained experimentally), Table 5.7 (Group 2) and Table 5.8 (Group 3). The respective temperature curves are shown in Figure 5.10 (Group

Table 5.5: Material properties used for simulations

Property	Substrate (AA 6061-T6)	Bond Coat (Nickel)	plasma sprayed alumina coating
Density (kg/m^3)	2700	3800	3400
Specific heat ($J/kg \cdot K$)	921	500	755 [95]
Thermal conductivity ($W/m \cdot K$)	121	11.6	1 (the lowest value from literature [95])
CTE ($m/m/°C$)	24E-6	16E-6	8E-6
E (GPa)	73	200	61 and 95 (limiting values)
Poisson's ratio	0.33	0.33	0.23

1), Figure 5.11 (Group 2) and Figure 5.12 (Group 3). For all cases, the temperature and stress stabilized after three orbit periods. Thus, the results are for 98 min counted from 294 min to 392 min (i.e. the fourth orbit period). It should be noted that when satellite moves in and out of the earth's shadow, the loadings for surface $S1$ and surface $S2$ change rapidly, which cause the temperature of the plate change rapidly, as presented in Figure 5.4, at time $t_4 = 31.5\ min$ and $t_8 = 66.5\ min$.

It may be noted that the analytical solution cannot be directly obtained for these cases using Stefan-Boltzmann Law. The equilibrium temperature of the single aluminum plate with certain surface properties (absorptance and emittance for both surfaces) can be determined under a constant thermal loading. But for solar panels in LEO, the thermal loading for the sun-facing surface (i.e., surface $S1$ in Figure 5.3) and non-sun-facing surface (i.e., surface $S2$ in Figure 5.3) change significantly with time. The cyclic steady state temperature ($T_{\min}$, $T_{\max}$) for such loading conditions will be lower than the equilibrium temperature and very difficult to calculate using Stefan-Boltzmann Law.

Table 5.6: Simulation results for Group 1

Case No.	CA01	CA02	CA03	CA04	CA05
$T_{\min}\ (°C)$	-22.8	-19.3	-16.0	-7.6	3.9
$T_{\max}\ (°C)$	96.9	96.7	96.5	95.8	94.2
$T_{\max} - T_{\min}\ (°C)$	119.7	116.0	112.5	103.3	90.3
$\sigma_{\max}\ (MPa)$, $E = 61GPa$	75	71	71	79	81
$\sigma_{\max}(MPa)$, $E = 95GPa$	93	91	91	99	105

Table 5.7: Simulation results for Group 2

Case No.	CA06	CA07	CA08	CA09	CA10
$T_{\min}\ (°C)$	-52.1	-49.0	-46.1	-38.6	-28.2
$T_{\max}\ (°C)$	61.0	61.0	60.9	60.5	59.4
$T_{\max} - T_{\min}\ (°C)$	113.1	110.0	107.0	99.1	87.6

Table 5.8: Simulation results for Group 3

Case No.	CA11	CA12
$T_{\min}\ (°C)$	-52.4	-28.5
$T_{\max}\ (°C)$	61.0	59.4
$T_{\max} - T_{\min}\ (°C)$	113.4	87.9

Thus numerical simulation is necessary to estimate $T_{\min}$ and $T_{\max}$, followed by stress analysis.

Figure 5.13, which is a $\sigma_{\max}$ history at an FE node in one stabilized orbit period, reveals that the $\sigma_{\max}$ occurred when the temperature reached $T_{\max}$. Thus, for the rest of the cases, only the maximum temperature loading was used for structural analysis. That is, for every case, it is not necessary to simulate the whole orbit period. It should be mentioned that the $\sigma_{\max}$ for every case appears around the corner of the panel, as

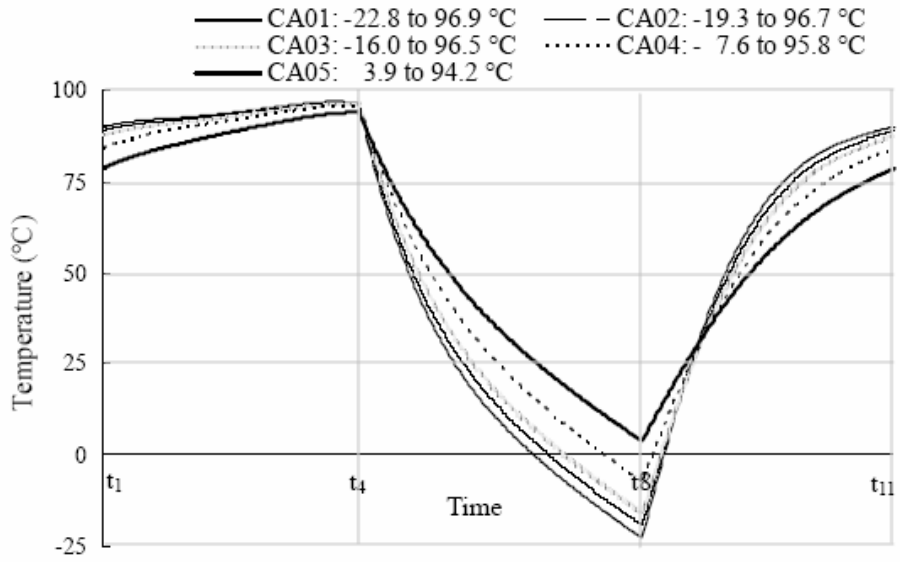

Figure 5.10: Temperature history of one orbit period for Group 1

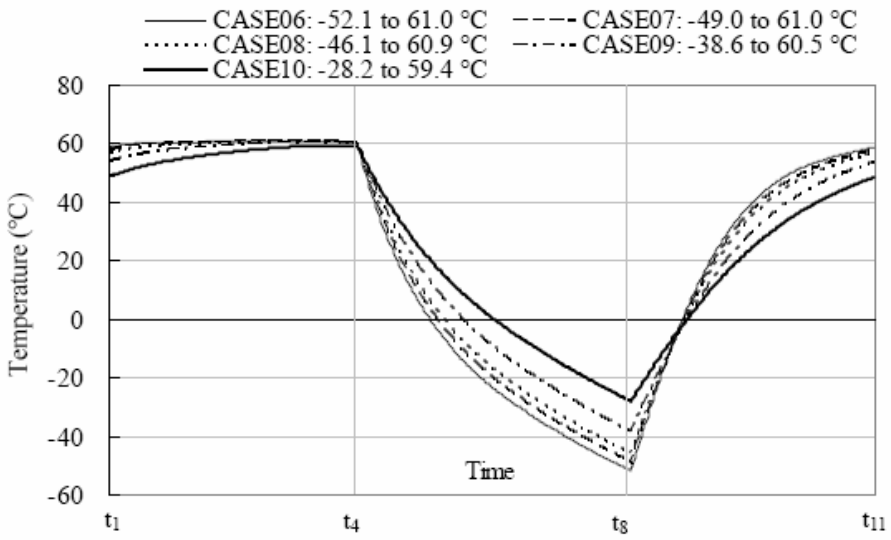

Figure 5.11: Temperature history of one orbit period for Group 2

shown in Figure 5.14. The stress is compressive because the aluminum substrate has a higher CTE than that of the alumina coating.

For cases CA01, CA02 and CA03, substrate thickness is 2 mm, while the alumina coating thickness is 0.1 mm, 0.2 mm and 0.3 mm respectively. From Figure 5.15, it can be seen that increasing alumina coating thickness can raise $T_{\min}$. Thus the overall temperature range for the panel is reduced. $\sigma_{\max}$ is reduced too, but slightly. It should be noted that, for CA01, $\sigma_{\max}$ occurred in the alumina coating, while for CA02 and CA03, $\sigma_{\max}$ occurred in the bond coating and the interfaces between bond coating and alumina

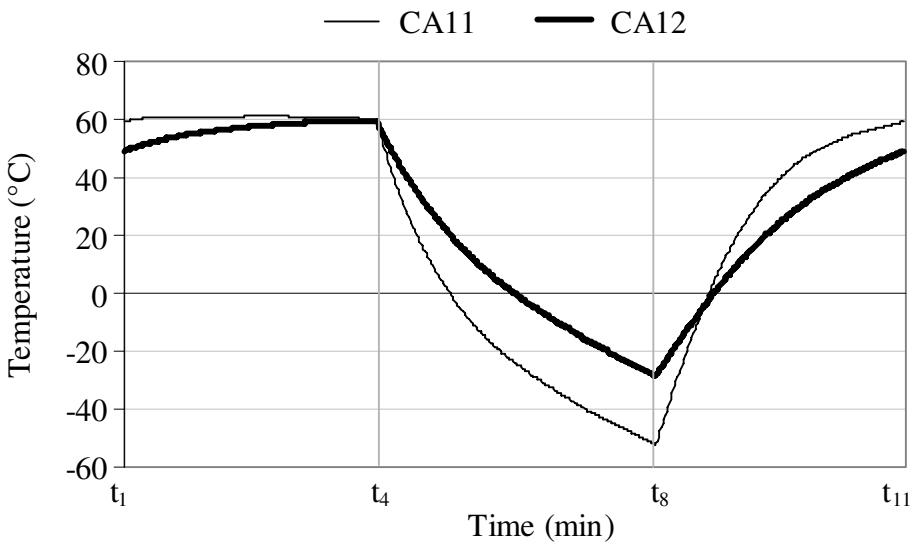

Figure 5.12: Temperature history of one orbit period for Group 3

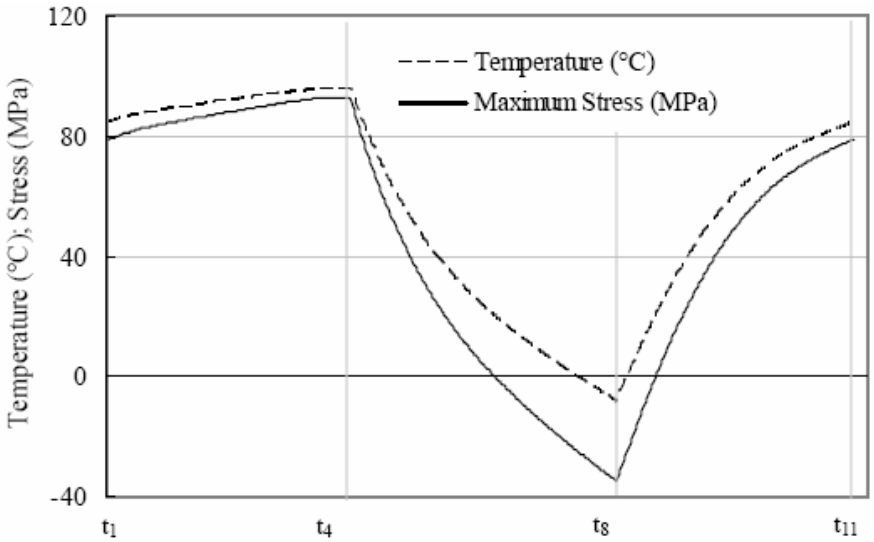

Figure 5.13: History for case CA01 at node A shown in Figure 5.5

coating. The reason is that, the thicker alumina coating is stronger than the thinner alumina coating layer.

From Figure 5.16 it can be seen that, with the increasing thickness of substrate, $T_{\min}$ increases, while $T_{\max}$ decreases slightly, thus the temperature range ($T_{\max} - T_{\min}$) is reduced. However the stress increases with an increase in thickness of the substrate.

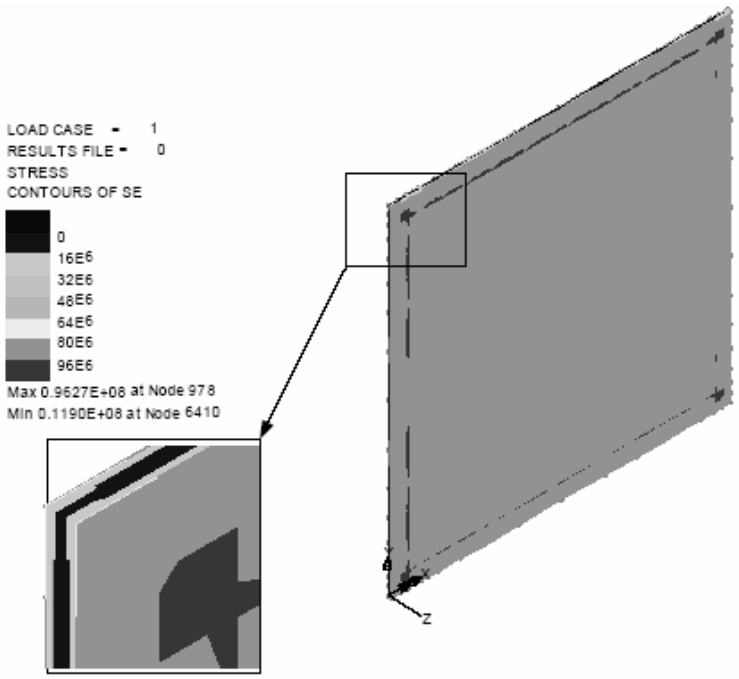

Figure 5.14: The locations of maximum stress ($\sigma_{\max}$) for case CA01

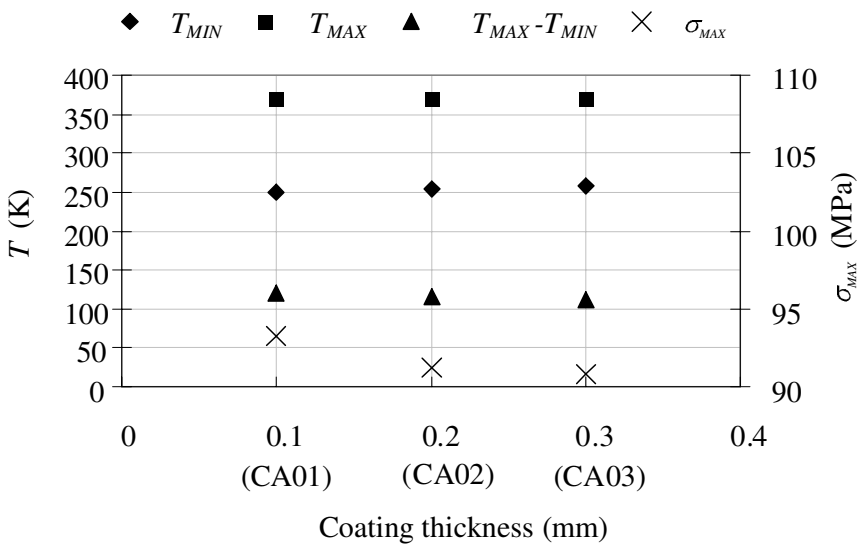

Figure 5.15: Temperature and stress vs.coating thickness

Thus, the substrate should be thin to keep the stress low, although it could raise the temperature range. For consideration of mass saving, this trend would be an advantage and could lead to an overall gain. For cases CA04 and CA05, $\sigma_{\max}$ occurred in the alumina coating.

The reason why both the coating thickness and the substrate thickness increase the $T_{\min}$ is that, the total thermal mass of the coated panel increases with an increase in coating/ substrate thickness.

For all cases, the stress occurred in the substrate was below 1 MPa, thus, $\sigma_{\max}$ did not reach fracture stress of alumina coating which is 138 MPa. Deflections caused by the thermal stress was not a problem. For example, the largest deflection in a 100 mm-long, 2 mm-thick aluminum square panel, with 0.1 mm-thick bond coating and 0.1 mm-thick alumina coating, were 0.086 mm (0.086%) in its longitudinal and transverse directions, and 0.007 mm (0.007%) in its thickness direction.

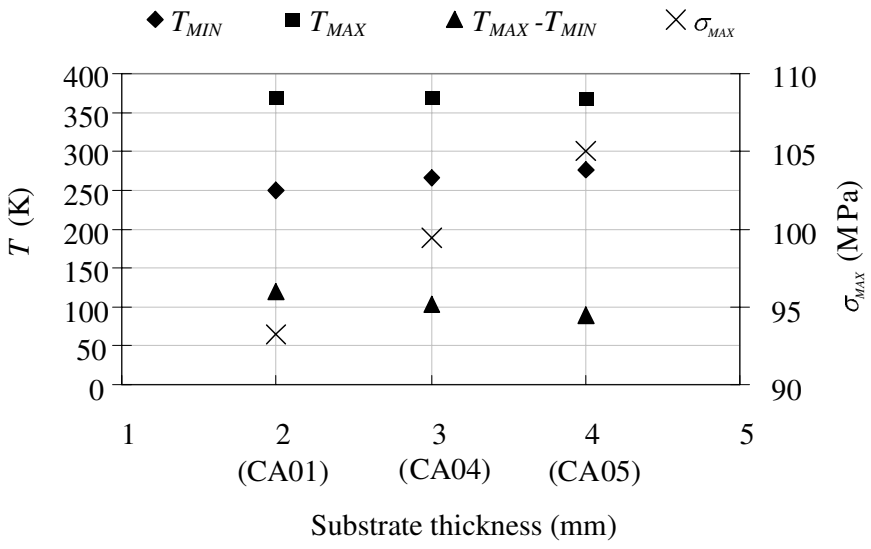

Figure 5.16: Temperature and stress vs. substrate thickness

5.8 Conclusions

FEM is applied to study the in-service thermo-mechanical behavior of the plasma-sprayed-alumina-coated solar panel substrates, including temperature variation, subsequent thermal stress distribution and the thickness effects of both substrate and alumina coating on these parameters. The simulation results reveal that: 1) $\frac{\alpha}{\epsilon}$ ratio for the alumina coating is suitable as TCM, 2) thermal stress within the plasma-sprayed-alumina-coated aluminum substrate under LEO thermal loadings is low and harmless for the panel, 3) the deflections are negligible, and 4) besides α and ϵ , both thickness of substrate and thickness of the alumina coating affect the stabilized temperature of the plasma-sprayed-alumina-coated panel.

Chapter 6

MODELING FOR RADIATION PROPERTIES OF A SURFACE

As mentioned in chapter 2, roughness plays a very important role in deciding the effective absorptance, α_{ne}, and effective emittance, ϵ_{he}, of a surface. Roughness parameters such as root-mean-square roughness cannot properly evaluate the surface roughness effects on radiation properties of opaque surfaces, i.e., α_{ne} and ϵ_{he}. Some models have been developed to predict the effects, such as Davies' model, Tang and Buckius's statistical geometric optics model [85], etc.. However they are valid only in very specific situations. A micro-level energy absorption geometrical model was developed and applied to investigate the roughness effects with the help of 2D surface profile of a plasma-sprayed-alumina-coated substrate scanned at micron level. This micro-level model predicts effective normal solar absorptance (α_{nel}) and effective hemispherical infrared emittance (ϵ_{hel}) of a small localized area of a rough surface. The micro-level model was validated using a few typical contrasts between examples of rough and smooth local area of a surface. Note that the ray interference with each other is ignored for the model.

The micro-level model predicts the local effective normal solar absorptance, α_{nel}, and the local effective hemispherical IR emittance, ϵ_{hel}, for an LV or an SLV of a rough surface. However, a rough surface consists of many LVs and/ or SLVs in reality. Thus the effective normal solar absorptance (α_{ne}) and the effective hemispherical IR emittance

(ϵ_{he}) are needed to simulate radiation heat transfer for a rough surface. The macro-level model was therefore developed, using which α_{ne} and ϵ_{he} can be predicted based on the baseline values of α_n and ϵ_h. The macro-level model was validated for a surface consisting of 3 LVs and 1 SLV and it was also applied to surfaces of plasma sprayed alumina coating.

An equation for absorptance based on its definition is

$$\alpha = \frac{\text{Total absorbed radiant flux}}{\text{Total incident flux}} \tag{6.1}$$

An equation for emittance based on its definition is

$$\epsilon = \frac{\text{Total power radiated by a body}}{\text{Total power radiated by a blackbody at the same temperature}} \tag{6.2}$$

The micro-level model, which uses Equations 6.1 and 6.2 as basic formulae, was developed through surface profile definition, α_{nel} equation solution, ϵ_{hel} equation solution followed by numerical validation.

6.1 Development of the Micro-Level Model

The micro-level model was developed for an area based on the scanned surface profile of a plasma sprayed alumina coating. Firstly, various necessary parameters were defined for a surface profile. Solutions for the parameters were then introduced. The α_{nel} equation and ϵ_{hel} equation were finally developed based on the parameters and their solutions.

6.1.1 Surface Profile and Parameter Definition

As mentioned in section 4.3 (page 40), the alumina coating surface was scanned with a 0.5 μm-interval in X direction and a 1 μm-interval in Y direction. Thus a scanned surface is formed by combining many 1 μm-wide strips, bound by (X, Z) coordinates. The strips are connected one by one in sequence. As a result, the 3D scanned surface is simplified to a 2D line element whose thickness is 1 μm. The rays hitting on the 2D

line element can be traced using geometrical optics method. Finally α_{nel} and ϵ_{hel} can be calculated using Equations 6.1 and 6.2 respectively.

The detailed process of obtaining the 2D strips is:

(1): Plot the 3D scanned surface profile as a pseudo-color image using the software MountainMap, as shown in Figure 6.1(a);

(2): Level the surface profile by running the command "Leveling" in the menu "Operators" of MountainMap, to correct the non-accurate sample mounting at an inclined plane (the leveled surface shown in Figure 6.1(b));

(3): Select the leveled surface profile, activate the command "Save the surface" from the menu "File", and save it as a *.txt surface profile which gives coordinates (X, Y, Z) of the captured points.

The command "Profile extraction" from the menu "Operators" provides the profile between any two points on the surface. For instance, the in Figure 6.1(c) was extracted for the line segment AB on the surface shown in Figure 6.1(b). Figure 6.1(d) is the first 100 μm length of line segment AB. Figure 6.1(e) is the first 10 μm length of line segment AB and the captured points were marked as red points. In Figure 6.1, "Pt" means the height between the highest point and the lowest point on the profile.

6.1.1.1 Coordinate System

The coordinate system used by the scanning system is Cartesian's and the surface is always marked by $+Z$ direction, as shown in Figure 6.2. This coordinate system was also used for calculating the variables during model development.

6.1.1.2 Local Valley and Semi Local Valley

As seen from the surface profile in Figure 6.2, there are numerous peaks and valleys marking the surface. A few terminologies are adopted for developing the model in the following sections. As shown in Figure 6.3, for a scanned surface profile, local valley

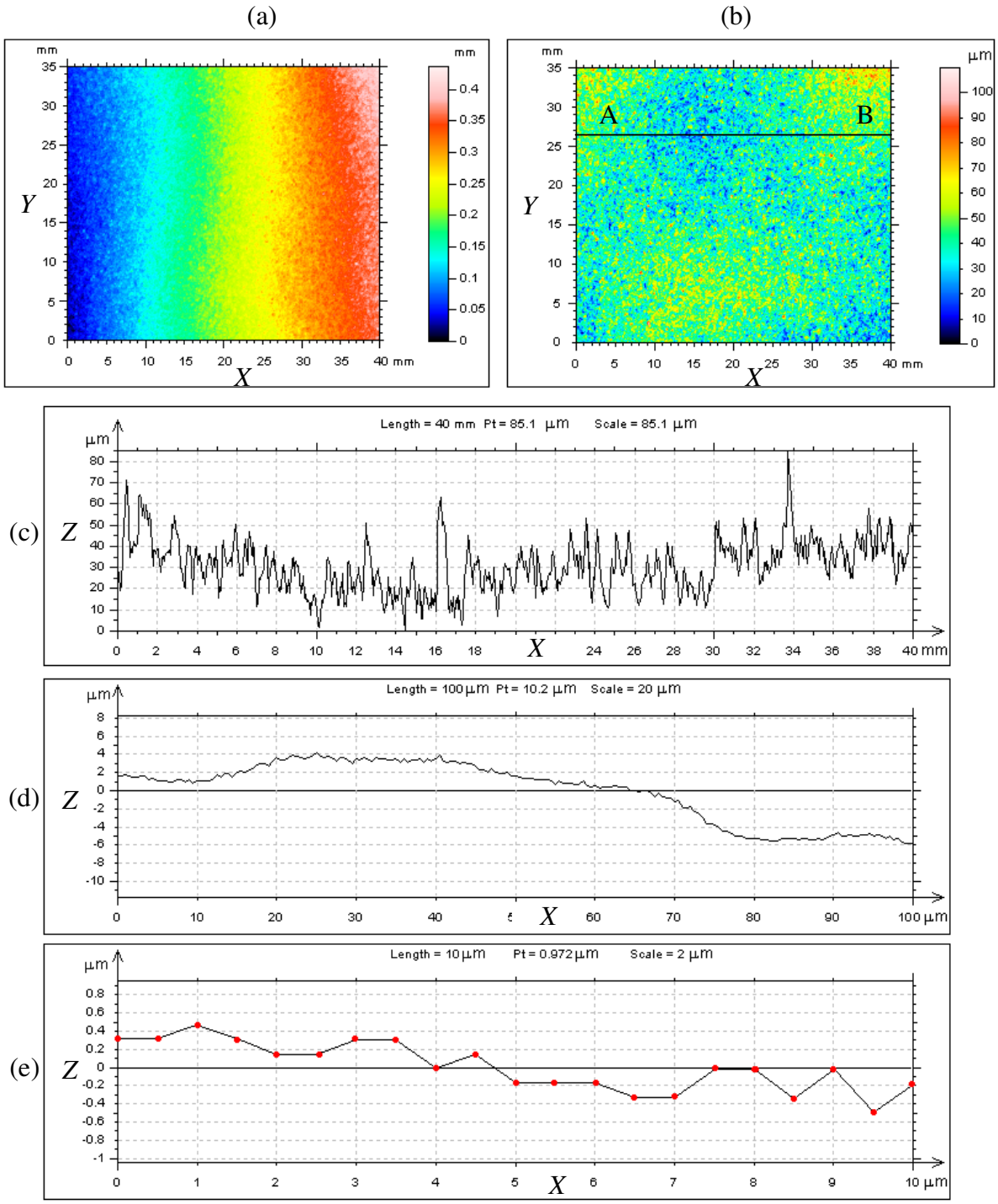

Figure 6.1: Pictorial explaining the scanned surface profile extraction process

(LV) is a region of a profile between two successive "high points" (local maxima) in the profile. Other individual segments are defined as semi local valleys (SLVs). With these two definitions, the energy absorbed by individual LV or SLV can be determined. For a large area consisting of many LVs and/ or SLVs, energy absorbed can be integrated over all the individual areas (this will be discussed in detail in chapter 7, macro-level modeling). An LV is described by its length of left hand side (LHS) segment, length of right hand side (RHS) segment, angle of LHS and angle of RHS, as shown in Figure 6.4. An SLV is expressed by its length and angle, as shown in Figure 6.5. Note that, for convenience, two cases of an SLV, case (a) and case (b) in this figure, are defined. The details of the above parameters are discussed below.

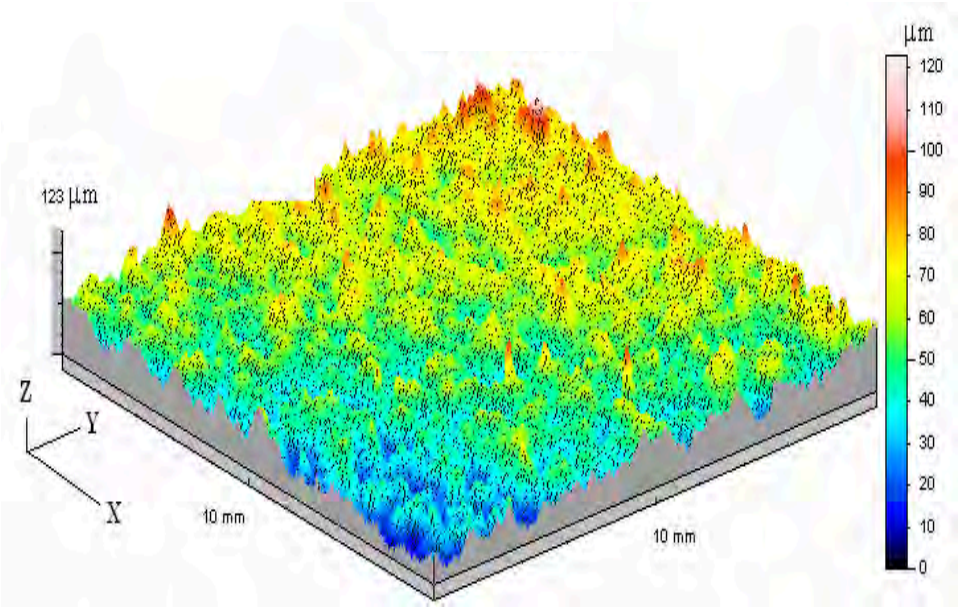

Figure 6.2: Surface orientation in the Cartesian coordinate system

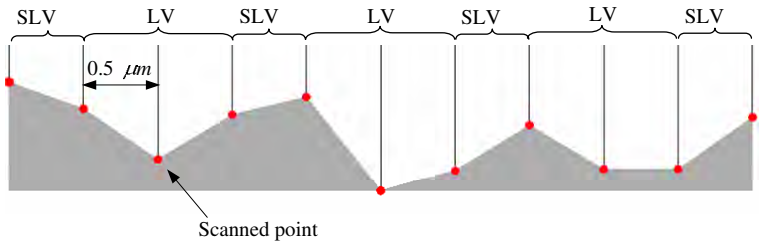

Figure 6.3: Definitions for local valley and semi local valley

6.1.1.3 Incidence Identification (i and $i^{'}$)

Incidence identification parameter was used as subscript to mark the number of times a beam of rays hits a surface. The superscript sign ($'$) was used to distinguish between the incidence identification number for the LHS and the RHS of an LV, for easy equation building. That is, for the incident rays that firstly reach the LHS of an LV, the incidence identification number is marked as i. For those incident rays reaching the RHS of an LV, the incidence identification number is marked as $i^{'}$. For an LV, the parameter i and $i^{'}$ both depend on the orientation of the LV, the angle of the LV and the side length of the LV. Moreover, i and $i^{'}$ have their own maximal values, $i_{\max}$ and $i^{'}_{\max}$. Determination of $i_{\max}$ and $i^{'}_{\max}$ will be discussed in section 6.1.1.7.

6.1.1.4 Flux Intensity of Incident Radiation (I_j and $I^{'}_k$)

For the flux intensity of incident rays that first hit the LHS of an LV is marked as I_j, j=0,1,..., i_{max}. For the incident rays that first hit the RHS of an LV, its flux intensity is marked as $I^{'}_k$, k=0,1,..., $i^{'}_{max}$. As shown in Figure 6.6, I_0, I_1, I_2 and I_3 are the flux

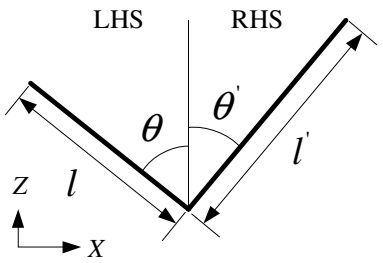

Figure 6.4: Description of a local valley

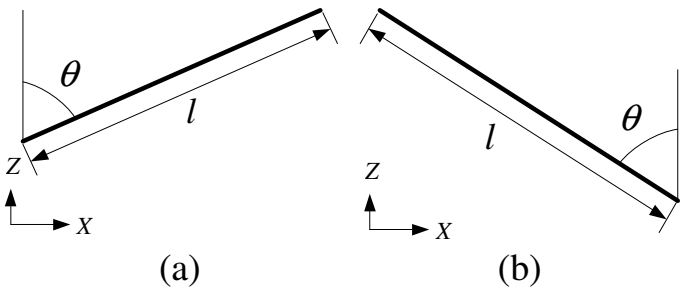

Figure 6.5: Description of a semi local valley

intensities for the rays hitting the LHS of the LV first. $I_0^{'}$, $I_1^{'}$, $I_2^{'}$, $I_3^{'}$ and $I_4^{'}$ are the flux intensity for the rays firstly hitting the RHS of the LV. The flux intensity reduces each time after reflection by the surface due to the absorption of some of the energy by the surface. Thus for Figure 6.6, relationship as below can be written:

$$I_0 > I_1 > I_2 > I_3 \quad and$$

$$I_0^{'} > I_1^{'} > I_2^{'} > I_3^{'} > I_4^{'}$$

Moreover, if I_0 is known, I_1, I_2 and I_3 can be calculated. Similarly, if $I_0^{'}$ is known, $I_1^{'}$, $I_2^{'}$, $I_{3'}$ and $I_4^{'}$ can be calculated. The calculation method will be discussed in section 6.1.1.5. Note that the generalized form, I_j and $I_k^{'}$, were used in the equations discussed in the following sections.

6.1.1.5 Incidence Angle (θ_j and $\theta_k^{'}$)

Incidence angle is the angle between the incident rays and the normal of the surface being radiated. For the incident rays that hit the LHS of an LV firstly, the incidence angle is

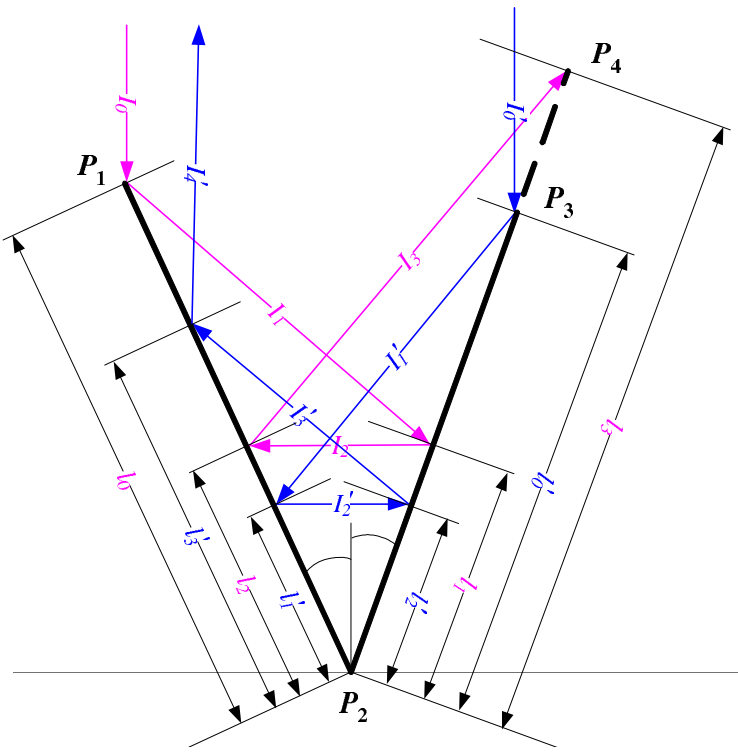

Figure 6.6: Illustration for flux intensity definition

marked as θ_j , $j = 0, 1, 2, \cdots, i_{\max} - 1$. For the incident rays that hit the RHS of an LV firstly, the incidence angle is marked as θ'_k , $k = 0, 1, 2, \cdots, i'_{\max} - 1$. The incidence angle was marked for an example of an LV, as shown in Figure 6.7.

The relations between each pair of incidence angle, θ_j, can be calculated. Similarly, the relations between each pair of incidence angle, θ'_k, can be determined. The incidence angles are calculated as follows (see Figure 6.7):

$$\theta_0 = 90 - \theta \tag{6.3}$$

For $\triangle$MON, $\angle 1 = \theta$, $\angle 2 = 90 + \theta_1$, $\angle 3 = \theta + \theta'$. Since $\angle 1 + \angle 2 + \angle 3 = 180°$ (Triangle-sum theorem),

$$\theta + (90 + \theta_1) + (\theta + \theta') = 180° \tag{6.4}$$

Simplifying equation 6.4,

$$\theta_1 = 90 - 2\theta - \theta' \tag{6.5}$$

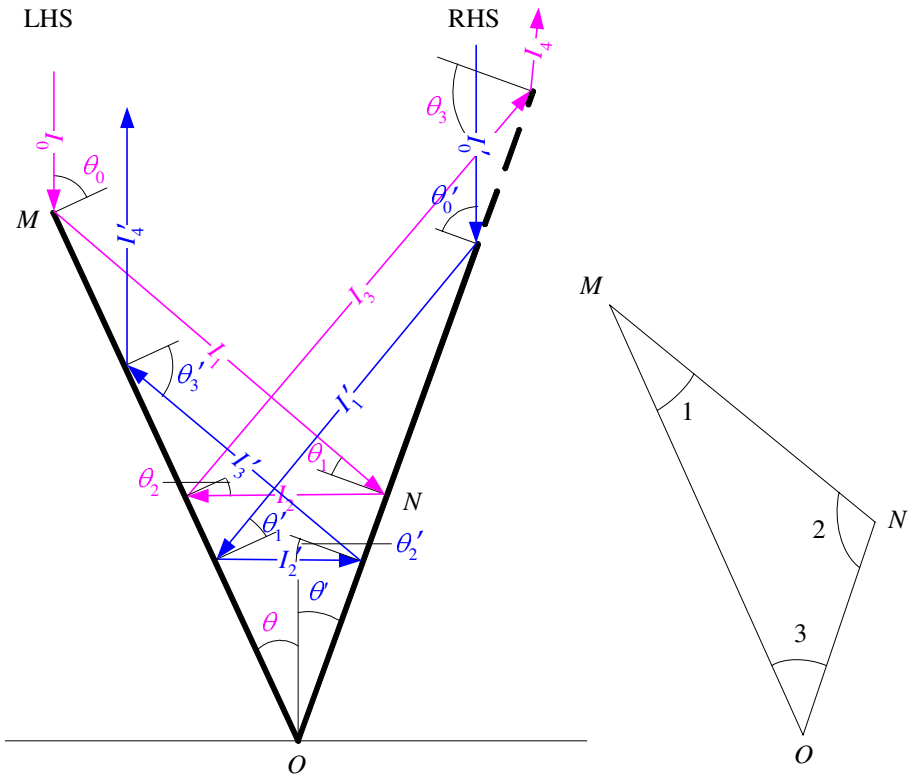

Figure 6.7: Illustration for incidence angle definition

Similarly, θ_2 for the second incident ray can be calculated as:

$$\theta_2 = 90 - 3\theta - 2\theta' \tag{6.6}$$

$$\theta_3 = 90 - 4\theta - 3\theta' \tag{6.7}$$

For the incidence rays reaching LHS of the LV first, the incidence angles were obtained using the same method as:

$$\theta_0' = 90 - \theta' \tag{6.8}$$

$$\theta_1' = 90 - 2\theta' - \theta \tag{6.9}$$

$$\theta_2' = 90 - 3\theta' - 2\theta \tag{6.10}$$

$$\theta_3' = 90 - 4\theta' - 3\theta \tag{6.11}$$

From the similarity observed among Equations 6.3, 6.5, 6.6 and 6.7, one generalized equation for θ_j can be obtained as:

$$\theta_j = \left|90 - (j+1)\theta - j\theta'\right|, j = 0,\ 1,\ 2,\ \cdots,\ i_{\max} - 1 \tag{6.12}$$

Similarly, the generalized equation for θ_j' can be obtained from Equations 6.8, 6.9, 6.10 and 6.11 as:

$$\theta_k' = \left|90 - (k+1)\theta' - k\theta\right|, k = 0,\ 1,\ 2,\ \cdots,\ i_{\max}' - 1 \tag{6.13}$$

It should be noted that, the situation $\theta = \theta' = 0°$ and $\theta = \theta' = 90°$ are special cases which need not be considered as no LV can be formed under any of these situations.

The incidence angle is used for the purpose of calculating the amount of energy being absorbed each time when rays hit the surface.

Thus, for the incident rays falling onto the LHS of an LV for the first time, its intensity after each hit (marked by $j+1$) is calculated as:

$$I_{j+1} = I_j \times (1 - \alpha_n),\ j = 0,\ 1,\ 2,\ \cdots,\ i_{\max} - 1 \tag{6.14}$$

For the incident rays falling on the RHS of an LV for the first time,

$$I_{k+1}' = I_k' \times (1 - \alpha_n),\ k = 0,\ 1,\ 2,\ \cdots,\ i_{\max}' - 1 \tag{6.15}$$

6.1.1.6 Maximum Incidence Length (l_j and $l_k^{'}$)

As shown in Figure 6.6, the subscripts for the maximum incidence length are defined according to the subscripts used for the flux intensity. For the rays first hitting on the LHS of an LV, the associated maximum incidence length is defined as l_j, $j = 0,\ 1,\ 2,\ \cdots,\ i_{\max} - 1$. For the rays first hitting on the RHS of an LV, the associated maximum incidence length is defined as $l_k^{'}$, $k = 0,\ 1,\ 2,\ \cdots,\ i_{\max}^{'} - 1$.

In Figure 6.6, l_0 is the left side length of the LV. The l_1, l_2 and l_3 can be calculated as follows: For $\triangle$MNO in Figure 6.7, applying SINE law,

$$\frac{\text{MO}}{\sin\angle 2} = \frac{\text{NO}}{\sin\angle 1} \tag{6.16}$$

where,

$$\text{MO} = \ l_0 \tag{6.17}$$

$$\angle\text{MNO} = \ 90 + \theta_1 \tag{6.18}$$

$$\text{NO} = \ l_1 \tag{6.19}$$

$$\angle\text{NMO} = \ \theta \tag{6.20}$$

Substituting Equations 6.17, 6.18, 6.19 and 6.20 into 6.16, we get:

$$\frac{l_0}{\sin(90 + \theta_1)} = \frac{l_1}{\sin\theta} \tag{6.21}$$

Substituting Equation 6.5 into Equation 6.21 and simplifying,

$$l_1 = \frac{l_0 \sin\theta}{\sin(180 - 2\theta - \theta^{'})} \tag{6.22}$$

Similarly,

$$l_2 = \frac{l_1 \sin(2\theta + \theta^{'})}{\sin(180 - 3\theta - 2\theta^{'})} \tag{6.23}$$

$$l_3 = \frac{l_2 \sin(3\theta + 2\theta^{'})}{\sin(180 - 4\theta - 3\theta^{'})} \tag{6.24}$$

For the incidence radiation onto the RHS of the LV, applying the same methods,

$$l_1^{'} = \frac{l_0^{'}\sin\theta^{'}}{\sin(180 - 2\theta^{'} - \theta)} \tag{6.25}$$

$$l_2^{'} = \frac{l_1^{'}\sin(2\theta^{'} + \theta)}{\sin(180 - 3\theta^{'} - 2\theta)} \tag{6.26}$$

$$l_3^{'} = \frac{l_2^{'}\sin(3\theta^{'} + 2\theta)}{\sin(180 - 4\theta^{'} - 3\theta)} \tag{6.27}$$

For Equations 6.22, 6.23 and 6.24, the generalized form is

$$l_{j+1} = \frac{l_j \sin\left((j+1)\theta + j\theta^{'}\right)}{\sin\left(180 - (j+2)\theta - (j+1)\theta^{'}\right)}\ ,\ j = 0,\ 1,\ 2,\ \cdots,\ i_{\max} \tag{6.28}$$

For Equations 6.25, 6.26 and 6.27, the generalized equation is

$$l_{k+1}^{'} = \frac{l_k^{'} \sin\left((k+1)\theta^{'} + k\theta\right)}{\sin\left(180 - (k+2)\theta^{'} - (k+1)\theta\right)}\ ,\ k = 0,\ 1,\ 2,\ \cdots,\ i_{\max}^{'} \tag{6.29}$$

6.1.1.7 Determination of $i_{\max}$ and $i_{\max}^{'}$

Figure 6.8 shows different LV geometries leading to different incident parameter i. In all cases shown in Figure 6.8, the direction of ray finally leaving the LV is parallel to one of the sides of the LV and:

$$2\theta + \theta^{'} = 180$$

$$\angle 1 = \angle 2 \tag{6.30}$$

In which, $\angle 1$ and $\angle 2$ can be calculated, as shown in Figure 6.9,

$$\angle 1 = 90 - 2(90 - \theta) = 2\theta - 90 \tag{6.31}$$

$$\angle 2 = 90 - \theta^{'} \tag{6.32}$$

Substituting Equations 6.31 and 6.32 into Equation 6.30 and simplifying,

$$2\theta + \theta^{'} - 180 = 0$$

In Figure 6.9, it was found that, when $\angle 1 \geq \angle 2$,

$$i_{\max} \leq 1 \tag{6.33}$$

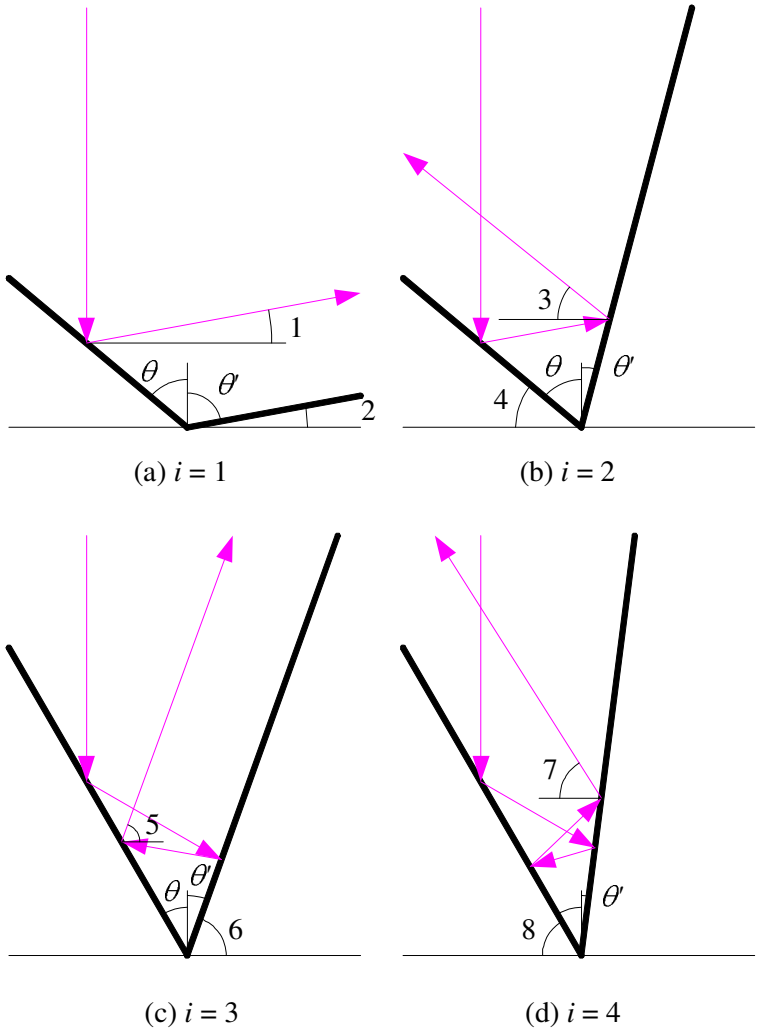

(a) $i = 1$ (b) $i = 2$

(c) $i = 3$ (d) $i = 4$

Figure 6.8: Four special cases of reflection

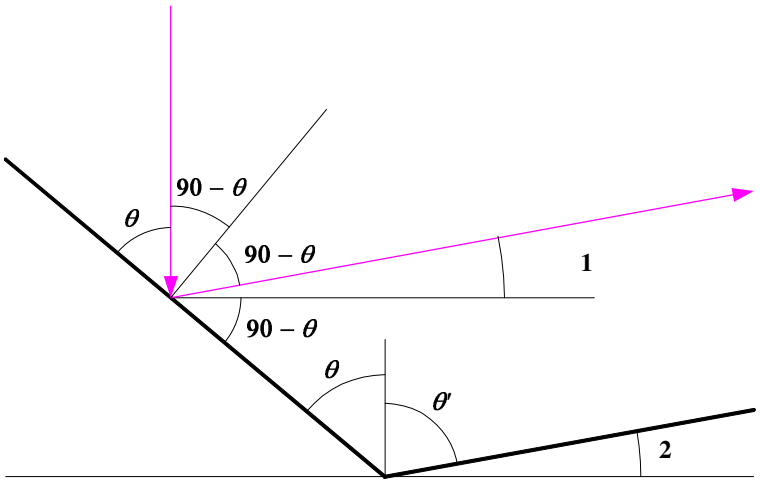

Figure 6.9: Angle calculation for Figure 6.8 (a)

Substituting Equations 6.31 and 6.32 into Equation 6.33:

$$2\theta - 90 \;\geq\; 90 - \theta^{'} \tag{6.34}$$

Simplifying Equation 6.34:

$$2\theta + \theta^{'} - 180 \;\geq\; 0 \tag{6.35}$$

Thus, without Equation 6.35 being true, Equation 6.33 cannot be valid. Similarly, for Figures 6.8(b), 6.8(c), and 6.8(d), the following 3 pairs of equation were obtained respectively:

$$i_{\max} \leq 2 \ , \ \text{when } 3\theta + 2\theta^{'} - 180 \geq 0$$

$$i_{\max} \leq 3 \ , \ \text{when } 4\theta + 3\theta^{'} - 180 \geq 0$$

$$i_{\max} \leq 4 \ , \ \text{when } 5\theta + 4\theta^{'} - 180 \geq 0$$

Thus, a generalized equation was obtained for $i_{\max}$,

$$i_{\max} \leq j \ , \ \text{when } (j+1)\theta + j\theta^{'} - 180 \geq 0 \ , \ j = \ 1, \ 2, \ 3, \ \cdots \tag{6.36}$$

Using the generalized Equation 6.36, $i_{\max}$ can be determined, as illustrated in Figure 6.10. In this figure, Equation 6.36 was plotted for $j \ = \ 1, \ 2, \ 3, \ 4, \ 5$. Using the same method, a generalized equation for $i^{'}_{\max}$ was obtained,

$$i^{'}_{\max} \leq k \ , \quad \text{when } (k+1)\theta^{'} + k\theta - 180 \ \geq \ 0 \ , \quad k \ = \ 1, \ 2, \ 3, \ \cdots \tag{6.37}$$

Determination for $i^{'}_{\max}$ is illustrated in Figure 6.11. Combining Equations 6.36 and 6.37, $i_{\max}$ and $i^{'}_{\max}$ were determined, as shown in Figure 6.12. The lines in this figure are values of critical angles and the lower bounds for the area above those lines on the right. For an SLV, $i = 1$, except when the incident ray is parallel to the SLV surface, which leads to $i_j = \ 0$. For the incident rays in the $-Z$ direction, the $i_{\max}$ depends only on the orientation of the LV and there is a certain relationship between $i_{\max}$ and the angle of the LV.

6.1.1.8 Width of Measured Profile

As mentioned earlier, the 3D surface can be simplified to a 1 μm-wide 2D strip.

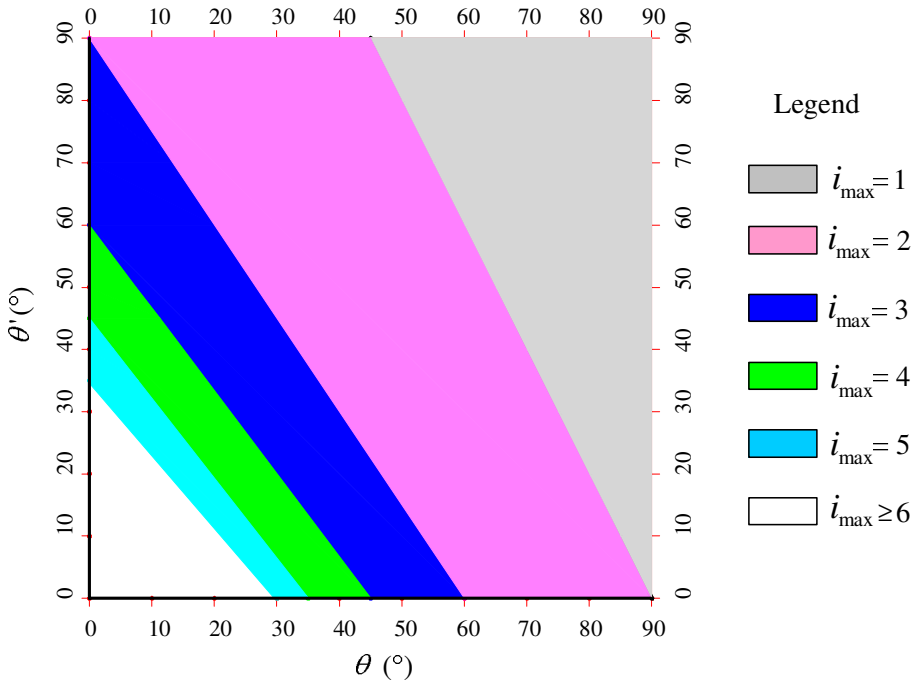

Figure 6.10: Illustration for determination of incidence identification number ($i_{\max}$)

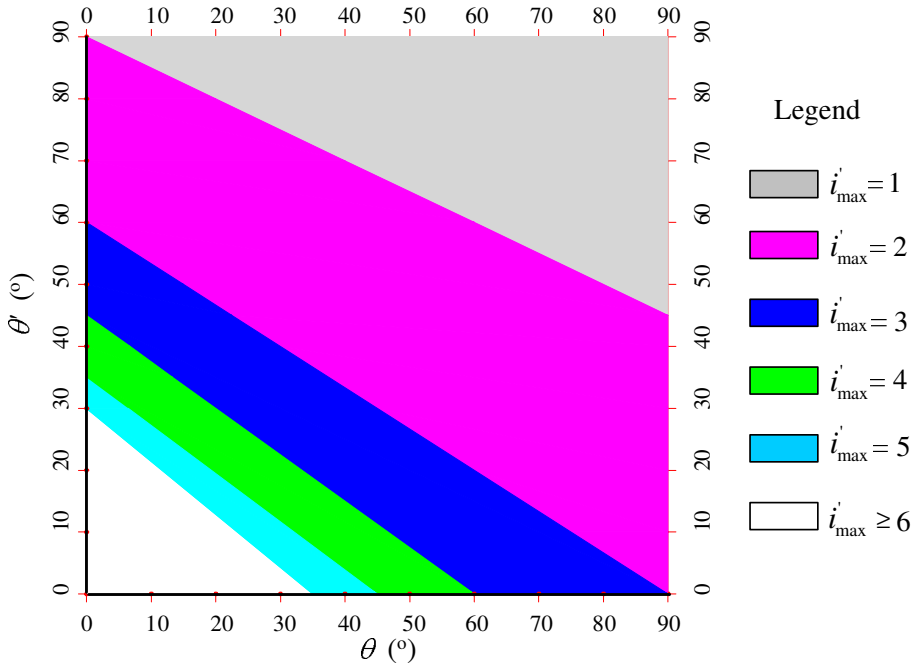

Figure 6.11: Illustration for determination of incidence identification number (i'_{max})

6.1.1.9 Absorbing Area (A and A')

Absorbing area is defined as the area over which the incident ray falls and its energy is absorbed. The absorbed energy can then be expressed as $E_j = \alpha_n I_j A_j$. A_j was determined for 4 different values of j and then a generalized equation was established. For the geometrical parameters shown in Figure 6.6, the following equations were obtained for the ray hitting the LHS of the LV first:

$$A_0 = l_0 \cos\theta_0$$

$$A_1 = \begin{cases} l_1 \cos\theta_1 \ , & l_1 \le l_0' \\ l_0' \cos\theta_1 \ , & l_1 > l_0' \end{cases}$$

$$A_2 = \begin{cases} l_2 \cos\theta_2 \ , & l_2 \le l_0 \\ l_0 \cos\theta_2 \ , & l_2 > l_0 \end{cases}$$

$$A_3 = \begin{cases} l_3 \cos\theta_3 \ , & l_3 \le l_0' \\ l_0' \cos\theta_3 \ , & l_3 > l_0' \end{cases}$$

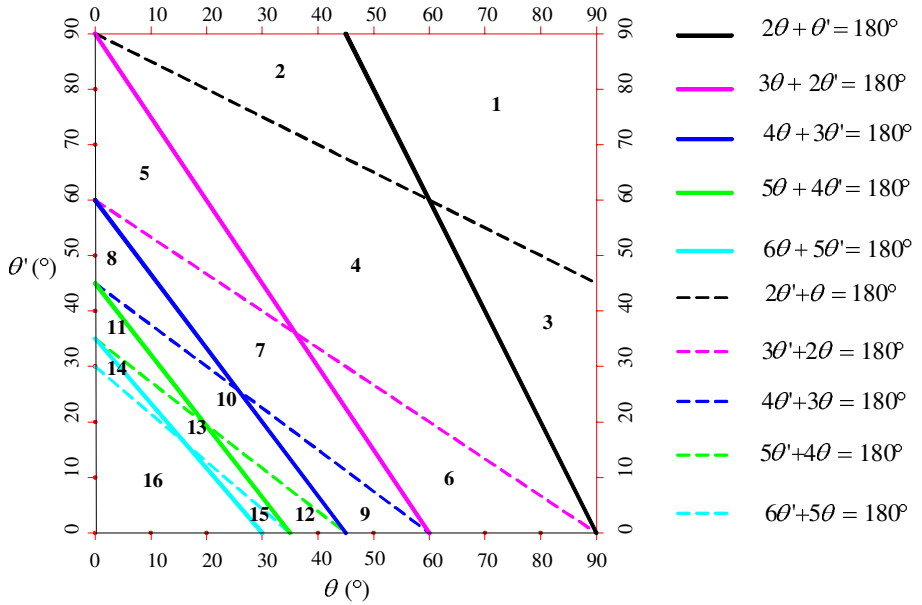

Area No.	1	2	3	4	5	6	7	8	9	10	11	12	13	14	15	16
i_{max} =	1	2	1	2	3	2	3	4	3	4	5	4	5	6	5	≥6
i'_{max} =	1	1	2	2	2	3	3	3	4	4	4	5	5	5	6	≥6

Figure 6.12: Illustration for determination of incidence identification number (i_{max} and i'_{max})

The generalized equation for the above four equations was established as,

$$A_j = \begin{cases} l_0 \cos\theta_0 \ , \ j = 0 \\ \begin{cases} l_j \cos\theta_j \ , \ l_j \leq l_0' \\ l_0' \cos\theta_j \ , \ l_j > l_0' \end{cases} \ , \ j \text{ is odd} \\ \begin{cases} l_j \cos\theta_j \ , \ l_j \leq l_0 \\ l_0 \cos\theta_j \ , \ l_j > l_0 \end{cases} \ , \ j \text{ is even} \end{cases} \tag{6.38}$$

Similarly, for the ray hitting the RHS of the LV, the generalized equation for the absorbing area is

$$A_k' = \begin{cases} l_0' \cos\theta_0' \ , \ k = 0 \\ \begin{cases} l_k' \cos\theta_k' \ , \ l_k' \leq l_0 \\ l_0 \cos\theta_k' \ , \ l_k' > l_0 \end{cases} \ , \ k \text{ is odd} \\ \begin{cases} l_k' \cos\theta_k \ , \ l_k' \leq l_0' \\ l_0' \cos\theta_k \ , \ l_k' > l_0' \end{cases} \ , \ k \text{ is even} \end{cases} \tag{6.39}$$

6.1.2 Local Effective Absorptance (α_{nel}) Model

From Equation 6.1, definition of α_{ne} for a local surface is:

$$\alpha_{nel} = \frac{\text{Total absorbed radiant flux for a local area}}{\text{Total incident flux for the local area}} \tag{6.40}$$

Thus, for an LV,

$$\alpha_{nel} = \frac{\alpha_n I_0 A_0 + \alpha_n I_1 A_1 + \cdots \alpha_n I_0' A_0' + \alpha_n I_1' A_1' + \cdots}{I_0 \times A_0 + I_0' \times A_0'} \tag{6.41}$$

The simple form of Equation 6.41 is

$$\alpha_{nel} = \frac{\alpha_n \times \sum_{j=0}^{i_{\max}} I_j \times A_j + \alpha_n \times \sum_{k=0}^{i'_{\max}} I_k' \times A_k'}{I_0 \times A_0 + I_0' \times A_0'} \tag{6.42}$$

Substituting parameters obtained using Equations 6.14, 6.15, 6.38 and 6.39 into 6.42, α_{nel} can be obtained. For an SLV, as $i_{\max} = 1$, Equation 6.42 simplifies to:

$$\alpha_{nel} = \alpha_n \tag{6.43}$$

6.1.3 Local Effective Emittance (ϵ_{hel}) Model

From Equation 6.2, definition of ϵ_{hel} for a local surface is:

$$\epsilon_{hel} = \frac{\text{Power radiated from a local area at certain temperature}}{\text{The power radiated by a blackbody at the same temperature for the same area}} \tag{6.44}$$

Thus, for an LV,

$$\epsilon_{hel} = \frac{\epsilon_h \left(l_0 + l_0^{'} - 2 l_0 F_{l_0 - l_0^{'}} \right)}{A_0 + A_0^{'}} \tag{6.45}$$

where,

$$\begin{aligned} F_{l-l'} \frac{\pi l'^2}{l} = & \\ & - \frac{\sin 2\phi}{4} \left[l l' \sin\phi + \left(\frac{\pi}{2} - \phi \right) \left(l^2 + l'^2 \right) + l'^2 \tan^{-1} \left(\frac{l - l' \cos\phi}{l' \sin\phi} \right) + l^2 \tan^{-1} \left(\frac{l' - l \cos\phi}{l \sin\phi} \right) \right] \\ & + \frac{\sin^2\phi}{4} \left\{ \left(\frac{2}{\sin^2\phi} - 1 \right) \ln \left[\frac{(1+l^2)(1+l'^2)}{1+Z} \right] + l'^2 \ln \left[\frac{l'^2 (1+Z)}{(1+l'^2) Z} \right] + l^2 \ln \left[\frac{l^2 (1+l^2)^{\cos 2\phi}}{Z (1+Z)^{\cos 2\phi}} \right] \right\} \\ & + l' \tan^{-1} \left(\frac{1}{l'} \right) + l \tan^{-1} \left(\frac{1}{l} \right) - \sqrt{Z} \tan^{-1} \left(\frac{1}{\sqrt{Z}} \right) \\ & + \frac{\sin\phi \sin 2\phi}{2} l \sqrt{1 + l^2 \sin^2\phi} \left[\tan^{-1} \left(\frac{l \cos\phi}{\sqrt{1 + l^2 \sin^2\phi}} \right) + \tan^{-1} \left(\frac{l' - l \cos\phi}{\sqrt{1 + l^2 \sin^2\phi}} \right) \right] \end{aligned} \tag{6.46}$$

in which,

$$Z = l^2 + l'^2 - 2 l l' \cos\phi \ , \ \phi = \theta + \theta'$$

Equation 6.46 is a view factor equation, which is a converted form of an equation given in reference [76]. For an SLV, Equation 6.45 simplifies to

$$\epsilon_{hel} = \frac{\epsilon_h l}{A} = \frac{\epsilon_h}{\sin\theta} \tag{6.47}$$

Thus, for a scanned surface there are many parameters to be taken care of while arriving at α_{nel} and ϵ_{hel}. A C-program based on Equations 6.42 and 6.45 was written to calculate α_{nel} and ϵ_{hel}.

6.2 Numerical Validation for Micro-Level Model

The numerical validation of the micro-level model is carried out for 3 typical cases, by means of comparing temperature history obtained by analytical calculations and numerical simulations. The 3 cases are listed in Table 6.1. The comparison between equilibrium temperature results is shown in Table 6.2. In Figure 6.13, objects (a) and (b) have the same thermal mass ($V \times \rho \times c_p$). However, object (a) represents the surface geometry as it

is, whereas object (b) has an equivalent flat surface. Radiation properties α_n and ϵ_h were used as baseline values for object (a). For object (b), α_{nel} and ϵ_{hel} values obtained using the micro-level model were used. All the cases were then analyzed numerically using a general-purpose finite element package, LUSAS. The results are shown in Table 6.2, column 4. Further analytical solutions were also obtained for these simple geometries. As shown in column 5 of Table 6.2, the results match exactly with the LUSAS results.

The transient temperature has to match with each other as well. This is discussed

Table 6.1: Three typical cases for numerical validation of micro-level model

Case ID	$\theta = \theta'$	$i = i'$	α_n	ϵ_h
CA-V1	15°	6	0.3	0.8
CA-V2	30°	3	0.3	0.8
CA-V3	45°	2	0.3	0.8

Table 6.2: Comparison between equilibrium temperatures for numerical validation of micro-level model

Case	α_{nel}	ϵ_{hel}	LUSAS temperature (K)	Analysis temperature (K)
CA-V1	0.8824	1.4796	348.3	348.3
CA-V2	0.6570	1.1388	345.5	345.5
CA-V3	0.5100	0.8799	345.9	345.9

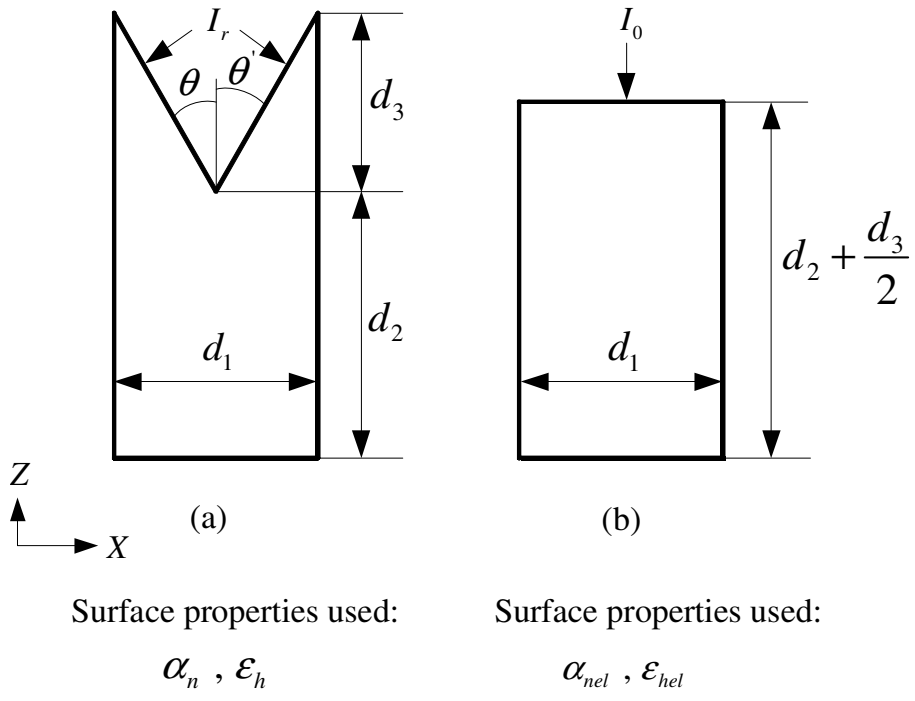

Figure 6.13: One case for numerical validation (width measured along Y axis, $w = 1$)

as below (see Figure 6.13): object (a) and object (b) have the same volume of $d_1 \times (d_2 + \frac{d_3}{2}) \times w$ and the same thermal mass ($V \times \rho \times c_p$). For the object (a) of Figure 6.13 , the instantaneous temperature is

$$T_{t+\Delta t} = T_t + \Delta t \frac{\alpha_n I_r (l + l^{'}) w - \sigma \epsilon_h (1 - F_{l-l^{'}})(l + l^{'}) w (T_t^4 - T_0^4)}{\rho c_p V} \tag{6.48}$$

where

$$I_r = I_0 \sin\theta \tag{6.49}$$

For the object (b) of Figure 6.13, the instantaneous temperature is

$$T_{t+\Delta t} = T_t + \Delta t \frac{\alpha_{nel} I_0 (l + l^{'}) w \sin\theta - \sigma \epsilon_{hel} (l + l^{'}) w \sin\theta (T_t^4 - T_0^4)}{\rho c_p V} \tag{6.50}$$

Thus, only if Equations 6.48 and 6.50 are equal, the instantaneous temperatures will match with each other for cases (a) and (b). Thus, by comparing Equations 6.48 and 6.50 and simplifying

$$\alpha_n I_r (l + l^{'}) w = \alpha_{nel} I_0 (l + l^{'}) w \sin\theta \tag{6.51}$$

$$\sigma \epsilon_h (1 - F_{l-l^{'}})(l + l^{'}) w (T_t^4 - T_0^4) = \sigma \epsilon_{hel} (l + l^{'}) w \sin\theta (T_t^4 - T_0^4) \tag{6.52}$$

Simplifying Equation 6.51:

$$\alpha_{nel} = \frac{\alpha_n I_r}{I_0} \tag{6.53}$$

Equation 6.53 exactly matches the original equation defining α, i.e., Equation 6.40. Simplify Equation 6.52 for

$$\epsilon_{hel} = \frac{\epsilon_h (1 - F_{l-l^{'}})}{\sin\theta} \tag{6.54}$$

Equation 6.54 is another form of Equation 6.45. This shows that the instantaneous temperatures for cases (a) and (b) will match, provided α_{nel}, ϵ_{hel}, α_n and ϵ_h values satisfy Equations 6.53 and 6.54. As shown in Table 6.3, the results for α_{nel} and ϵ_{hel} match well with the values obtained using Equations 6.53 and 6.54.

The entire process of numerical validation for case CA-V3 is discussed below.

For case CA-V3, $\theta = \theta' = 45°$ (refer Figure 6.14), assuming $I_0 = 1400\ W/m^2$,

$$I_r = I_0 \cos\theta + I_0 \cos\theta' = 1400 \times \cos 45 + 1400 \times \cos 45 = 1682.9\ W/m^2.$$

Using $I_r = 1682.9$, $\alpha_n = 0.3$ and $\epsilon_h = 0.8$ as input for the numerical simulation for the object (a) shown in Figure 6.14, the temperature history for object (a) was obtained; refer to Figure 6.15. For object (b) shown in Figure 6.14, $I_0 = 1400.0$, $\alpha_{nel} = 0.5100$ and $\epsilon_{hel} = 0.8799$ were used as input for the numerical simulation using LUSAS and the temperature history was obtained, which is also shown in Figure 6.15. A temperature history curve was also obtained for object (b) using the analytical method (i.e., using Equation 6.50). Comparing these 3 temperature histories, it was found that the micro-level model developed for α_{nel} and ϵ_{hel} is reliable and accurate.

Table 6.3: Local effective absorptance (α_{nel}) and local effective emittance (ϵ_{hel}) results for SMP♯2

Case	α_n	ϵ_h	Model		Equations 6.53 and 6.54	
			α_{nel}	ϵ_{hel}	α_{nel}	ϵ_{hel}
CA-V1	0.3	0.8	0.8824	1.4796	0.8824	1.4796
CA-V2	0.3	0.8	0.6570	1.1388	0.6570	1.1388
CA-V3	0.3	0.8	0.5100	0.8799	0.5100	0.8799

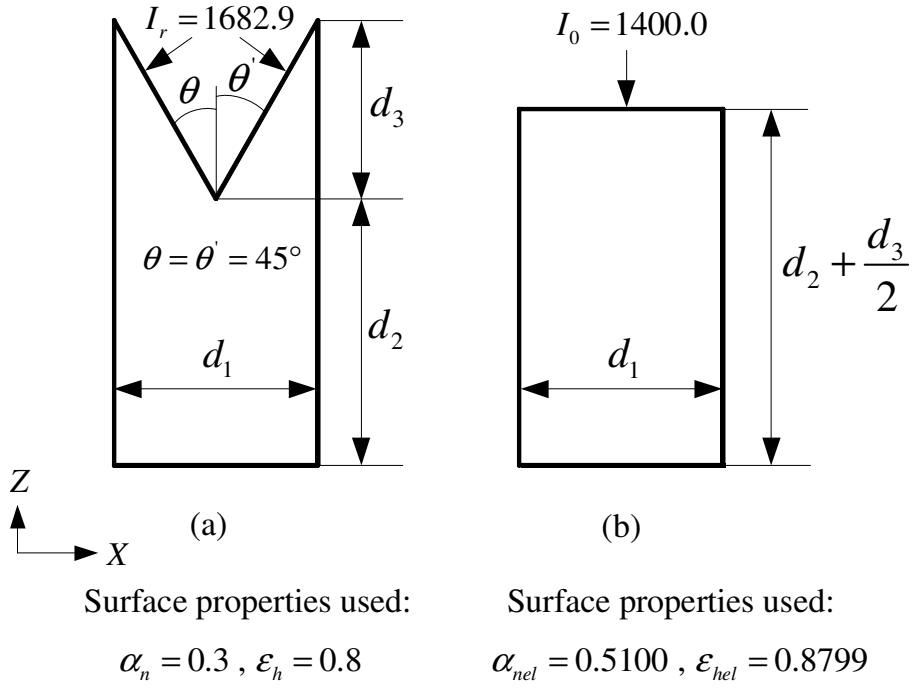

Figure 6.14: Numerical validation for case CA-V3

6.3 Conclusions for Micro-Level Model

The micro-level model for α_{nel} and ϵ_{hel} was successfully developed and validated using analytical and numerical methods. However, this model is limited only for a single geometrical feature such as an LV or an SLV. This model would serve as a basic building block for the development of a macro-level model for a large surface consisting of more than one LV and/ or SLV.

6.4 Development of the Macro-Level Model

As seen in the above section, the micro-level model predicts the local effective normal solar absorptance, α_{nel}, and the local effective hemispherical IR emittance, ϵ_{hel}, for an LV or an SLV of a rough surface. However, a rough surface consists of many LVs and/ or SLVs in reality. Thus the effective normal solar absorptance (α_{ne}) and the effective hemispherical IR emittance (ϵ_{he}) are needed to simulate radiation heat transfer for a rough surface. The macro-level model was therefore developed, using which α_{ne} and ϵ_{he} can be predicted based on the baseline values of α_n and ϵ_h. The macro-level model development included:

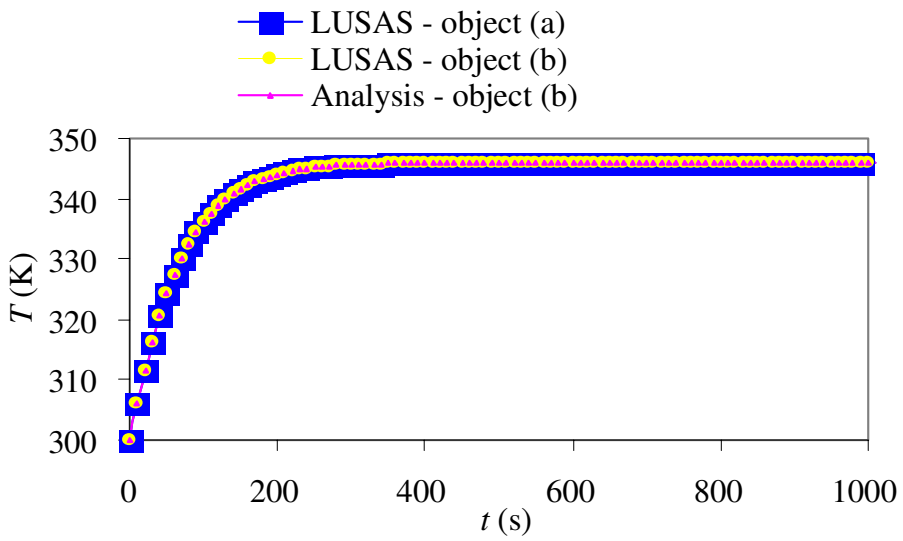

Figure 6.15: Comparison of temperature histories obtained using different methods for case CA-V3

(a) Surface profile idealization of scanned plasma sprayed alumina coating, including the comparison between the scanned coating surface profile and the surface profile of the coating under SEM, and refining of the scanned surface profile of alumina coating;

(b) Equation development for α_{ne};

(c) Equation development for ϵ_{he};

(d) Development and validation of C program "CP-Model", for performing all tedious calculations;

(e) Validation of the macro-level model, i.e., verification of α_{ne} and ϵ_{he} equations; and

(f) Application of the model for understanding radiation heat transfer for a rough plasma sprayed alumina coating surface.

Note that for the macro-level modeling, the ray reflected from an LV/ SLV will not be counted in for any other LV/ SLV.

6.4.1 Profile Idealization of Scanned Surfaces

It was observed that the plasma sprayed alumina coating surface profile obtained by Talyscan 150 does not exactly match with the real surface due to the experimental limitations, i.e., the resolutions in the X, Y and Z directions can only reach 0.5 μm, 1 μm and 0.1 μm respectively for Talyscan 150. Therefore the particles and valleys smaller than 0.5 μm, as shown in Figure 6.16, will be possibly lost for the surface profile obtained by Talyscan 150. In this figure, the small particles whose sizes are around 0.5 μm, marked as p1, p2 and p3, might not be captured by Talyscan 150. The shapes of particles p4 and p5 would not be shown in the surface profile obtained by Talyscan 150 as their sizes are about 0.4 μm and 0.25 μm. Similarly, the width of valleys v1, v3 and v6 is

around 0.5 μm, and therefore these valleys might not be captured by Talyscan 150. There are a certain number of very acute angles observed in the SEM surface profile. However, these angles can hardly be found in the surface profile scanned by Talyscan 150. For example, in Figure 6.16, the edges v2, v4 and v5 form their own LV shape or SLV shape with the corresponding angles smaller than 30°. A statistical result shows that, 96.15 % of the angle values are concentrated in the range from 70° to 90° for a typical length of surface, as shown in Figure 6.17 and Figure 6.18. In the two figures, it was found that for the length of 1000 μm, the angles between 80° to 90° have a percentage of 43.88%; the angles smaller than 50° only have a percentage of 0.30%. However, the angles smaller than 50° will have more percentage, rather than 0.30%, in Figure 6.16. Thus A certain percentage of particles/ particle edges/ valleys whose size is smaller than 0.5 μm will be lost in the surface profile obtained by Talyscan 150. The larger particles and valleys with nearly vertical sides cannot be faithfully recorded. However, these particles and

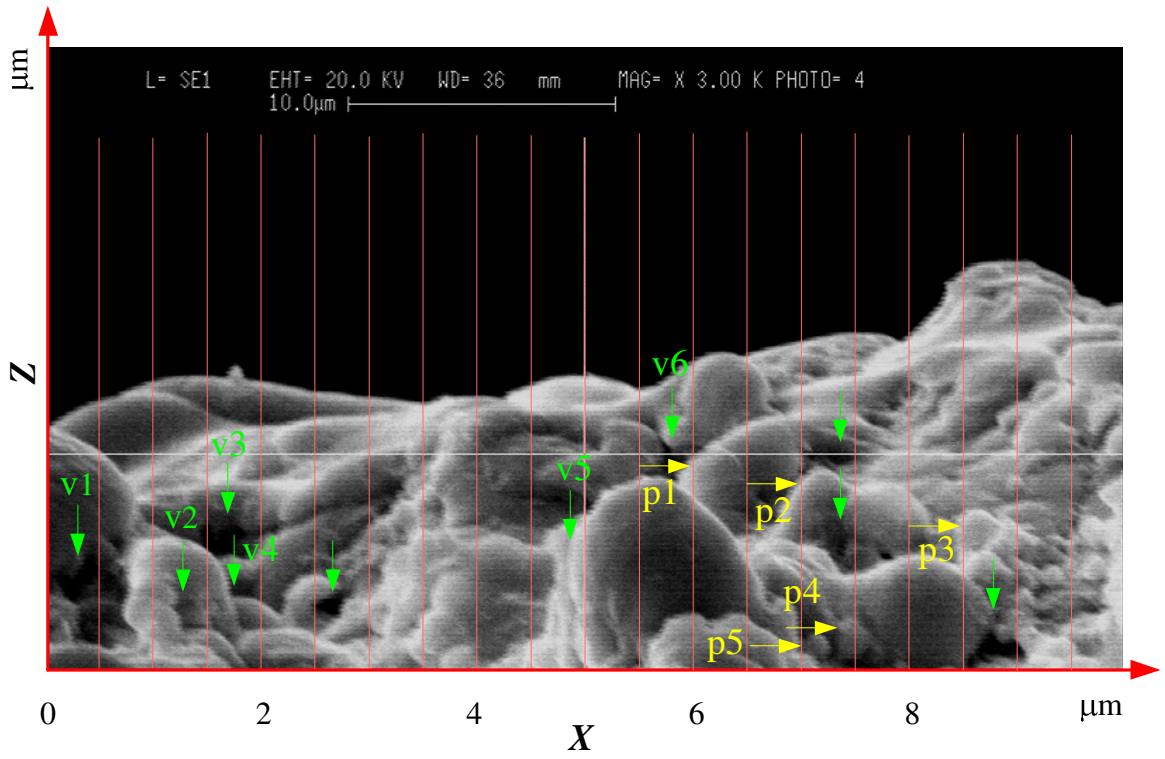

Figure 6.16: A typical plasma sprayed alumina coating surface obtained by scanning electron microscope showing small particles/ valleys that will be possibly lost from the surface profile obtained by Talyscan 150

valleys can be observed by SEM. However SEM cannot provide the surface profile for a surface in terms of coordinates. In order to get a more accurate surface profile, the two scanning methods must be combined judiciously so that the obtained profile matches the real surface profile as closely as possible. Such combination can be carried out by particle interpolation and valley interpolation based on the statistical data for the SEM pictures, which are taken randomly along the X direction for the sample after it is scanned by Talyscan 150. A total of 17 such SEM pictures were selected to calculate the average particle and valley sizes according to their distribution at an interval of 0.5 μm. The size of the particle/ valley was measured manually. This process is explained in sections 7.1.1

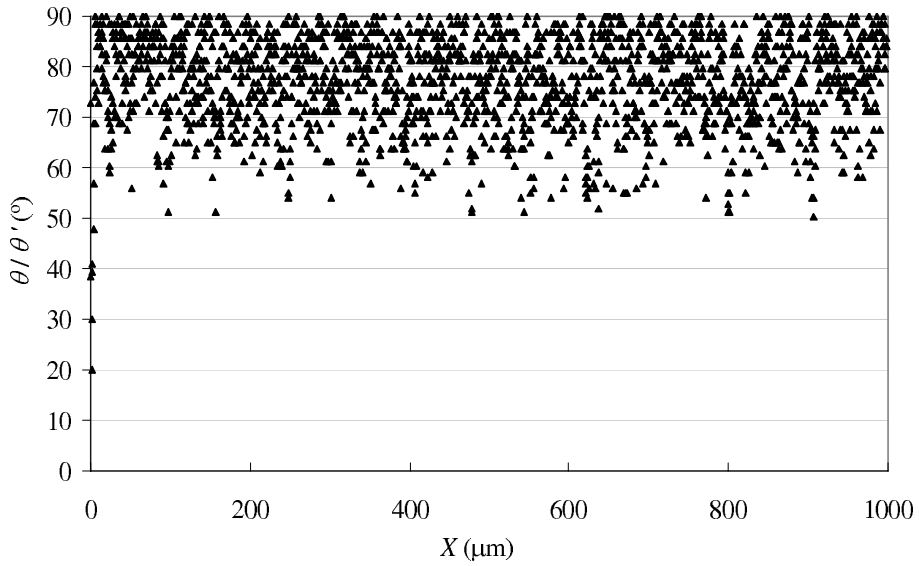

Figure 6.17: Angle value (θ and $\theta^{'}$) distributions along X axis of a scanned surface profile using Talyscan 150

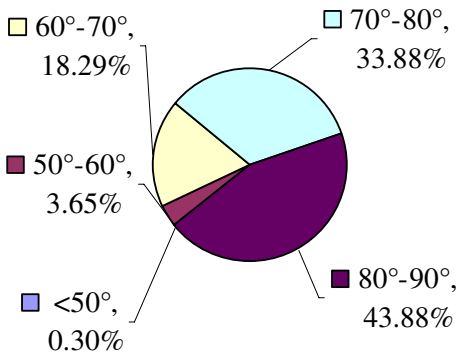

Figure 6.18: Percentage of angle value (θ and $\theta^{'}$) distributions for the data presented in Figure 6.17

and 7.1.2.

6.4.1.1 Particle Interpolation

For particle interpolation, two parameters are necessary, i.e., a particle size(D) and its number (N). Thus, for a scanned surface, different sizes of particles and their numbers are needed. These parameters can only be obtained precisely from the SEM surface profile. However, it is impossible to measure all the particles for a whole surface by SEM profile because there are hundreds of thousands of particles. Therefore, sampling of the scanned surface is needed. When the different sizes of particles and their numbers for a typical sample surface are obtained, the different sizes of particles and their numbers for any other scanned surface from the same lot can be deduced. For example, for a sample surface whose area is wL_s and there are N_s number of particles whose size is approximately 0.5 μm, a large surface with a total area of wL_t, the number of 0.5-μm size particle (N_t)will be

$$N_t = \frac{N_s}{wL_s} \times wL_t = \frac{N_s L_t}{L_s} \tag{6.55}$$

where w is the width and L is the length of the area.

The particles were measured along a typical scanning line (i.e., Y=constant) on the SEM surface profile. For easy interpolation, the average size of the particles is obtained for every 0.5 μm range, i.e., the particle size in the range of 0-0.5 μm will be averaged; the particle size in the range of 0.5-1.0 μm will be averaged; the particle size in the range of 1.0-1.5 μm will be averaged; the rest may be deduced similarly. There is correspondence between each averaged particle size and the resolution used for the interpolation, i.e., for average particle size in the range of 0.5-1.0 μm, the resolution of 1.0 μm will be used for the interpolation; for average particle size in the range of 1.0-1.5 μm, the resolution of 1.5 μm will be used for the interpolation; the rest may be deduced. The particle sizes and their numbers for a sample surface profile are shown in Table 6.4.

Generally, plasma spray process fuses alumina particles. As a result, most of the particles maintain the hemispherical boundary. Thus, assuming them as solids with octagonal surface boundary is not unrealistic. Moreover, at a micron level, a curved boundary can be closely represented by a series of straight lines. Hexagon or even tetragon would not be proper to represent a circular-shape particle. On the other hand, enneagon or even decagon are not necessary. Therefore, particle interpolation is used just to interpolate a half of the particle in the scanned surface. That is, for two neighboring scanned points, four points will be interpolated to form a half octagon, as shown in Figure 6.19. In this figure, the points P_1 and P_2 are the points obtained using Talyscan 150 measurements (P_1P_2 is the default surface formed by joining points P_1 and P_2) and D is the particle size. The points P_3, P_4, P_5 and P_6 are the points interpolated between points P_1 and P_2. Thus $P_1P_3P_4P_5P_6P_2$ is the surface formed by particle interpolation based on points P_1 and P_2.

6.4.1.2 Valley Interpolation

Valley interpolation was carried out with the similar manner as that for particle interpolation. The valley was characterized by its width and angle. The total number of valley interpolations was calculated in the same manner as defined in Equation 6.55. The respective sizes of valleys are sorted according to their width. After this, the valleys whose

Table 6.4: Particle size distribution

Average particle dia. (μm)	N_s	L_s (μm)	L_t	N_t	Resolution to be used for the surface scan(μm)
0.80	6	547.15	48000.00	526	1.0
1.27	19	547.15	48000.00	1667	1.5
1.76	26	547.15	48000.00	2281	2.0
2.29	16	547.15	48000.00	1404	2.5
2.82	6	547.15	48000.00	526	3.0
3.19	4	547.15	48000.00	351	3.5
3.80	1	547.15	48000.00	88	4.0
4.14	1	547.15	48000.00	88	4.5
5.34	2	547.15	48000.00	175	5.5
6.08	1	547.15	48000.00	88	6.5

width is between 0-0.5 μm are grouped and their averaged width and angle are calculated. The averaged width will be in the range of 0-0.5 μm and the corresponding interpolation will apply to the profile with a resolution of 0.5 μm. For an interval of 0.5 μm, which is the Talyscan 150's scanning resolution in the X direction, the valley width and angle are averaged and the corresponding resolution for interpolation will be used. The valley size distribution for the surface under consideration is presented in Table 6.5. The valley interpolation strategy is shown in Figure 6.20. In this figure, P_1 and P_2 are scanned points (P_1P_2 is the surface formed by scanning). P_3 and P_4 are interpolated based on points P_1 and P_2 (surface $P_1P_3P_4P_2$ is the new surface generated by interpolation).

The interpolated particles/ valleys were randomly distributed over the scanned

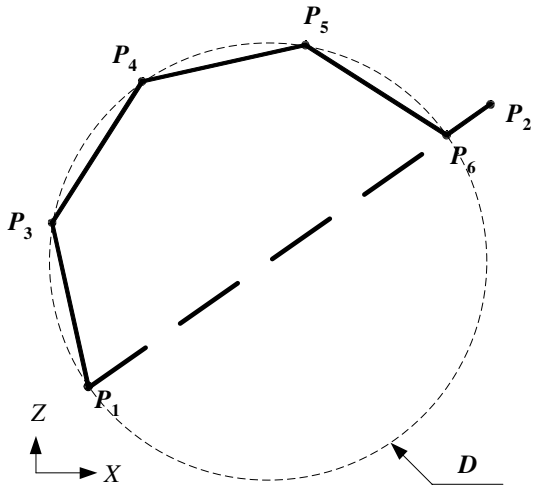

Figure 6.19: Particle interpolation strategy

Table 6.5: Valley size distribution

Avg. width (μm)	Avg. angle (°)	N_s	L_s (μm)	L_t (μm)	Resolution to be used (μm)	N_t
0.76	57.50	2	547.15	48000.00	1.0	175
1.36	64.80	10	547.15	48000.00	1.5	877
1.64	58.00	5	547.15	48000.00	2.0	439
2.32	82.50	2	547.15	48000.00	2.5	175
3.31	70.00	7	547.15	48000.00	3.5	614
3.64	88.50	2	547.15	48000.00	4.0	175
4.65	24.00	1	547.15	48000.00	5.0	88
5.74	65.00	1	547.15	48000.00	6.0	88
6.17	120.00	1	547.15	48000.00	6.5	88

length according to their percentage stated in Tables 6.4 and 6.5. After interpolation, α_{ne} and ϵ_{he} will be calculated for every resolution of profile and finally they will be summed up so that the final α_{ne} and ϵ_{he} can be obtained for a large surface.

6.4.2 Effective Absorptance (α_{ne}) Equation Development

Based on Equation 6.1, the α_{ne} for a surface (as shown in Figure 6.21) will be:

$$\alpha_{ne} = \frac{\alpha_{nel1}\left(A_{01}+A'_{01}\right)I_0 + \alpha_{nel2}\left(A_{02}+A'_{02}\right)I_0 + \alpha_{nel3}\left(A_{03}+A'_{03}\right)I_0}{\left(A_{01}+A'_{01}\right)I_0 + \left(A_{02}+A'_{02}\right)I_0 + \left(A_{03}+A'_{03}\right)I_0} \tag{6.56}$$

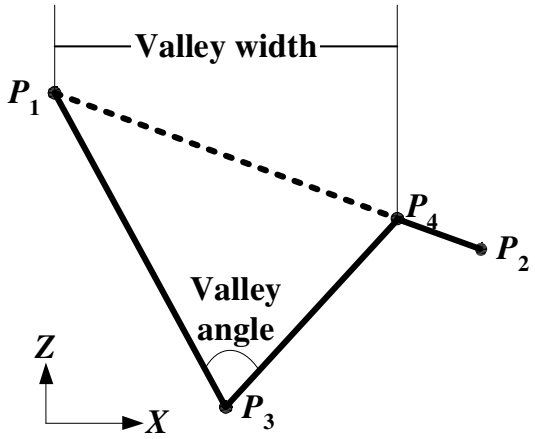

Figure 6.20: Valley interpolation strategy

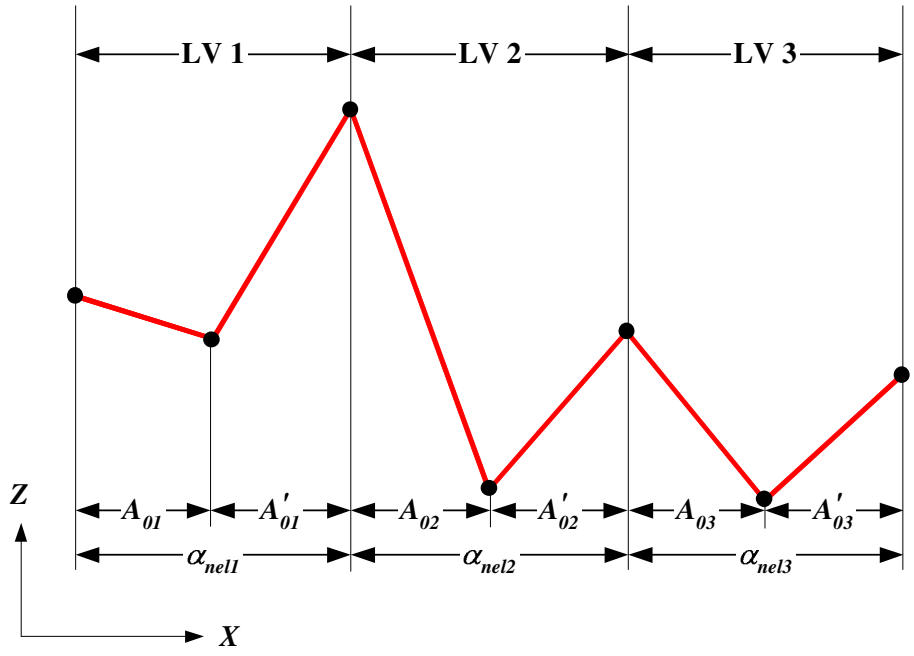

Figure 6.21: An example for calculating effective absorptance(α_{ne})

Thus, for a surface consisting u LVs, the α_{ne} will be

$$\alpha_{ne} = \frac{\sum_{m=1}^{u} \alpha_{nelm} \left(A_{0m} + A'_{0m}\right) I_0}{\sum_{m=1}^{u} \left(A_{0m} + A'_{0m}\right) I_0} = \frac{\sum_{m=1}^{u} \alpha_{nelm} \left(A_{0m} + A'_{0m}\right)}{\sum_{m=1}^{u} \left(A_{0m} + A'_{0m}\right)} \tag{6.57}$$

Thus, for an SLV consisting of v SLVs, the α_{ne} will be

$$\alpha_{ne} = \frac{\sum_{m=1}^{v} \alpha_{nel_m} A_m}{\sum_{m=1}^{v} A_m} \tag{6.58}$$

Based on the Equations 6.57 and 6.58, for a surface consisting of u LVs and v SLVs, α_{ne} will be

$$\alpha_{ne} = \frac{\sum_{m=1}^{u} \alpha_{nel_m} \left(A_{0m} + A'_{0m}\right) + \sum_{q=1}^{v} \alpha_{nel_q} A_q}{\sum_{m=1}^{u} \left(A_{0m} + A'_{0m}\right) + \sum_{q=1}^{v} A_q} \tag{6.59}$$

6.4.3 Effective Emittance (ϵ_{he}) Equation Development

Based on Equation 6.44, ϵ_{he} for the surface shown in Figure 6.22 will be

$$\epsilon_{he} = \frac{\epsilon_{hel1} \left(A_{01} + A'_{01}\right) + \epsilon_{hel2} \left(A_{02} + A'_{02}\right) + \epsilon_{hel3} \left(A_{03} + A'_{03}\right)}{\left(A_{01} + A'_{01}\right) + \left(A_{02} + A'_{02}\right) + \left(A_{03} + A'_{03}\right)} \tag{6.60}$$

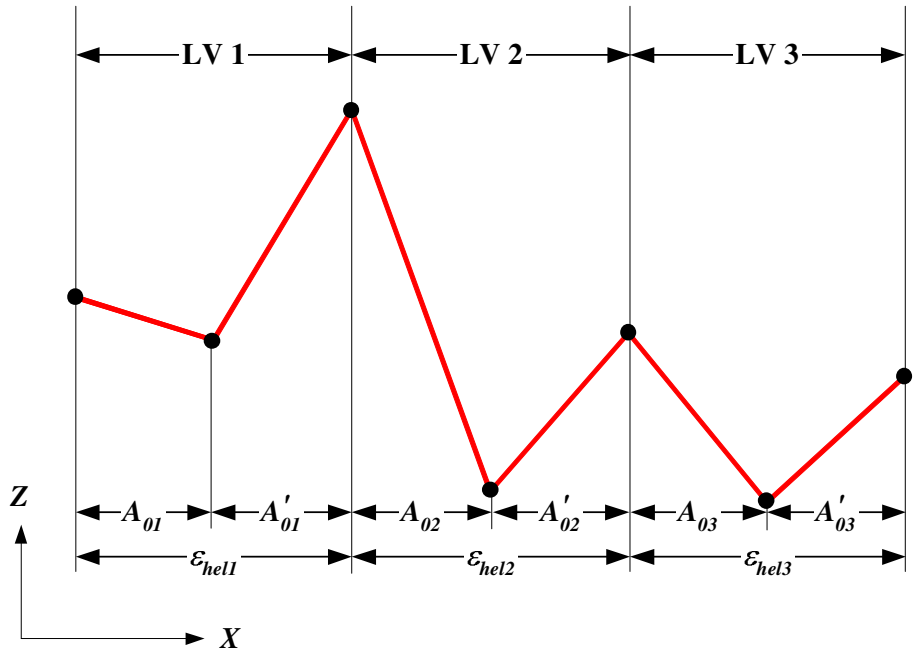

Figure 6.22: An example for calculating effective emittance(ϵ_{he})

Therefore, for a surface consisting of u LVs, ϵ_{he} will be

$$\epsilon_{he} = \frac{\sum_{m=1}^{u} \epsilon_{hel_m} \left(A_m + A_m^{'}\right)}{\sum_{m=1}^{u} \left(A_m + A_m^{'}\right)} \tag{6.61}$$

For a surface consisting of v SLVs, ϵ_{he} will be,

$$\epsilon_{he} = \frac{\sum_{m=1}^{v} \epsilon_{hel_m} A_m}{\sum_{m=1}^{v} A_m} \tag{6.62}$$

Based on Equations 6.61 and 6.62, for a surface consisting of u LVs, and v SLVs, ϵ_{he} will be

$$\epsilon_{he} = \frac{\sum_{m=1}^{u} \epsilon_{hel_m} \left(A_{0m} + A_{0m}^{'}\right) + \sum_{q=1}^{v} \epsilon_{hel_q} A_q}{\sum_{m=1}^{u} \left(A_{0m} + A_{0m}^{'}\right) + \sum_{q=1}^{v} A_q} \tag{6.63}$$

6.4.4 Implementation and Validation of Effective Absorptance (α_{ne}) and Effective Emittance (ϵ_{he})

6.4.4.1 Implementation

The model was implemented through surface profile scanning (using Talyscan 150 and SEM), parameters calculation and particles and/ or valleys interpolation (using user-written C program, "CP-Model"). The detailed procedure is:

Step 1: Scan plasma sprayed alumina coating surface using Talyscan 150 to obtain the surface profile (X, Z). The X-resolution is 0.5 μm and the Y-resolution is 1.0 μm.

Step 2: Scan the alumina coating surface using SEM to obtain the numbers, sizes and distributions of particles and valleys. Count the number of particles and valleys for the SEM surface at certain locations.

Step 3: Distribute randomly the particles and valleys obtained in Step 2 according to their respective proportions. Thus the alumina coating surface profile will be updated to $(X^{'}, Z^{'})$.

Step 4: "CP-Model" program reads (X', Z') coordinates of the updated profile and calculates $l_j, \theta_j, A_j, I_j, l'_k, \theta'_k, A'_k$ and I'_k $(j = 0, 1, 2, \cdots, i_{max} - 1;\ k = 0, 1, 2, \cdots, i'_{max} - 1\ )$

Step 5: "CP-Model" program identifies the LVs and SLVs, calculates view factors, F, for every LV.

Step 6: "CP-Model" program calculates α_{nel} and ϵ_{hel} for each LV and SLV.

Step 7: Finally, "CP-Model" program calculates α_{ne} and ϵ_{he} for the scanned alumina coating surface.

6.4.4.2 Validation

For validating the α_{ne} and ϵ_{he} equations, a typical surface consisting of 3 LVs and 1 SLV was created, as shown in Figure 6.23 (a). The α_{ne} and ϵ_{he} values, which were derived from α_n and ϵ_h of surface (a), will be used as the absorptance and IR emittance for the flat surface (b), as shown in Figure 6.23 (b). In this figure, the α_{nel} and ϵ_{hel} are local absorptance and IR emittance for an LV/ SLV. The surfaces (a) and (b) have the same projected length d. If the temperature gradients and the final temperatures of surface (a) and (b) match for a given flux loading, the α_{nel} and ϵ_{hel} model, α_{ne} and ϵ_{he} model and "CP-Model" program will be validated at one time.

Before the simulations were performed using LUSAS, the basic numerical functions of the "CP-Model" program were verified by some other tools. Firstly, the length and angle for each LV/ SLV of the surface (a) were verified. For this verification, the input used is the (X, Z) of the scanned points. The results provided by the "CP-Model" are shown in Table 6.6. The results delivered by AutoCAD 2004 are shown in Table 6.7. The procedure using AutoCAD 2004 is: (1) draw the surface (a) shown in Figure 6.23 using the $(X,\ Y)$ coordinates of the points P_1 to P_8; (2) measure the length of every

line segment and the angle between every neighboring line segment using the "Aligned Dimension" and the "Angular Dimension" functions of the AutoCAD 2004; (3) save the results in a file.

It was found that the program "CP-Model" provided the correct length and angle calculations after comparing Table 6.6 and Table 6.7.

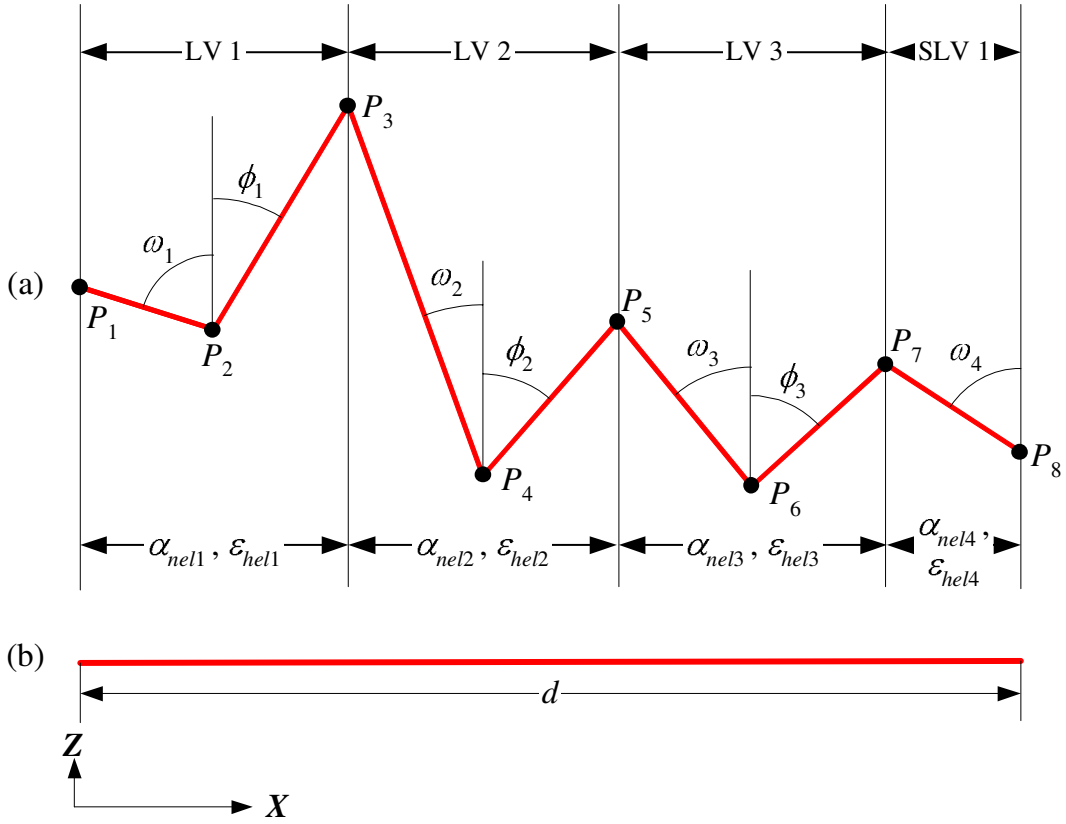

Figure 6.23: A typical pair of equivalent surfaces used for validating effective absorptance (α_{ne}) and effective emittance (ϵ_{he})

Table 6.6: Length and angle of local valley and semi local valley computed by "CP-Model" for Surface(a) shown in Figure 6.23

Input		Output	
$X(\mu m)$	$Z(\mu m)$	Length (μm)	Angle (°)
0.0	-13.921216	-	-
0.5	-14.077342	P_1P_2 = 0.523808	ω_1 = 72.659
1.0	-13.244671	P_2P_3 = 0.971257	ϕ_1 = 30.984
1.5	-14.623782	P_3P_4 = 1.466952	ω_2 = 19.928
2.0	-14.051321	P_4P_5 = 0.760073	ϕ_2 = 41.135
2.5	-14.662814	P_5P_6 =0.789888	ω_3 = 39.272
3.0	-14.207447	P_6P_7 = 0.676283	ϕ_3 = 47.675
3.5	-14.532709	P_7P_8 =0.596486	ω_4 = 56.955

The view factor (F) of an LV to its surrounding was calculated by Mathematica and validated by MATLAB, as presented in Table 6.8 and Table 6.9. The input used were the length and angle of each LV. Equation 6.46 was applied. The procedure of using Mathematica to calculate F is: (1) Establish the general equation defined in Equation 6.46; (2) input lengths and angles of every LV; (3) save F for every LV in a file. The procedure of using MATLAB to calculate F is similar. Comparing Table 6.8 and Table 6.9, it was found that Mathematica provided the correct calculations. The "CP-Model"

Table 6.7: Length and angle of local valley and semi local valley computed by AutoCAD for Surface(a) shown in Figure 6.23

Input		Output	
X (μm)	Z (μm)	Length (μm)	Angle (°)
0.0	-13.921216	-	-
0.5	-14.077342	$P_1P_2 = 0.523808$	$\omega_1 = 72.659$
1.0	-13.244671	$P_2P_3 = 0.971257$	$\phi_1 = 30.984$
1.5	-14.623782	$P_3P_4 = 1.466952$	$\omega_2 = 19.928$
2.0	-14.051321	$P_4P_5 = 0.760073$	$\phi_2 = 41.135$
2.5	-14.662814	P_5P_6 =0.789888	$\omega_3 = 39.272$
3.0	-14.207447	$P_6P_7 = 0.676283$	$\phi_3 = 47.675$
3.5	-14.532709	P_7P_8 =0.596486	$\omega_4 = 56.955$

Table 6.8: View factor computed by Mathematica for local valleys shown in Figure 6.23 (a)

Input		Output
Length (μm)	Angle (°)	View factor ($F_{Left-Right}$)
$P_1P_2 = 0.523808$	$\omega_1 = 72.659$	0.110408
$P_2P_3 = 0.971257$	$\phi_1 = 30.984$	
$P_3P_4 = 1.466952$	$\omega_2 = 19.928$	0.457619
$P_4P_5 = 0.760073$	$\phi_2 = 41.135$	
$P_5P_6 = 0.789888$	$\omega_3 = 39.272$	0.254011
$P_6P_7 = 0.676283$	$\phi_3 = 47.675$	

Table 6.9: View factor computed by MATLAB for local valleys shown in Figure 6.23 (a)

Input		Output
Length (μm)	Angle (°)	View factor ($F_{Left-Right}$)
$P_1P_2 = 0.523808$	$\omega_1 = 72.659$	0.110408
$P_2P_3 = 0.971257$	$\phi_1 = 30.984$	
$P_3P_4 = 1.466952$	$\omega_2 = 19.928$	0.457619
$P_4P_5 = 0.760073$	$\phi_2 = 41.135$	
$P_5P_6 = 0.789888$	$\omega_3 = 39.272$	0.254011
$P_6P_7 = 0.676283$	$\phi_3 = 47.675$	

function for calculating α_{ne} and ϵ_{he} was validated by manual calculations for the surface (a). For these manual calculations, the middle variables were firstly calculated for each LV/ SLV, as shown in Table 6.10. In this table, it is assumed that $\alpha_n = 0.25$ and $\epsilon_h = 0.80$. θ_j ($j = 0, 1, 2, \cdots, i_{\max} - 1$) was calculated using Equation 6.12. $\theta_k^{'}$ ($k = 0, 1, 2, \cdots, i_{\max}^{'} - 1$) was calculated using Equation 6.13. l_j and $l_k^{'}$ were calculated using Equations 6.28 and 6.29, respectively. A_j was calculated using Equation 6.38. $A_k^{'}$ was calculated using Equation 6.39. I_j and $I_k^{'}$ were calculated using Equations 6.14 and 6.15 respectively. With the data in Table 6.10, α_{nel} and ϵ_{hel} for each LV/ SLV can be calculated using Equations 6.42, 6.45, 6.43 and 6.47 respectively, as shown in Table 6.11. Using the α_{nel} and ϵ_{hel} for each LV/ SLV, the α_{ne} and ϵ_{he} for the surface (a)

Table 6.10: Values of middle variables for surface (a) shown in Figure 6.23

-	θ_0	θ_1	θ_2	θ_3	$\theta_0^{'}$	$\theta_1^{'}$	$\theta_2^{'}$	$\theta_3^{'}$
LV_1	72.659	17.341	86.302	-	30.984	59.016	44.627	-
LV_2	19.928	70.072	9.009	52.054	41.135	48.865	12.198	73.261
LV_3	39.272	50.728	36.219	-	47.675	42.325	44.622	-
SLV_1	56.995	-	-	-	-	-	-	-
-	l_0	l_1	l_2	l_3	$l_0^{'}$	$l_1^{'}$	$l_2^{'}$	$l_3^{'}$
LV_1	0.5238	0.5238	7.7522	-	0.9713	0.9713	0.7026	-
LV_2	1.4670	1.4670	0.5062	0.8131	0.7601	0.76017	0.5116	1.73601
LV_3	0.7899	0.7899	0.6198	-	0.6763	0.6763	0.7025	-
SLV_1	0.5965	-	-	-	-	-	-	-
-	-	A_1	A_2	A_3	-	$A_1^{'}$	$A_2^{'}$	$A_3^{'}$
LV_1	-	0.5000	0.0626	-	-	0.5000	0.3728	-
LV_2	-	0.5000	0.5000	0.5000	-	0.5000	0.5000	0.2189
LV_3	-	0.5000	0.5000	-	-	0.5000	0.5000	-
SLV_1	-	0.5000	-	-	-	-	-	-
-	I_0	I_1	I_2	I_3	$I_0^{'}$	$I_1^{'}$	$I_2^{'}$	$I_3^{'}$
LV_1	1350.0	1350.0	1012.5	-	1350.0	1350.0	1012.5	-
LV_2	1350.0	1350.0	1012.5	759.4	1350.0	1350.0	1012.5	759.4
LV_3	1350.0	1350.0	1012.5	-	1350.0	1350.0	1012.5	-
SLV_1	1350.0	-	-	-	-	-	-	-

Table 6.11: Local effective absorptance (α_{nel}) and local effective emittance (ϵ_{hel}) for the each local valley and semi local valley of surface (a) in Figure 6.23

	LV_1	LV_2	LV_3	SLV_1
α_{nel}	0.3316	0.5386	0.4375	0.2500
ϵ_{hel}	0.6897	0.4422	0.5324	0.9539

can be calculated with Equations 6.59 and 6.63:

$$\alpha_{ne} = \frac{\sum_{m=1}^{3} \alpha_{nel_m} \left(A_{0m} + A'_{0m}\right) + \sum_{q=1}^{1} \alpha_{nel_q} A_q}{\sum_{m=1}^{3} \left(A_{0m} + A'_{0m}\right) + \sum_{q=1}^{1} A_q} \tag{6.64}$$

Thus,

$$\alpha_{ne} = \frac{0.3316 \times 1 + 0.5386 \times 1 + 0.4375 \times 1 + 0.25 \times 0.5}{1 + 1 + 1 + 0.5} = 0.4093 \tag{6.65}$$

$$\epsilon_{he} = \frac{\sum_{m=1}^{3} \epsilon_{hel_m} \left(A_{0m} + A'_{0m}\right) + \sum_{q=1}^{1} \epsilon_{hel_q} A_q}{\sum_{m=1}^{3} \left(A_{0m} + A'_{0m}\right) + \sum_{q=1}^{1} A_q} \tag{6.66}$$

Thus,

$$\epsilon_{he} = \frac{0.6897 \times 1 + 0.4442 \times 1 + 0.5324 \times 1 + 0.9539 \times 0.5}{1 + 1 + 1 + 0.5} = 0.6124 \tag{6.67}$$

The results provided by "CP-Model" were exactly the same: $\alpha_{ne} = 0.4093$, $\epsilon_{he} = 0.6124$. Thus, it proved that the C program "CP-Model" worked precisely.

The temperature simulations for the surfaces (a) and (b) were then performed using LUSAS. First, simulation was carried out for surface (a), using $\alpha_n = 0.2500$, $\epsilon_h = 0.8000$, $I_0 = 1400\ W/m^2$, the environment temperature 4 K, and the initial temperature 300 K. Its temperature history was then plotted, as shown in Figure 6.24, curve "Surface (a)". Secondly, the simulation was run for surface (b) with the same boundary conditions and loading except that absorptance and IR emittance were $\alpha_{ne} = 0.4093$ and $\epsilon_{he} = 0.6124$. The temperature history was then plotted, as shown in Figure 6.24, curve "Surface (b)". Comparing the two curves it was found that they match perfectly. Thus, both the macro-level model (α_{ne} and ϵ_{he} equations) and the developed computer program "CP-Model" were accurate and worked as expected.

6.4.4.3 Application of the Models to Surfaces with Plasma Sprayed Alumina Coating

The successfully developed model was then applied to samples S-PSA-03 (as sprayed surface) and S-PSA-04 (grounded surface) for determining their radiation properties,

using the procedures described previously. The corresponding results are shown in Table 6.12 and 6.13 respectively. Note that in Table 6.12, "PIN" means particle interpolation and "VIN" valley interpolation In Table 6.12, it was found that, for sample S-PSA-03 (as

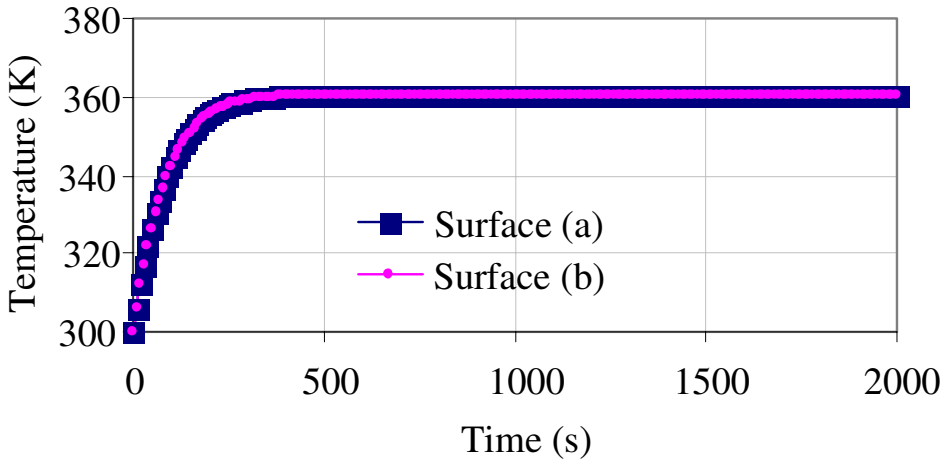

Figure 6.24: Temperature history comparison for surfaces (a) and (b)

Table 6.12: Effective absorptance (α_{ne}) results for S-PSA-03 (as sprayed surface)

Res. (μm)	Particle Dia. (μm)	Valley Angle (°)	Valley Width (μm)	$\frac{\alpha_{ne}-\alpha_n}{\alpha_n} \times 100\%$ (PIN:VIN)	$\frac{\epsilon_{he}-\epsilon_h}{\epsilon_h} \times 100\%$ (PIN:VIN)
0.50	-	-	-	- : -	- : -
1.00	0.80	57.50	0.76	0.12% : 4.89%	3.13% : 3.03%
1.50	1.27	64.80	1.36	0.53% : 0.56%	3.63% : 3.35%
2.00	1.76	58.00	1.64	0.93% : 4.03%	4.56% : 3.08%
2.50	2.29	82.50	2.32	0.70% : 5.23%	4.12% : 2.57%
3.00	2.82	-	-	0.29% : -	3.15% : -
3.50	3.19	70.00	3.31	0.23% : 1.49%	3.27% : 3.86%
4.00	3.80	88.50	3.64	0.06% : 0.87%	2.36% : 2.45%
4.50	4.14	-	-	0.07% : -	3.32% : -
5.00	-	24.00	4.65	- : 3.55%	- : 4.25%
5.50	5.34	-	-	0.15% : -	2.57% : -
6.00	-	65.00	5.74	- : 2.35%	- : 2.49%
6.50	6.08	120.00	6.17	0.12%: 0.02%	2.22% : 1.95%
7.00	-	-	-	-	-
7.50	-	-	-	-	-
8.00	-	-	-	-	-
8.50	-	-	-	-	-
9.00	-	-	-	-	-
9.50	-	-	-	-	-
10.00	-	-	-	-	-
Sum	-	-	-	3.20% : 22.99%	32.33% : 27.03%
	-	-	-	26.19%	59.36%

sprayed surface), $\alpha_{ne} = 1.2619\alpha_n$ and $\epsilon_{he} = 1.5936\epsilon_{he}$. In Table 6.13 it was found that, for sample S-PSA-04 (grounded surface), $\alpha_{ne} = 1.0498\alpha_n$ and $\epsilon_{he} = 1.3942\epsilon_{he}$. Comparing the α_{ne} and ϵ_{he} of S-PSA-03 and S-PSA-04 calculated by the model, it was found the surface conditions affect the effective radiation properties, i.e., the rougher the surface is, the higher the effective absorptance and emittance values are. This corresponds to the experimental results which show that the rougher surface of S-PSA-03 has higher absorptance and emittance than the surface of S-PSA-04 does.

The increase in absorptance for S-PSA-03 from the absorptance for S-PSA-04 is:

$$26.19\% - 4.98\% = 21.21\% \tag{6.68}$$

The increase in emittance for S-PSA-03 from the emittance for S-PSA-04 is:

$$59.36\% - 39.42\% = 19.94\% \tag{6.69}$$

Table 6.13: Effective absorptance (α_{ne}) results for S-PSA-04 (grounded surface)

Res. (μm)	Particle Dia. (μm)	Valley Angle (°)	Valley Width (μm)	$\frac{\alpha_{ne}-\alpha_n}{\alpha_n} \times 100\%$ (PIN:VIN [1])	$\frac{\epsilon_{he}-\epsilon_h}{\epsilon_h} \times 100\%$ (PIN:VIN)
0.50	-	-	-	- : -	- : -
1.00	0.75	60.0	0.75	0.04% : 0.13%	2.67% : 2.56%
1.50	1.50	95.0	1.22	0.02% : 0.15%	2.36% : 2.30%
2.00	1.70	-	-	0.13% : -	2.64% : -
2.50	2.30	-	-	0.18% : -	2.94% : -
3.00	2.85	100.0	2.61	0.15% : 0.28%	2.88% : 2.03%
3.50	3.05	77.5	3.19	0.18% : 0.95%	2.60% : 2.20%
4.00	3.80	-	-	0.15% : -	2.77% :
4.50	-	51.0	4.24	- : 1.15%	- : 2.97%
5.00	4.76	-	-	0.14% : -	2.54% : -
5.50	-	-	-	- : -	- : -
6.00	5.94	-	-	0.07% : -	2.11% : -
6.50	-	-	-	-	-
7.00	-	-	-	-	-
7.50	-	-	-	-	-
8.00	-	-	-	-	-
8.50	-	-	-	-	-
9.00	-	-	-	-	-
9.50	-	60.50	9.34	- : 1.26%	- : 3.85%
10.00	-	-	-	-	-
Sum	-	-	-	1.06% : 3.92%	23.51% : 15.91%
				4.98%	39.42%

The experimental results showed that, the increase in the absorptance and the emittance from the ground surface (S-PSA-04 and S-PSA-06) to as-sprayed surface (S-PSA-03 and S-PSA-05) is (refer to Table 4.4 for surface IDs):

Increase in absorptance:

$$\frac{\frac{0.318+0.301}{2} - \frac{0.250+0.243}{2}}{\frac{0.250+0.243}{2}} \times 100\% = 25.56\%$$

Increase in emittance:

$$\frac{\frac{0.801+0.810}{2} - \frac{0.795+0.795}{2}}{\frac{0.795+0.795}{2}} \times 100\% = 1.32\%$$

Comparing the increase in absorptance observed from the experimental measurements and the values predicted by the model, the percentage values are close. Assuming that the ground surface represented a flat surface, increase in absorptance for as-sprayed surface can be calculated. Similar percentage increase was also expected when the model was used. For the increase in ϵ_{he} the increases are quite substantial. However, the experimental values and the values predicted by the model could not be and need not be compared, because the model requires the base values. It is possible that in the case of emittance, the ground plasma sprayed surface does not provide similar values as that of an alumina block which could represent the base material.

6.5 Conclusions

Roughness plays a very important role in deciding the effective light energy absorptance α_{ne} and effective emittance ϵ_{he} of an opaque surface. However, the existing roughness parameters such as root-mean-square roughness cannot properly evaluate the surface roughness effects on radiation properties of opaque surfaces, i.e., α_{ne} and ϵ_{he}. Although some models have been developed to predict the effects, such as Davies' model, Tang and

Buckius's statistical geometric optics model [85], etc., they are valid only in very specific situations.

Therefore a micro-level energy absorption geometrical model was developed and applied to investigate the roughness effects with the help of 2D surface profile of a plasma-sprayed-alumina-coated substrate scanned at a micron level. This micro-level model predicts effective normal solar absorptance (α_{nel}) and effective hemispherical infrared emittance (ϵ_{hel}) of LV or SLV. A macro-level model was also developed based on the micro-level model to predict the effective normal solar absorptance (α_{ne}) and the effective hemispherical IR emittance (ϵ_{he}) of a rough surface consisting of LV and/ or SLV.

Both of the micro-level model and macro-level model were validated using numerical simulations and experimental results. The derived α_{ne} and ϵ_{he} values of the model, when used in the heat transfer analysis of an equivalent, smooth and optically flat surfaces, led to the prediction of the same rate of heat exchange and temperature as that of for the rough surface with its original radiation properties. As the model formulation is generic for the surfaces either of similar opaque materials or coated with such opaque materials where the substrates have little influence on the radiation properties, it can be used to incorporate the rough surface effects for other types of thermal coatings, provided the baseline values of α_n and ϵ_h are available for an optically flat surface of the same material.

Chapter 7

CONCLUSIONS AND RECOMMENDATIONS FOR FUTURE WORK

7.1 Conclusions

Micro-satellite technologies are the current trend in satellite development because they provide cost effective solutions to a wide range of missions. Thermal control becomes more important for smaller satellites, in view of the reduction in packaging space and thermal mass. As such, the passive thermal control methods are generally used for small satellites, because active methods require electric power, more hardware and space for installation. However, passive TCM deteriorate in the harmful outer space environment, leading to unanticipated mission problems. New and better TCMs are therefore constantly sought to reduce the difficulties in satellite thermal design and to ensure that the desired missions are completed.

In this thesis, the suitability of the plasma sprayed alumina coating as TCM was established through various information collected from the literature, the numerical simulations and the various experiments on representative samples. These different approaches show that, the relevant properties of plasma sprayed alumina coating are suitable as TCM, due to its better performance than that of the conventional coatings/ films. The reasons are:

(1) The alumina coating's outgassing is minimum because no organic element was used;

(2) The alumina coating's behavior is more predictable as its α/ϵ ratio is suitable as TCM and these values are less likely to degrade;

(3) The coating works as not only TCM, but also thermal barrier;

(4) The alumina coating can withstand severe thermal shock without delamination problem, which will cause failure of the coating function;

(5) The maximum thermal stress in the plasma-sprayed-alumina-coated aluminum panel is found to be very small and well within the safe range (about 90 to 100 MPa, less than the fracture stress of 138 MPa) as seen from the analysis.

(6) Furthermore, the thickness of both substrate and alumina coating can be minimized/ optimized by numerical simulations, which will help in designing better thermal control for a satellite.

The details showing plasma sprayed alumina coating's suitability as TCM are summarized in Table 7.1.

During the investigation, the surface roughness of plasma sprayed alumina coating is found important because the roughness affects the radiative heat exchange between the surface and its surrounding. Roughness parameters such as root-mean-square roughness cannot properly evaluate surface roughness effects on radiation properties of opaque surfaces. Some models have been developed to predict the effects, such as Davies' model, Tang and Buckius's statistical geometric optics model. However they are valid only in their own specific situations. An energy absorption geometry model was therefore developed to determine effective radiation properties for a rough plasma sprayed alumina coating surface. The model was validated using numerical simulations and experimental

results. The derived α_{ne} and ϵ_{he} values of the model, when used in the heat transfer analysis of an equivalent, smooth and optically flat surfaces, lead to the prediction of the same rate of heat exchange and temperature as that of for the rough surface. As the model formulations are generic for the surfaces either of similar opaque materials or coated with such opaque materials where the substrates have little influence on the radiation properties, they can be used to incorporate the rough surface effects for other types of thermal coatings, provided the baseline values of α_n and ϵ_h are available for an optically flat surface of the same material.

To conclude, the major contributions of this thesis are: 1) Suitability of plasma sprayed alumina coating as TCM was established by means of literature review, FE simulations and experiments, and 2) An energy absorption geometry model was developed and validated to determine the effective radiation properties for rough plasma sprayed alumina coating surface and such model can be extended to predict the effective surface

Table 7.1: Plasma sprayed alumina coating's suitability as thermal control material

Property	Testing method	Outcome
Color	Visual inspection	Whitish—good as reflectors and barriers
Density	Calculation by volume/ mass	3435 kg/m^3, thickness control required
Hardness	Microhardness tester	Better durability in orbit
Young's modulus	Literature and experiments	Proper stiffness of the plasma sprayed alumina coating
Vacuum outgassing	Literature (negligible); Vacuum baking	Reduced to minimum extent; No organic element
Thermal performance in orbit	Validated numerical scheme designed using LUSAS	Safe temperature range and the corresponding thermal stress and deflection
Contamination	Literature	No organic elements, no contamination
Degradation	Literature	Very stable under UV irradiation
Manufacturing	Experiments	Optimized plasma spraying parameters
α_n and ϵ_h	Experiments	Suitable as TCM
α_{ne} and ϵ_{he} model	Surface profile scanning and modeling	Effective surface properties useful for temperature prediction and expandable for other TCMs

radiation properties of other TCM coatings/ films.

7.2 Recommendations for Future Work

As mentioned in chapter 3, testing new materials in simulated space environment prior to an actual space flight testing opportunity is the first step toward acceptance and transition to new materials. The actual difficulties in integrating such plasma-sprayed-alumina-coated substrates into a satellite or spacecraft are to be studied. For example, if the plasma sprayed alumina coating is used for the solar panels, the adhesive bonding technique for the solar cells needs to be examined.

The C program for predicting the effective surface radiation properties, "CP-Model", will be more useful if a database is built to encompass particle/ valley sizes, numbers and their distributions as a function of spraying parameters. Such database can also be expanded for other TCMs. For ease of application, it is better to develop a user-friendly interface for the "CP-Model" program. A better surface scanning facility is also sought so that the interpolation will not be necessary for the macro-level model which could possibly result in better model results.

APPENDIX A: SHELDAHL TEST REPORT

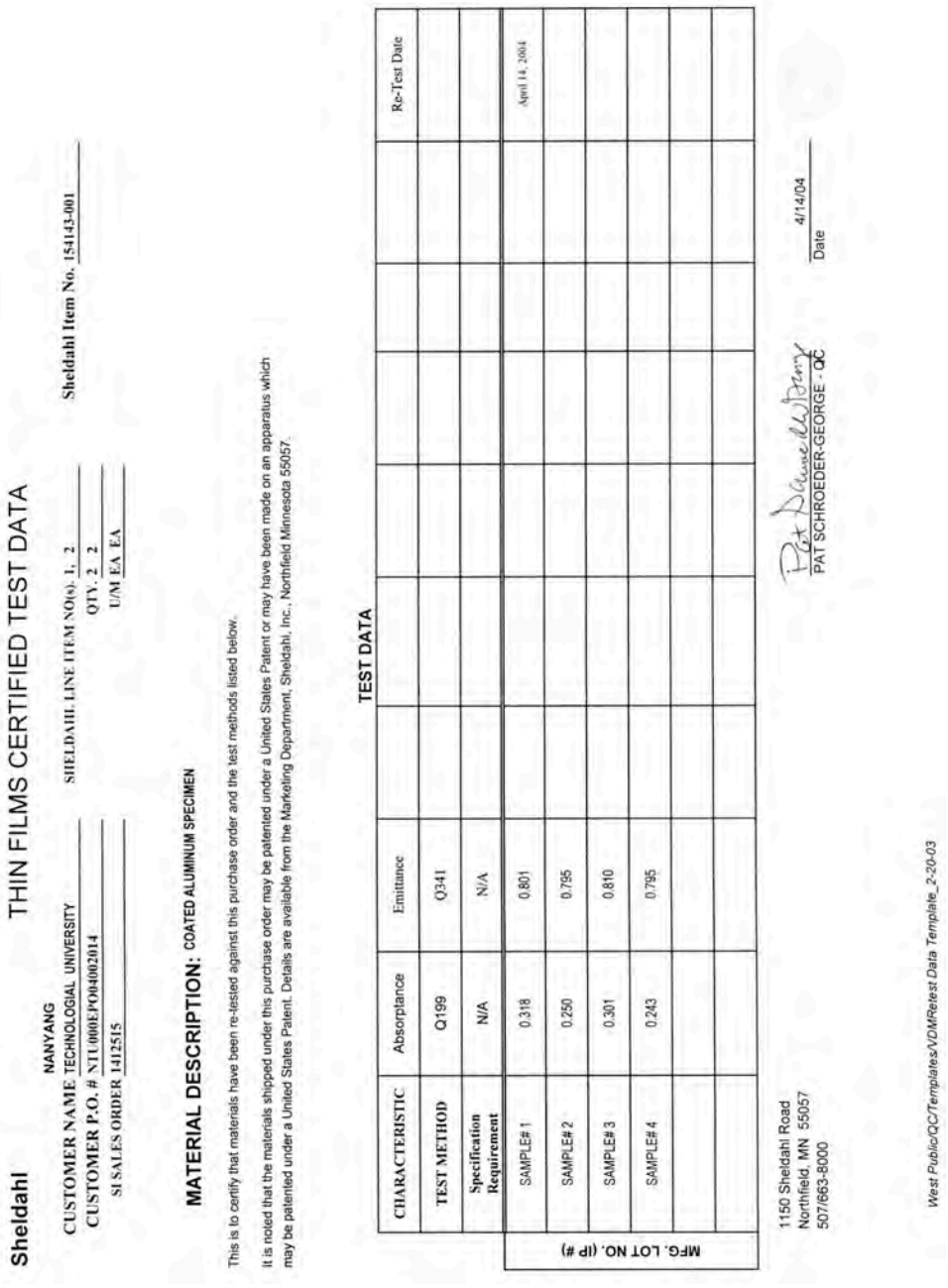

Sheldahl

THIN FILMS CERTIFIED TEST DATA

NANYANG
CUSTOMER NAME TECHNOLOGIAL UNIVERSITY
CUSTOMER P.O. # NTU000EP004002014
SI SALES ORDER 1412515

SHELDAHL LINE ITEM NO(s). 1, 2
QTY. 2 2
U/M EA EA

Sheldahl Item No. 154143-001

MATERIAL DESCRIPTION: COATED ALUMINUM SPECIMEN

This is to certify that materials have been re-tested against this purchase order and the test methods listed below.

It is noted that the materials shipped under this purchase order may be patented under a United States Patent or may have been made on an apparatus which may be patented under a United States Patent. Details are available from the Marketing Department, Sheldahl, Inc., Northfield Minnesota 55057.

TEST DATA

CHARACTERISTIC	Absorptance	Emittance							Re-Test Date
TEST METHOD	Q199	Q341							
Specification Requirement	N/A	N/A							
SAMPLE# 1	0.318	0.801							April 14, 2004
SAMPLE# 2	0.250	0.795							
SAMPLE# 3	0.301	0.810							
SAMPLE# 4	0.243	0.795							

MFG. LOT NO. (IP #)

Pat Schroeder-George

PAT SCHROEDER-GEORGE - QC

4/14/04
Date

1150 Sheldahl Road
Northfield, MN 55057
507/663-8000

West Public/QC/Templates/VDMRetest Data Template_2-20-03

References

[1] ASTM E 408: Standard test methods for total normal emittance of surfaces using inspection-meter techniques. 1971.

[2] NASA space vehicle design criteria (environment): Solar electromagnetic radiation(NASA SP-8005). pages 1–33, 1971.

[3] *New Technology Japan, Special Issue: Solar Power Satellite R&D in Japan*. Three "I" Publications Ltd, 1991.

[4] ASTM E595, total mass loss and collected volatile condensable materials from outgassing in a vacuum environment. 1993.

[5] NASA preferred reliability practices: Spacecraft thermal control coatings design and application (practice no. pd-ed-1239). pages 1–6, 1995.

[6] *Space Product Assurance: Thermal Cycling Test for the Screening of Space Materials and Processes*. ESA Publications Division, the Netherlands, 1999.

[7] ASTM E 490-00a: Solar constant and air mass zero solar spectral irradiance tables. 2000.

[8] ECSS-Q-70-02A, space product assurance: thermal vacuum outgassing test for the screening of space materials. 2000.

[9] *Space Engineering: Mechanical - Part 1: Thermal Control*. ESA Publications Division, the Netherlands, 2000.

[10] *Space Engineering: Space Environment.* ESA Publications Division, the Netherlands, 2000.

[11] BS EN 14091:2002 space product assurance–thermal vacuum outgassing test for the screening of space materials. pages 1–28, 2002.

[12] *Introduction To Small Satellites.* Small Satellites Homepage: http://centaur.sstl.co.uk/SSHP/, 2003.

[13] Sheldahl technical materials: Test methods. 2003.

[14] *Space Product Assurance: Measurements of Thermo-Optical Properties of Thermal Control Materials.* ESA Publications Division, the Netherlands, 2003.

[15] Webpage: http://www.tak2000.com/data/finish.htm♯spacecraft. 2003.

[16] A. A. Abdel-Samad, A. M. M. El-Bahloul, E. Lugscheider, and S. A. Rassoul. A comparative study on thermally sprayed alumina based ceramic coatings. *Journal of Materials Science*, 35:3127–3130, 2000.

[17] S. Ahmaniemi, M. Vippola, P. Vuoristo, T. Mantyla, M. Buchmann, and R. Gadow. Residual stresses in aluminum phosphate sealed plasma sprayed oxide coatings and their effect on abrasive wear. *Wear*, 252:614–623, 2002.

[18] M. Ahrens, R. Vaben, and D. Stover. Stress distributions in plasma-sprayed thermal barrier coatings as a function of interface roughness and oxide scale thickness. *Surface and Coatings Technology*, 161:26–35, 2002.

[19] D. W. Almgren and F. E. Ruccia. *Thermal Design of the Second Navigation Technology Satellite*, volume 70 of *Progress in Astronautics and Aeronautics.* AIAA, NASA Headquarters, Washington, D. C., 1979.

[20] A. Berghaus, A. Djahanbakhsh, and L. K. Thomas. Characterization of cvd-tungsten-alumina cermets for high-temperature selective absorbers. *Solar Energy Materials and Solar Cells*, 54:19–26, 1998.

[21] A. W. Brace and P. G. Sheasby. *the Technology of Anodizing Aluminum*. Technicopy Limited, Stonehouse, 2nd edition, 1979.

[22] M. Brogren, G. L. Harding, R. Karmhag, C. G. Ribbing, G. A. Niklasson, and L. Stenmark. Titanium-aluminum-nitride coatings for satellite temperature control. *Thin Solid Films*, 370:268–277, 2000.

[23] D. G. Cahill, S.-M. Lee, and T. I. Selinder. Thermal conductivity of k-alumina and alumina wear-resistant coatings. *Journal of Applied Physics*, 83(11):5783–5786, 1998.

[24] G. Carbajal, A. Martinez Villafane, J. G. Gonzalez Rodriguez, and V. M. Castano. Corrosion-resistant coatings: a nanotechnology approach. *Anti-Corrosion Methods and Materials*, 48(4):241–244, 2001.

[25] M. C. Chee. Performance analysis of thermal control materials and coatings for satellite. Technical report, School of Mechanical and Production Engineering, Nanyang Technological University, 2004.

[26] P. R. K. Chetty. *Satellite Technology and Its Applications*. TAB Professional and Reference Books, USA, 2nd edition, 1991.

[27] B. V. Cockeram and J. L. Hollenbeck. the spectral emittance and long-term thermal stability of coatings for thermophotovoltaic (TPV) radiator applications. *Surface and Coatings Technology*, 157:274–281, 2002.

[28] R. Creasey and G. P. Whitcomb. Small satellite projects in the european space agency (ESA). *Proceeding of the institution of mechanical engineers: Part G*, 213:201–212, 1999.

[29] CSM. *Micro-Hardness Tester Manual*. CSM, Switzerland, 2003.

[30] R. J. Damani. Mechanical and microstructural characterization of a free standing plasma sprayed alumina. In *Proceedings of the 15th International Thermal Spray Conference*, pages 1217–1222, May 1998.

[31] D. A. Denoirjean, O. Lagnoux, P. Fauchais, and V. Sember. Oxidation control in atmospheric plasma spraying: Comparison between $Ar/H_2/He$ and Ar/H_2 mixtures. In *Proceedings of the 15th international thermal spray conference*, page 809, Nice, France, 1998.

[32] A. Devasenapathi, C. B. Ang, S. C. M. Yu, and H. W. Ng. Role of particle injection velocity on coating microstructure of plasma sprayed alumina–validation of process chart. *Surface and Coatings Technology*, 139:44–54, 2001.

[33] M. Donabedian. Emittance of selected thermal control surfaces at cryogenic temperatures. December 1989.

[34] R. J. Duckett and C. S. Gilliland. Variable anodic thermal control coating on aluminum. June 1983.

[35] R. Emmerich, B. Enders, H. Martin, F. Stippich, G. K. Wolf, P. E. Andersen, J. Kudelha, P. Lukac, H. Hasuyama, and Y. Shima. Corrosion protection ability of alumina coatings deposited with ion beam assisted deposition. *Surface and Coatings Technology*, 89:47–51, 1997.

[36] L. C. Erickson, H. M. Hawthorne, and T. Troczynski. Correlations between microstructural parameters, micromechanical properties and wear resistance of plasma sprayed ceramic coatings. *Wear*, 250:569–575, 2001.

[37] J. R. Fincke, W. D. Swank, and D. C. Haggard. the influence of injector geometry and carrier gas flow rate on spray pattern. In C. C. Berndl, editor, *United Forum for Scientific and Technological Advances*, pages 335–342. ASM International, 1997.

[38] P. W. Fortescue and J. P. W. Stark. *Spacecraft Systems Engineering*. John Wiley & Sons, Chichester, 1995.

[39] Y. Gao, X. L. Xu, Z. J. Yan, and G. Xin. High hardness alumina coatings prepared by low power plasma spraying. *Surface and Coatings Technology*, 154:189–193, 2002.

[40] M. Gell, E. H. Jordan, Y. H. Sohn, D. Goberman, L. Shaw, and T. D. Xiao. Development and implementation of plasma sprayed nanostructured ceramic coatings. *Surface and Coatings Technology*, 146-147:48–54, 2001.

[41] D. G. Gilmore. *Satellite Thermal Control Handbook*. the aerospace corporation press, California, USA, 1994.

[42] D. Goberman, Y. H. Sohn, L. Shaw, E. Jordan, and M. Gell. Microstructure development of $Al_2O_3 - 13\ wt.\%\ TiO_2$ plasma sprayed coatings derived from nanocrystalline powders. *Acta Materialia*, 50:1141–1152, 2002.

[43] H. M. Hawthorne, L. C. Erickson, D. Ross, H. Tai, and T. Troczynski. The microstructural dependence of wear and indentation behavior of some plasma-sprayed alumina coatings. *Wear*, 203-204:709–714, 1997.

[44] I. Hofinger, K. Raab, J. Moller, and M. Bobeth. Effect of substrate surface roughness on the adherence of nicraiy thermal spray coatings. *Journal of Thermal Spray Technology*, 11(3):387–392, 2002.

[45] Choi H.S., Yoon B.H., Kim H.J., and Lee C.H. Isothermal oxidation of air plasma spray nicraly bond coatings. *Surface and Coatings Technology*, 150:297–308, 2002.

[46] C. H. Hsueh, P. F. Becher, E. R. Fuller, S. A. Langer, and W. C. Carter. Surface-roughness induced residual stresses in thermal barrier coatings: Computer simulations. *Materials Science Forum*, 308-311.

[47] A. K. Hyder, R. L. Wiley, G. Halpert, D. J. Flood, and S. Sabripour. *Spacecraft Power Technologies*. Imperial College Press, 2000.

[48] S. Igor and K. Mark. Anisotropic thermal conductivities of plasma-sprayed thermal barrier coatings in relation to the microstructure. *ASM International*, 9(4):478–482, 2000.

[49] N. Iwamoto and Y. Makino. The effect of pretreatments of metals on bond adhesion. pages 18–20, 1983.

[50] M. R. Jackson, P. A. Siemers, J. R. Rairden, R. L. Mehan, and A. M. Ritter. Composite structures produced by low pressure plasma deposition. In *Processing and Properties for Powder Metallurgy Composites (Proceedings of a symposium sponsored by the P/M Committees of TMS/AIME held at the Annual Meeting of the Metallurgical Society).*, pages 45–57, Denver, Colorado, 1987.

[51] S. Janisson, E. Meillot, A. Vardelle, J. F. Coudert, B. Pateyron, and P. Fauchais. Plasma spraying using ar-he-h2 gas mixtures. In *Proceedings of the 15th International Thermal Spray Conference*, pages 803–808, Nice, France, 1998.

[52] D. A. Jaworske. Optical and calorimetric evaluation of z-93-p and other thermal control coatings. *Thin Solid Films*, 290-291:278–282, 1996.

[53] D. A. Jaworske. Correlation of predicted and observed optical properties of multi-layer thermal control coating. *Thin Solid Films*, 332:30–33, 1998.

[54] R. L. Jones. *High Temperature Vanadate Corrosion of Yttria-Stailized Zirconia Coatings on Mild Steel*, pages 263–287. ASM International, 1988.

[55] E. H. Jordan, M. Gell, Y. H. Sohn, D. Goberman, L. Shaw, S. Jiang, M. Wang, T. D. Xiao, Y. Wang, and P. Strutt. Fabrication and evaluation of plasma sprayed nanostructured alumina-titania coatings with superior properties. *Materials Science and Engineering*, A301:80–89, 2001.

[56] R. R. Kamenetzky, J. A. Vaughn, M. M. Finckenor, and R. C. Linton. *Evaluation of Thermal Control Coatings and Polymeric Materials Exposed To Ground Simulated Atomic Oxygen and Vacuum Ultraviolet Radiation*, pages 1–42. NASA Technical Paper 3595. 1995.

[57] A. Kandiah and B. Shantonu. Outgassing in micro-satellite platforms. In *5th National Undergraduate Research Opportunities Program (NUROP)*, pages 1–4, Nanyang, Singapore, 1999.

[58] R. D. Karam. *Satellite Thermal Control for Systems Engineers*. AIAA, Reston, Virginia, USA, 1998.

[59] B. H. Kear, Z. Kalman, R. K. Sadangi, G. Skandan, J. Coiaizzi, and W. E. Mayo. Plasma-sprayed nanostructured alumina/ titania powders and coatings. *Journal of Thermal Spray Technology*, 9(4):483–487, 2000.

[60] C. E. Kennedy, R. V. Smilgys, D. A. Kirkpatrick, and J. S. Ross. Optical performance and durability of solar reflectors protected by an alumina coating. *Thin Solid Films*, 304:303–309, 1997.

[61] O. Kesler, M. Finot, S. Suresh, and S. Sampath. Determination of processing-induced stresses and properties of layered and graded coatings: Experimental method and results for plasma-sprayed ni-alumina. *Acta Materialia*, 45(8):3123–3134, 1997.

[62] O. Kesler, J. Matejicek, S. Sampath, and S. Suresh. Measurement of residual stress in plasma-sprayed composite coatings with graded and uniform compositions. *Material Science Forum*, 308-311:389–395, 1999.

[63] O. Kesler, J. Matejicek, S. Sampath, S. Suresh, T. Gnaeupel-Herold, P. C. Brand, and H. J. Prask. Measurement of residual stress in plasma-sprayed metallic, ceramic and composite coatings. *Materials Science and Engineering*, A257:215–224, 1998.

[64] A. Nusair Khan, J. Lu, and H. Liao. Effect of residual stresses on air plasma sprayed thermal barrier coatings. *Surface and Coatings Technology*, 168:291–299, 2003.

[65] H.-J. Kim, C. H. Lee, and Y. G. Kweonand. The effects of sealing on the mechanical properties of the plasma sprayed alumina-titania coating. *Surface and Coatings Technology*, 139:75–80, 2001.

[66] H.-J. Kim, S. Odoul, C.-H. Lee, and Y.-G. Kweon. the electrical insulation behavior and sealing effects of plasma-sprayed alumina-titania coatings. *Surface and Coatings Technology*, 140:293–301, 2001.

[67] H. S. Kim, H. H. Yang, I. H. Oh, and S. S. Kim. Bond strength of plasma sprayed chromium oxide coatings. *Material Science Forum*, 308-311:226, 1999.

[68] D. Kourtides, C. Carroll, M. Guzinski, J. Marschall, J. Pallix, J. Ridge, D. Smith, and D. Tran. Evaluation of thermal control coatings for flexible ceramic thermal protection system. Technical report, Ames Research Center, Moffett Field, California, July 1997.

[69] C. S. Kumar, A. K. Sharma, K. N. Mahendra, and S. M. Mayanna. Study on anodic oxide coating with low absorptance and high emittance on aluminum alloy 2024. *Solar Energy Materials & Solar Cells*, 60:51–57, 2000.

[70] T. Fukushima Kuroda, S. and S. Kitahara. Significance of the quenching stress in the cohesion and adhesion of thermally sprayed coatings. In *13th International Thermal Spraying Conference*, pages 903–909, Orlando, Florida, USA, 1992.

[71] W. J. Larson and J. R. Wertz. *Space Mission Analysis and Design*. Microcosm, Torrance, California, 2nd edition, 1992.

[72] L. Leblanc and C. Moreau. The long-term stability of plasma spraying. *Journal of Thermal Spray Technology*, 11(3):380–386, 2002.

[73] C.-J. Li and A. Ohmori. Relationships between the microstructure and properties of thermally sprayed deposits. *Journal of Thermal Spray Technology*, 11(3):365–374, 2002.

[74] Y. Li and K. A. Khor. Mechanical properties of the plasma-sprayed $Al_2O_3/ZrSiO_4$ coatings. *Surface and Coatings Technology*, 150:143–150, 2002.

[75] Y. Li and K. A. Khor. Microstructure and composition analysis in plasma sprayed coatings of $Al_2O_3/ZrSiO_4$ mixtures. *Surface and Coatings Technology*, 150:125–132, 2002.

[76] Omikron Delta Ltd. *SINDA/ G Manual*. Omikron Delta Ltd., Israel, 2001.

[77] D. Matejka and B. Benko. *Plasma Spraying of Metallic and Ceramic Materials*. John Wiley & Sons, Baffins Lane, Chichester, UK, 1989.

[78] J. R. Mawdsley. *Processing-Microstructure-Properties Relationships in Small-Particle Plasma-Sprayed Ceramic Coatings*. PhD thesis, Northwestern University, 2000.

[79] J. A. Mazer. *Solar Cells: An Introduction to Crystalline Photovoltaic Technology*. Kluwer Academic Publishers, Boston, 1997.

[80] R. McPherson. A review of microstructure and properties of plasma sprayed ceramic coatings. *Surface and Coatings Technology*, 39/40:173–181, 1989.

[81] M. Mellali, P. Fauchais, and A. Grimaud. Influence of substrate roughness and temperature on the adhesion/ cohesion of alumina coating. *Surface and Coatings Technology*, 81:275–286, 1996.

[82] M. J. Meshishnek. Long duration exposure facility experiment deintegration/ findings and impacts. *LDEF-69 months in space first post-retrieval symposium*, pages 1073–1107, 1992.

[83] D. Michel. Abcite, new generation coating-coatings for corrosion protection. *Pigment & Resin Technology*, 27:157–160, 1998.

[84] G. R. Min, Z. G. Zhang, and Z. Z. He. *Satellite Thermal Control Technology*. China Astronautics Publishing, Beijing, 1991.

[85] M. F. Modest. *Radiative Heat Transfer*. Academic Press, Elsevier Science, USA, 2nd edition, 2003.

[86] M. Moraw. Analysis of outgassing characteristics of metals. *Vacuum*, 38(7-9):523–525, 1986.

[87] A. R. Nicoll. the effect of varying plasma gun nozzle diameter on the surface roughness; hardness and bond strength of Al_2O_3 and Cr_2O_3 coatings. pages 19–25, October 1988.

[88] X. Nie, E. I. Meletis, J. C. Jiang, A. Leyland, A. L. Yerokhin, and A. Matthews. Abrasive wear/ corrosion properties and tem analysis of Al_2O_3 coatings fabricated using plasma electrolysis. *Surface and Coatings Technology*, 149:245–251, 2002.

[89] S. Oki, S. Gohda, and M. Yamakawa. Surface morphology of plasma sprayed ceramic coatings. In *The 15th International Thermal Spray Conference*, pages 593–597, Nice, France, 1998.

[90] A. Pajares, L. Wei, B. R. Lawn, N. P. Padure, and C. C. Berndt. Mechanical characterization of plasma sprayed ceramic coatings on metal substrates by contact testing. *Materials Science and Engineering*, A208:158–165, 1996.

[91] S. Parthasarathi, B. R. Tittmann, K. Sampath, and E. J. Onesto. Ultrasonic characterization of elastic anisotropy in plasma-sprayed alumina coatings. *Journal of Thermal Spray Technology*, 4(4):367–373, 1995.

[92] M. Pasandideh-Fard, V. Pershin, S. Chandra, and J. Mostaghimi. Splat shapes in a thermal spray coating process: Simulations and experiments. *Journal of Thermal Spray Technology*, 11(2):206–217, 2002.

[93] T. J. Patrick. Space environment and vacuum properties of spacecraft materials. *Vacuum*, 31(8-9):351–357, 1981.

[94] L. Pawlowski. Microstructural study of plasma-sprayed alumina and nickel chromium coatings. *Surface and Coating Technology*, 31:103–116, 1987.

[95] L. Pawlowski. *the Science and Engineering of Thermal Spray Coatings*. John Wiley & Sons, Chichester, 1995.

[96] A. Polat, O. Sarikaya, and E. Celik. Effects of porosity on thermal loadings of functionally graded $Y_2O_3 - ZrO_2/NiCoCrAlY$ coatings. *Materials and Design*, 23:641–644, 2002.

[97] K. Ramachandran, V. Selvarajan, P. V. Ananthapadmanabhan, and K. P. Sreekumar. Microstructure, adhesion, microhardness, abrasive wear resistance and electrical resistivity of the plasma sprayed alumina and alumina-titania coatings. *Thin Solid Films*, 315:144–152, 1998.

[98] F. K. Rault and A. Zahedi. Computational modeling of the reflectivity of $AlGaAs/GaAs$ and $SiGe/Si$ quantum well solar cells. *Solar Energy Materials & Solar Cells*, 2003.

[99] H. S. Rauschenbach. *Solar Cell Array Design Handbook*. Ban Nostrand Reinhold, New York, 1980.

[100] D. Reynolds, J. Kern, and J. L. Schoeneman. Nanosatellite program at sandia national laboratories. In *Space 2000: Proceedings of SPACE 2000; the seventh International Conference and Exposition on Engineering, Construction, Operations and Business in Space*, pages 461–468, Albuquerque, New Mexico, February-March 2000.

[101] S. Sampath, X. Jiang, A. Kulkarni, J. Matejicek, D. L. Gilmore, and R. A. Neiser. Development of process maps for plasma spray: Case study for molybdenum. *Materials Science and Engineering A*, 348:54–66, 2003.

[102] S. Sampath, W. C. Smith, T. J. Jewett, and H. Kim. Synthesis and characterization of grading profiles in plasma sprayed nicraly-zirconia fgms. *Materials Science Forum*, 308-311:383–388, 1999.

[103] K. W. Schlichting, N. P. Padture, E. H. Jordan, and M. Gell. Failure modes in plasma-sprayed thermal barrier coatings. *Materials Science and Engineering A*, 342:120–130, 2003.

[104] S. Seifert, J. I. Kleiman, and R. B. Heimann. Thermal optical properties of plasma-sprayed mullite coatings for space launch vehicles. *Journal of Spacecraft and Rockets*, 43(2):439–442, 2006.

[105] E. S. Seumahu. Investigation of the equatorial leo orbit for small satellite applications. *International Journal of Small Satellite Engineering*, August 1996.

[106] I. Sevostianov and M. Kachanov. Modeling of the anisotropic elastic properties of plasma-sprayed coatings in relation to their microstructure. *Acta Materialia*, 48:1361–1370, 2000.

[107] I. Sevostianov and M. Kachanov. Plasma-sprayed ceramic coatings: Anisotropic elastic and conductive properties in relation to the microstructure; cross-property correlations. *Material Science and Engineering A*, 297:235–243, 2001.

[108] L. L. Shaw, D. Goberman, R. Ren, M. Gell, S. Jiang, Y. Wang, T. D. Xiao, and P. R. Strutt. the dependency of microstructure and properties of nanostructured coatings on plasma spray conditions. *Surface and Coatings Technology*, 130:1–8, 2000.

[109] K.-B. Shin, C. G. Kim, C. S. Hong, and H. H. Lee. Thermal distortion analysis of orbiting solar array including degradation effects of composite materials. *Composites: Part B*, 32:271–285, 2001.

[110] R. Siegel and J. R. Howell. *Thermal Radiation Heat Transfer*. Taylor & Francis, New York, 4th edition, 2002.

[111] Y.S. Song, G. Lee, D.Y. Lee, D.-J. Kim, S. Kim, and K.Y. Lee. High-temperature properties of plasma-sprayed coatings of $YSZ/NiCrAlY$ on inconel substrate. *Materials Science and Engineering A*, 332:129–133, 2002.

[112] H.-D. Steffens and U. Fischer. *Correlation Between Microstructure and Physical Properties of Plasma Sprayed Zirconia Coatings*, pages 167–173. Thermal spray technology: new ideas and processes (Proceedings of national thermal spray conference). ASM International, Cincinnati, Ohio, USA, 1988.

[113] Y. J. Su, T. F. Bernecki, and K. T. Faber. In situ characterization of small-particle plasma sprayed powders. *Journal of Thermal Spray Technology*, 11(1):52–61, 2002.

[114] K. Takahashi, I. Tsuji, and N. Hirota. The application of advanced plasma coating to hot parts for heavy-duty gas turbine. In *Thermal Spray Research and Applications, Proceedings of the Third National Thermal Spray Conference*, pages 439–441, Long Beach, CA, USA, May 1990.

[115] Y. S. Touloukian. *Thermal Radiative Properties: Coatings*. IFI/ Plenum, New York, 1989.

[116] A. C. Tribble. *The Space Environment: Implications for Spacecraft Design*. Princeton University Press, 1995.

[117] R. C. Tucker. Structure property relationships in deposits produced by plasma spray and detonation gun techniques. *Journal of Vacuum Science and Technology*, 11:725–734, 1974.

[118] R. C. Tucker. *Plasma and Detonation Gun Deposition Techniques and Coating Properties*, pages 454–489. Depostion technologies for films and coatings. Noyes publications, 1982.

[119] M. Vardelle, P. Fauchais, A. Vardelle, and A. C. Leger. Numerical study of the relative importance of turbulence, particle size and density, and injection parameters on particle behavior during thermal plasma spraying. In C.C. Berndt, editor, *Thermal spray: A united forum for scientific and technological advances*, pages 535–542, Materials Park, Ohio, USA, 1997. ASM International.

[120] M. Vippola, J. Vuorinen, P. Vuoristo, T. Lepisto, and T. Maantyla. Thermal analysis of plasma sprayed oxide coatings sealed with aluminium phosphate. *Journal of the European Ceramic Society*, 22:1937–1946, 2002.

[121] Y. Wang, W. Chen, and L. Wang. Micro-indentation and erosion properties of thermal sprayed *nial* intermetallic-based alloy coatings. *Wear*, 254:350–355, 2003.

[122] S. Wernick and R. Pinner. *Surface Treatment and Finishing of Aluminum and its Alloys*, volume I&II. Robert Draper, New York, 1972.

[123] R. Westergard, N. Axen, U. Wiklund, and S. Hogmark. An evaluation of plasma sprayed ceramic coatings by erosion, abrasion and bend testing. *Wear*, 246:12–19, 2000.

[124] G. F. Weston. Materials for ultrahigh vacuum. *Vacuum*, 25(11/12):119–134, 1986.

[125] D. L. Wilkes and L. H. Hummer. Thermal control surfaces experiment-initial flight data analysis-final report. Technical report, 1991.

[126] D. R. Yan, J. N. He, J. J. Wu, W. Q. Qiu, and J. Ma. the corrosion behavior of a plasma spraying alumina ceramic coating in dilute HCL solution. *Surface and Coatings Technology*, 89:191–195, 1997.

[127] D. Yana. An investigation of the corrosion behavior of Al_2O_3-based ceramic composite coatings in dilute HCL solution. *Surface and Coatings Technology*, 141:1–6, 2001.

[128] S. J. Yankee and B. J. Pletka. Effect of plasma spray processing variations on particle melting and splat spreading of hydroxylapatitle and alumina. *Journal of Thermal Spray Technology*, 2(3):271–282, 1993.

[129] Y. Zeng, S. W. Lee, and C. X. Ding. Plasma spray coatings in different nanosize alumina. *Materials Letters*, 57:495–501, 2002.

[130] Q. C. Zhang. Recent progress in high-temperature solar selective coatings. *Solar Energy Materials & Solar Cells*, 62:63–74, 2000.